

Synthesis and Characterization of Magneto-Plasmonic Hybrid Nanoparticles for Biomedical Applications

Sara Félix Medeiros dos Santos

Thesis to obtain the Master of Science Degree in

Bioengineering and Nanosystems

Supervisors: Prof. Dr. Maria Clara Henriques Baptista Gonçalves
Prof. Dr. Marta Estrader Bofarull

Examination Committee

Chairperson: Prof. Dr. Jorge Manuel Ferreira Morgado
Supervisor: Prof. Dr. Maria Clara Henriques Baptista Gonçalves
Member of the Committee: Prof. Dr. Gabriel António Amaro Monteiro

October 2021

I declare that this document is an original work of my own authorship and that it fulfills all the requirements of the Code of Conduct and Good Practices of University of Lisbon.

*Para o avô Eugénio,
avó Gracinda
e avô Pedro*

Preface

The work presented in this thesis was performed at the University of Barcelona, into both the Chemistry Department and the Physics Department, during the period from March to October of 2021, under the supervision of professors Xavier Batlle Gelabert and Marta Estrader Bofarull, within the frame of the Erasmus⁺ Work Placements programs. This thesis was also co-supervised at Instituto Superior Técnico by professor Maria Clara Gonçalves.

Acknowledgments

First of all, I'd like to thank my supervisors at the University of Barcelona, professors Xavier Batlle Gelabert and Marta Estrader Bofarull for giving me the opportunity to work at the UB and to live in this wonderful city. I am deeply grateful to not only Xavier Batlle and Marta Estrader, but also to professor Amilcar Ramon Labarta Rodriguez, Víctor Fernández-Altable and Mariona Escoda I Torroella for all the guidance and valuable suggestions throughout all the work.

To my parents, for supporting me emotionally and financially on everything I do, to my grandma for her unconditional love and support and to my sisters and brother: to Filipa for being my first best friend, to Mariana for being a true inspiration, to Henrique for being the best brother I could ever have and to Sofia for being such a special soul.

Last but not the least, I'd like to thank my friends for keeping it fun. Particularly, to Constança for being my role-model and the most intelligent person I know, to Inês for being my unconditional supporter and to Catarina for all her advices and valuable skills.

Thank you all, without you this wouldn't be possible.

Abstract

Cancer is one of the biggest causes of death in the world thus it is becoming increasingly important to improve cancer treatments and its early diagnosis. In this sense, a lot of research has been made in nanotechnology over the last few decades towards the implementation of new strategies to fight this disease. In this work, it was intended to synthesize spherical hybrid magneto-plasmonic nanoparticles, incorporating gold (Au) on the core and both gold and iron (AuFe) on the shell, that could further be translated into nanorods with the same composition, which would take advantages of both optical and magnetic properties of Au and Fe, respectively, along with its NIR(Near Infrared)-responsive feature provided by the rod shape. Hence, the nanoparticles obtained would be capable of taking tasks such as improve magnetically-based imaging techniques by enhancing image contrast, improve magnetic hyperthermia treatments and optimize magnetically-guided drug delivery systems in a non-invasive way provided by its NIR-responsive nature thus providing targeted treatments and reducing the side-effects of the techniques currently used. This way, the synthesis of gold nanoparticles was firstly performed aiming to use them as seeds to grow an AuFe shell afterwards. Throughout all the process, the protocols used were optimized and the nanoparticles were characterized on every step of the way. Finally, the main goal of this Master thesis seems not to have been achieved, however it was possible to synthesize colloiddally stable nanoparticles with a mean size of 3,3 nm containing 20% of iron and 80% of gold.

Keywords

Hybrid Magneto-Plasmonic Nanoparticles; Core-Shell; NIR-Responsive; Nanorods

Resumo

O cancro é uma das maiores causas de morte no mundo por isso é cada vez mais importante melhorar os tratamentos oncológicos e promover um diagnóstico precoce. Assim sendo, muitas alternativas em nanotecnologia têm sido investigadas nas últimas décadas com vista à implementação de novas estratégias de combate a esta e outras doenças. Nesta dissertação, pretendeu-se sintetizar nanopartículas magneto-plasmónicas esféricas, com um núcleo composto por ouro (Au) e um recobrimento de ouro e ferro metálico (AuFe), com a intenção de posteriormente adaptar o protocolo à síntese de nanorods com a mesma composição, que teriam a vantagem de não só combinar as propriedades óticas e magnéticas provenientes dos materiais que as constituem (ouro e ferro, respetivamente), mas também da sua natureza responsiva ao infravermelho próximo (NIR) proveniente da forma de nanorod. Assim, as nanopartículas obtidas seriam capazes de melhorar o contraste de imagem em ressonância magnética, melhorar os tratamentos por hipertermia magnética e otimizar sistemas de libertação controlada de fármacos, de uma forma não invasiva e direcionada (natureza responsiva ao NIR), reduzindo os efeitos secundários dos tratamentos atualmente utilizados. Desta forma, procedeu-se à síntese de nanopartículas de ouro e, de seguida, ao seu recobrimento com AuFe. Ao longo deste trabalho, os protocolos utilizados foram otimizados e as nanopartículas foram caracterizadas em todas as etapas do processo. Concluindo, o objetivo principal desta dissertação parece não ter sido alcançado, porém foi possível sintetizar nanopartículas coloidalmente estáveis com tamanho médio de 3,3 nm contendo 20% de ferro e 80% de ouro.

Palavras Chave

Nanopartículas Magneto-Plasmónicas; Recobrimento; NIR; Nanorods

Contents

Abstract	v
Resumo	vii
List of Figures	x
List of Tables	xiii
Acronyms	xvii
1 Introduction	1
1.1 General Concepts of Nanomaterials	2
1.2 Types of Nanomaterials According to their Dimensionality	2
1.2.1 Zero-dimensional Nanomaterials	2
1.2.2 One-dimensional Nanomaterials	3
1.2.3 Two-dimensional Nanomaterials	4
1.2.4 Three-dimensional Nanomaterials	4
1.3 Main Features of Nanoscaled Materials	5
1.3.1 Size Effects	5
1.3.2 Shape Effects	7
1.4 Hybrid Nanomaterials	7
1.4.1 Magnetic Nanoparticles	11
1.4.2 Plasmonic Nanoparticles	14
1.4.3 Hybrid Magneto-Plasmonic Nanoparticles	16
1.4.4 Brief state-of-the-art of Au-Fe based Nanorods	18
2 Materials and Methodologies	21
2.1 Materials	22
2.1.1 AuNPs Seeds Synthesis	22
2.1.2 Au-AuFe Core-Shell NPs Synthesis	22
2.2 Characterization Techniques	22
2.3 Au-AuFe Core-Shell NPs Synthesis	24
2.3.1 AuNPs Seeds Synthesis	24

2.3.2	Au-AuFe Core-Shell NPs Synthesis	24
3	Results and Discussion	27
3.1	AuNPs Seeds	28
3.1.1	Protocol Selection	28
3.1.1.A	First Protocol	28
3.1.1.B	Second Protocol	29
3.1.2	Calculation of Gold Concentration	31
3.2	Au-AuFe Core-Shell Nanoparticles Synthesis	32
3.2.1	First Protocol	32
3.2.2	Second Protocol	35
3.2.2.A	Synthesis with Au(COOCH ₃) ₃	35
A –	SS21	36
B –	SS22	39
C –	SS30	40
D –	SS33	42
D –.1	SS33-Supernatant	44
3.2.2.B	Synthesis without Au(COOCH ₃) ₃	47
3.2.3	UV-visible Spectroscopy	51
4	Conclusions and Future Work	53
	Bibliography	55
A	AuNPs seeds: Synthesis and Characterization	63
B	Au-AuFe Nanohybrids: Synthesis and Characterization	67

List of Figures

1.1	Classification of nanomaterials based on dimensionality.	5
1.2	Size effects.	6
1.3	Optical Properties of Gold Nanoparticles.	6
1.4	Types of hybrid nanoparticles.	10
1.5	Types of magnetic behaviors.	13
1.6	Plasmonic properties of gold nanorods.	15
1.7	UV-Vis spectrums of AuNPs exhibiting different shapes.	16
2.1	AuNPs seeds synthesis protocol.	24
2.2	Au-AuFe Core-Shell NPs synthesis protocol.	25
3.1	First AuNPs seeds synthesis protocol.	28
3.2	Comparison (UV-visible spectrum and respective TEM images) between the two protocols (samples SS03 and SS09) used to synthesize AuNPs.	30
3.3	First Au-AuFe core-shell NPs synthesis protocol.	32
3.4	Characterization results of synthesis SS20 and respective AuNPs seeds (SS19): UV-visible spectra and TEM images with 200kX of magnification.	33
3.5	HRTEM images of sample SS20 and respective crystalline plan analysis with Digital Microsoft.	34
3.6	TEM-EDX results of sample SS20.	34
3.7	High resolution XPS spectrum of energy ranges corresponding to Fe 2p of sample SS20.	35
3.8	Characterization results of synthesis SS21 and respective AuNPs seeds (SS18): UV-visible spectra and TEM images with 200kX and 150kX of magnification, respectively.	36
3.9	HRTEM images of sample SS21 and respective crystalline plan analysis with Digital Microsoft.	37
3.10	TEM-EDX results of sample SS21.	37
3.11	High resolution XPS spectrum of energy ranges corresponding to Fe 2p of sample SS21.	38

3.12 XRD results of sample SS21 together with the Au (0011140) and Fe ₃ O ₄ (00-019-0629) peaks.	39
3.13 Characterization results of synthesis SS22 and respective AuNPs seeds (SS18): UV-visible spectra and TEM images with 250kX and 150kX of magnification, respectively. . .	39
3.14 Characterization results of synthesis SS30 and respective AuNPs seeds (SS29): UV-visible spectra and TEM images with 200kX of magnification.	40
3.15 HRTEM images of sample SS30 and respective crystalline plan analysis with Digital Microsoft.	40
3.16 TEM-EDX results of sample SS30.	41
3.17 High resolution XPS spectrum of energy ranges corresponding to Fe 2p of sample SS30.	41
3.18 Characterization results of synthesis SS33 and respective AuNPs seeds (SS32): UV-visible spectra and TEM images with 150kX and 200kX of magnification, respectively. . .	42
3.19 HRTEM images of sample SS33 and respective crystalline plan analysis with Digital Microsoft.	43
3.20 TEM-EDX results of sample SS33.	43
3.21 High resolution XPS spectrum of energy ranges corresponding to Fe 2p of sample SS33.	44
3.22 Characterization results of supernatant of synthesis SS33 and respective AuNPs seeds (SS32): UV-visible spectra and TEM images with 250kX and 200kX of magnification, respectively.	45
3.23 HRTEM images of the supernatant of sample SS33 and respective crystalline plan analysis with Digital Microsoft.	45
3.24 TEM-EDX results of supernatant of sample SS33.	46
3.25 Characterization results of synthesis SS24 and respective AuNPs seeds (SS23): UV-visible spectra and TEM images with 200kX and 150kX of magnification, respectively. . .	48
3.26 TEM images of samples SS24 and SS25.	49
3.27 HRTEM image of sample SS24 and respective crystalline plans analysis with Digital Microsoft.	50
3.28 TEM images of sample SS33 at 10', 30' and 60' of reaction.	50
3.29 Schematic diagram of UV-visible spectroscopy with double beam optical system.	51
3.30 UV-visible spectra using both toluene and hexane as reference, and respective peak wavelengths.	52
A.1 Characterization results of synthesis SS01: UV-visible spectrum, TEM image with 250kX of magnification and size distribution histogram.	64
A.2 Characterization results of synthesis SS02: UV-visible spectrum, TEM image with 250kX of magnification and size distribution histogram.	64

A.3	Characterization results of synthesis SS03: UV-visible spectrum, TEM image with 250kX of magnification and size distribution histogram.	64
A.4	Characterization results of synthesis SS04: UV-visible spectrum, TEM image with 250kX of magnification and size distribution histogram.	64
A.5	Characterization results of synthesis SS09: UV-visible spectrum, TEM image with 200kX of magnification and size distribution histogram.	65
A.6	Characterization results of synthesis SS10: UV-visible spectrum, TEM image with 250kX of magnification and size distribution histogram.	65
A.7	Characterization results of synthesis SS11: UV-visible spectrum, TEM image with 150kX of magnification and size distribution histogram.	65
B.1	SS20 Histogram and SS19 (respective AuNPs) Histogram.	68
B.2	SS21 Histogram and SS18 (respective AuNPs) Histogram.	68
B.3	SS22 Histogram and SS18 (respective AuNPs) Histogram.	69
B.4	SS30 Histogram and SS29 (respective AuNPs) Histogram.	70
B.5	SS33 Histogram and SS32 (respective AuNPs) Histogram.	70
B.6	UV-visible spectra of sample SS33 at 10', 30' and 60' of reaction, and respective AuNPs (SS32).	71
B.7	SS33 supernatant Histogram and SS32 (respective AuNPs) Histogram.	71
B.8	Characterization results of synthesis SS25 and respective AuNPs seeds (SS23): UV-visible spectra and TEM images with 200kX of magnification.	72
B.9	Characterization results of synthesis SS27 and respective AuNPs seeds (SS26): UV-visible spectra and TEM images with 100kX of magnification.	72
B.10	Characterization results of synthesis SS28 and respective AuNPs seeds (SS26): UV-visible spectra and TEM images with 150kX and 100kX of magnification, respectively.	72
B.11	General XPS spectrum results of sample SS20.	73
B.12	General XPS spectrum results of sample SS21.	73
B.13	Repeated measurements of the general XPS spectrum results of sample SS21.	73
B.14	General XPS spectrum results of sample SS30.	74
B.15	General XPS spectrum results of sample SS33.	74
B.16	General XPS spectrum results of the supernatant from sample SS33.	74
B.17	High resolution XPS results for Au of sample SS20.	75
B.18	High resolution XPS results for Au of sample SS21.	75
B.19	High resolution XPS results for Au of sample SS30.	76
B.20	High resolution XPS results for Au of sample SS33.	76

List of Tables

3.1	Concentration of AuNPs: comparison of results between ICP and UV-Vis spectroscopy. .	31
3.2	Au-AuFe nanoparticles synthesis with gold precursor. The number of magnets beside each sample represents, qualitatively, the magnitude of the magnetic susceptibility of the sample.	36
3.3	Au-AuFe nanoparticles synthesis without gold precursor. The number of magnets beside each sample represents, qualitatively, the magnitude of the magnetic susceptibility of the sample.	47
A.1	Reagents quantities used on the first AuNPs seeds synthesis protocol.	63
B.1	Binding energy profiles of Fe 2p.	69
B.2	Binding energy profiles of Au 4f.	69

Acronyms

AuNPs	Gold Nanoparticles
AuNRs	Gold Nanorods
CNTs	Carbon Nanotubes
EDX	Energy-Dispersive X-ray Spectroscopy
HRTEM	High Resolution Transmission Electron Microscopy
ICP-MS	Inductively Coupled Plasma Mass Spectrometry
IONPs	Iron Oxide Nanoparticles
LSPR	Localized Surface Plasmon Resonance
MNPs	Magnetic Nanoparticles
MPI	Magnetic Particle Imaging
MRI	Magnetic Resonance Imaging
NIR	Near-Infrared
NPs	Nanoparticles
ODE	Octadecene
OLAc	Oleic Acid
OLAm	Oleylamine
PAI	Photoacoustic Imaging
QDs	Quantum Dots
SEM	Scanning Electron Microscopy
SERS	Surface-Enhanced Raman Spectroscopy
SPIONs	Superparamagnetic Iron Oxide Nanoparticles
SPR	Surface Plasmon Resonance
T_B	Blocking Temperature

T_C	<i>Curie</i> Temperature
TEM	Transmission Electron Microscopy
T_N	<i>Néel</i> Temperature
XPS	X-ray Photoelectron Spectroscopy
XRD	X-Ray Diffraction

1

Introduction

Contents

1.1 General Concepts of Nanomaterials	2
1.2 Types of Nanomaterials According to their Dimensionality	2
1.3 Main Features of Nanoscaled Materials	5
1.4 Hybrid Nanomaterials	7

1.1 General Concepts of Nanomaterials

A nanomaterial can be defined as a material that have at least one critical dimension inferior to 100 nm¹ and a nanostructure is said to have one dimension, the length for example, larger than 100 nm in one direction only,² providing a great range of possibilities in the nanotechnology world. The synthesis, assembly and fabrication of nanomaterials have been widely investigated in the last decades owing to their variety of applications,³ that go from nanodevices and nanoelectronics to a myriad of medical applications. For instance, in biomedical applications, nanomaterials can be found in drug delivery systems and also in various imaging techniques. Thus, providing not only more effective treatments against various diseases but also its early diagnosis.

This way, novel methods for fabricating patterned nanostructures as well as new device concepts are constantly being discovered,³ and in the next decades it is expected that nanotechnology will present a wide range of applications in almost all sectors of technology and industry, providing new opportunities to discover various mundane products such as electronics, medicines, cars, homes, computers, etc., that are better, cheaper and require fewer raw materials⁴ than the ones used nowadays.

1.2 Types of Nanomaterials According to their Dimensionality

From the point of view of their dimensionality, nanomaterials can be classified as nanomaterials with zero dimensions (0D), one dimension (1D), two dimensions (2D) and three dimensions (3D) within the nanoscale.⁵

1.2.1 Zero-dimensional Nanomaterials

0D nanomaterials correspond to those where all dimensions are less than 100 nm,⁶ and nanoparticles are the most common representation of these materials. Nanoparticles (NPs) can be amorphous or crystalline, metallic, ceramic or polymeric, exhibiting various shapes and forms² (hollow spheres, nanolenses, core shell QDs, among other configurations⁶). Concerning its synthesis, there are two approaches to be considered: top-down and bottom-up, in which the top-down approach deals with the breaking down of larger particles by an external applied force and the bottom-up approach deals with larger molecules composed of a multitude of smaller molecules.⁶ Depending on their composition, NPs can present different properties, being able to give rise to applications concerning almost all fields of study: from nanoparticle-based technologies to food packaging, batteries and supercapacitors, nanoceramics and nanomedicine.⁷

Quantum Dots (QDs) are one of the most studied 0D nanomaterials due to its quantum confinement effect arising from the ultra-small size. This is translated in great electronic and optical properties,

being QDs able to emit light of any wavelength by changing their size: larger-sized QDs emit large wavelengths (e.g., red light), smaller QDs emit the small wavelengths (e.g., blue light) and intermediate-sized QDs can emit green light and other colors depending on the size of the QDs,⁶ therefore some of its applications include chemical sensing, biosensing, bioimaging, light-emitting diodes (LEDs), drug delivery, photodynamic therapy, photocatalysis and electrocatalysis.⁸

1.2.2 One-dimensional Nanomaterials

1D nanomaterials are defined as materials with one dimension greater than 100 nm within the nanoscale,⁶ which include nanotubes, nanowires and nanorods. Some of its properties include high conductivity and excellent mechanical deformability due to its configuration that ensures a direct conductive path for the transport of charges and decreases the grain boundaries or defects.⁹

Nanotubes made of carbon, namely Carbon Nanotubes (CNTs) present chemical composition and atomic bonding arrangements that are very simple but have diversity and richness in all nanostructures, provided by its twist (or chirality) that affects the conductance, density, lattice structure, and other properties of the nanotube.⁶ CNTs present good optical and electrical properties, and its electrical conductivity, i.e., whether it shows metallic or semiconductor behavior, is mainly depend on its structural properties. Due to these properties, CNTs present a high number of applications in the optical field, particularly in the areas of infrared optical communication and diagnostic technology.⁶ They present excellent mechanical properties as well, since it requires a large amount of energy to break its bonds and therefore break a nanotube. Due to their strength, lightweightness and elasticity, CNTs are very promising candidates as probes in scanning microscopy. Finally, CNTs have showed very high thermal conductivity, which becomes very significant when the size of electronic and mechanical devices is decreased down to the nanoscale.⁶

Nanowires can be defined as structures that have two dimensions constrained to 100nm and an unconstrained longitudinal size.² Its unique geometry and physical properties make it possible to integrate them into vast application domains such as electronics, optics, heat, photovoltaics, biology, chemistry, and mechanics.¹⁰

Finally, nanorods terminology is considered when all three dimensions are below 100 nm being one of them the largest one (namely, whose length is two to twenty times longer than their width¹¹). Nanorods can be obtained from semiconductors or metals. Gold Nanorods (AuNRs) are one of the most studied 1D systems due to their significant optical extinction coefficients and narrower line widths (these concepts are deeply explained in section 1.4.2), giving rise to high photothermal conversion efficiencies and excellent sensitivity to local dielectric constant shifts.¹¹ These properties have given rise to various exciting possibilities in the biomedicine field where, for instance, AuNRs can be functionalized with antibodies to detect selected biomolecules.⁶

In contrast to 0D nanomaterials, progress in 1D nanostructures has been delayed because of various difficulties associated with synthesis issues as, mainly, the control of morphology, purity, and chemical composition.⁶

1.2.3 Two-dimensional Nanomaterials

2D nanomaterials correspond to those in which two dimensions are on the microscale and one dimension at nanoscale, and are typically plate-like including nanofilms, nanocoatings, and nanolayers. These nanomaterials are synthesized by deposition on the substrate as a single layer or multilayered structures and because of their interesting surface and electronic properties, have become a huge source of research in the field of solar energy.⁶

Nanocoatings corresponds to a coating of fine and thin layers of polymeric material within the nanoscale on the surface of a substrate (metal, polymer, glass or ceramic), in which different techniques are applied such as physical vapor deposition, chemical vapor deposition, and others.⁶ Comparing to the convectional coatings, nanocoatings present superior properties, such as enhanced chemical stability, hardness, wear resistance, toughness, and low friction, providing the opportunity of being incorporated on magnetic storage devices, automotive applications, high-speed machining and tooling, and biomedical and optical devices.⁶

Nanofilms are thin layers of material ranging from fractions of nanometers to several micrometers in thickness,¹² and are formed by deposition of layer by layer on the substrate surface.⁶ During its preparation, it's possible to control its physical, optical, mechanical, and electrical properties by changing some deposition parameters (substrate temperature, deposition rate, purity of deposited material, angle of incidence, environmental conditions, and energy of depositing particles).⁶ Its attractive properties create many possibilities of applications especially in the biomedical field.¹³

1.2.4 Three-dimensional Nanomaterials

3D nanomaterials can be defined as nanomaterials with all dimensions larger than 100nm.⁶ There are several methods of synthesis for these types of nanomaterials, being the classical ones the chemical precipitation, Sol-Gel, hydrothermal method, solvothermal method, thermal decomposition, microemulsion and chemical vapor.¹⁴

Concerning its definition, because their dimensions are larger than 100nm, it is a controversial matter to consider them as a type of nanomaterial, but there is not a lot research done regarding this, comparing to 0D, 1D, and 2D nanomaterials.⁶

A summary of all these concepts is represented on Figure 1.1.

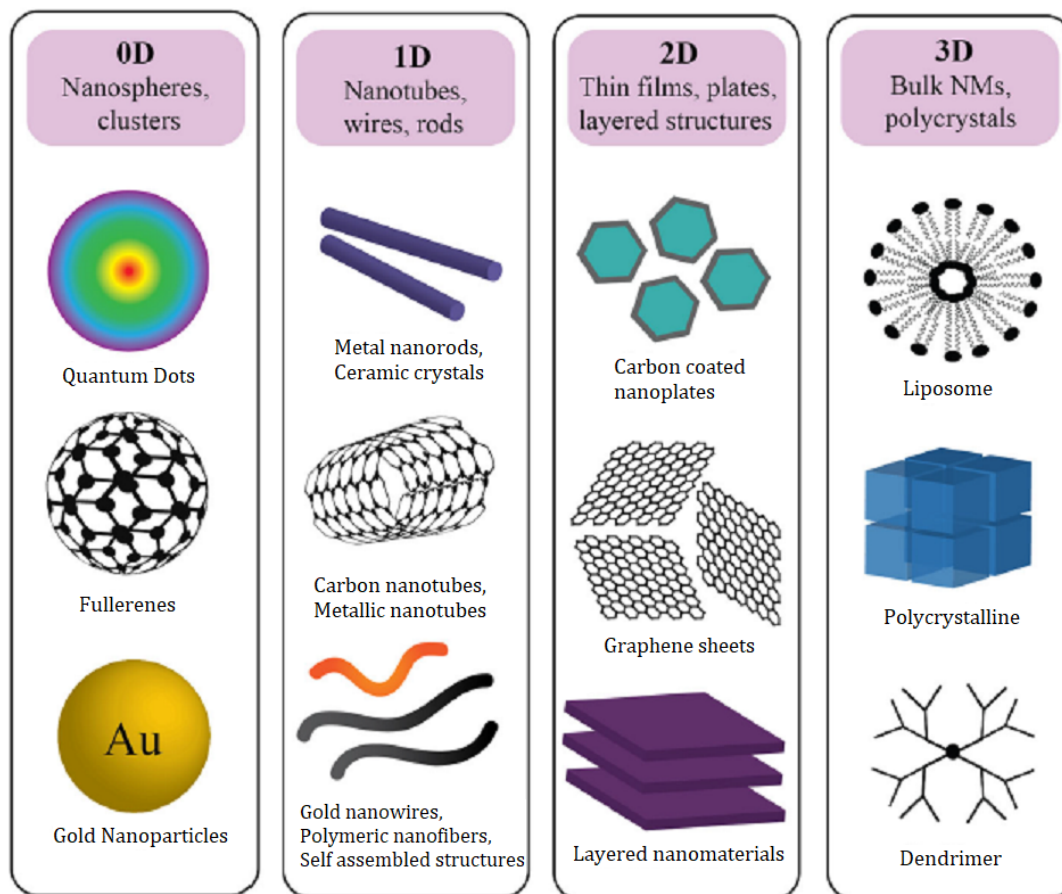


Figure 1.1: Classification of nanomaterials based on dimensionality.¹⁵

1.3 Main Features of Nanoscaled Materials

In this section, two main features of nanomaterials will be explained: size and shape effects.

1.3.1 Size Effects

One of the most important effects on nanoparticles is the increased surface area-to-volume ratio. As demonstrated by Figure 1.2, from a cubic microparticle of 20 μm we can obtain 8 cubic microparticles of 10 μm and 64 cubic microparticles of 5 μm , meaning that the surface area increases with the decreasing of particle size. This feature provides to NPs a higher contact area between the NPs surface and the reaction medium, highly increasing its reactivity¹⁶ in comparison to micro-sized particles.

Also, as the size decreases, both chemical and physical properties change. This way, nanomaterials exhibit different physical properties in relation to bulk materials, including electrical, catalytic, magnetic, mechanical, thermal, or imaging features providing applications on medical, pharmaceutical and different engineering sectors.¹⁷

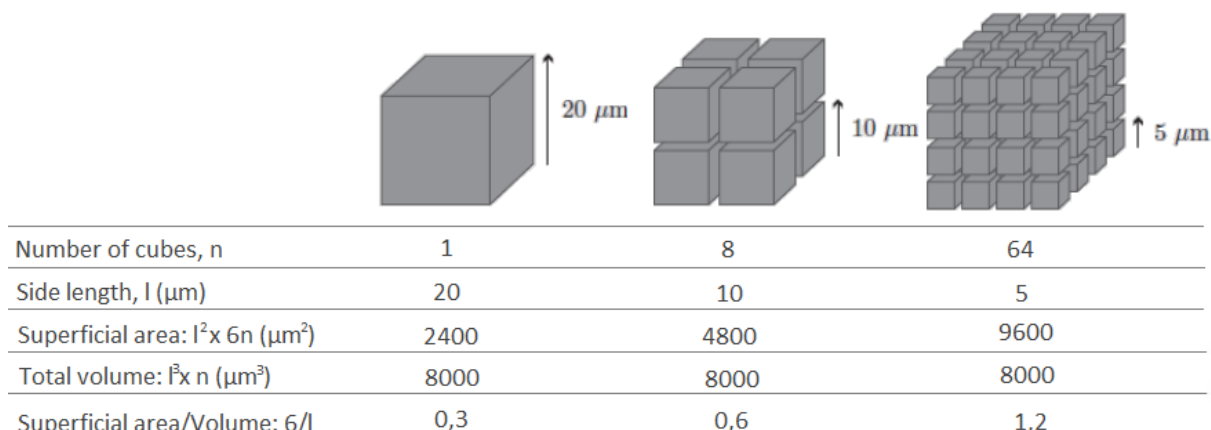


Figure 1.2: Size effects.¹

The specific heat is observed to increase with the decrease in particle size, whereas both the melting entropy and enthalpy decrease as the particle size decreases.¹⁸ Because nanomaterials have a much larger surface area-to-volume ratio than bulk materials, its thermodynamic and thermal properties are drastically different, leading to a melting point depression: nanomaterials are able to melt at temperatures hundreds of degrees lower than bulk materials,¹⁷ which has been predicted based on size-dependent cohesive energy (i.e. basic thermodynamic property used to predict melting temperature, melting enthalpy, melting entropy and specific heat of nanomaterials).¹⁸

Due to its nano size, NPs are small enough to confine their electrons and produce quantum effects, presenting unexpected optical properties.¹⁷ One example is demonstrated on Figure 1.3, in which we can see that gold particles present different colors depending on their size.

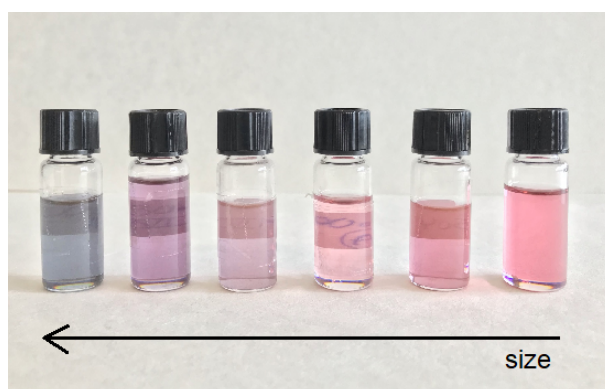


Figure 1.3: Optical Properties of Gold Nanoparticles.

Regarding the size effects on magnetic properties, it has been demonstrated that the size reduction of magnetic nanoparticles affects its main magnetic parameters, such as the magnetic moment (decreasing it and thus reducing its saturation magnetization¹⁹) and blocking temperature. These effects are further addressed in section 1.4.1.

Particularly for biomedical applications, NPs are extremely interesting due to their size, providing great advantages in relation to bigger-sized particles. Such advantages include its enhanced solubility, improving its bioavailability and clearance.²⁰

Concluding, depending on the material, properties like solubility, transparency, color, absorption, or emission wavelength, conductivity, melting point, and catalytic behavior can be changed only by varying the particle size.¹⁷

1.3.2 Shape Effects

In the last few decades, advances in the synthesis methods and characterization techniques of NPs have enable the control over its shape and morphology.²¹ This way, different shapes have been widely investigated and, particularly, for gold nanoparticles, there has been demonstrated that they can present shapes like a nanosphere, nanoshell, nanocage, nanorod, nanotube, nanowire and nanostar.²² Nevertheless, the most common shape presented by nanomaterials is still a spherical shape that is adopted by liquid nanoparticles and isotropic solids, as it is the shape that minimizes the surface area-to-volume ratio.¹

In fact, even though crystals acquire a polyhedral shape on the initial phases of crystallization, above its roughening temperature, the energy gap between different planes fade, and the crystal shape changes from polyhedral to spherical,¹ which is considered the lowest-energy shape.

Regarding shape effects on magnetic properties, it has been reported that ellipsoidal (solid and hollow) magnetite NPs present lower magnetization values and high coercivity when compared to spherical (solid) NPs which was attributed to the increased surface spin canting effects in ellipsoidal shaped NPs.¹⁹

Shape effects on nanomaterials also can affect their optical properties, namely for Gold Nanoparticles (AuNPs) there is an alteration of color depending on their shape: they exhibit a pale orange color associated with a spherical shape and a red violet color associated with a rod shape.⁵

Particularly, the control over their shape provides its usage to tailor functional properties for specific biomedical and technological applications.²¹ In fact, the size and shape effect are found prominent in nanostructures up to the size limit of approximately 30nm, however the effect of size and shape becomes less significant as the size is more than 30 nm.²³

In conclusion, the fact that its properties are size and shape dependent is what provides such interesting features and great potential on all sorts of applications.¹

1.4 Hybrid Nanomaterials

Hybrid nanomaterials are nanomaterials composed by at least two different materials. These materials are typically inorganic components (metal ions, metal clusters or particles, salts, oxides, sulfides, non-

metallic elements and their derivatives, etc.) or organic components (that ranges from simple organic molecules to advanced molecular architectures and organic polymers),²⁴ meaning that we can have hybrid nanomaterials that are inorganic-organic, organic-organic or inorganic-inorganic.

The combination of organic and inorganic components represents an easy and convenient way for the development of innovative properties.²⁴ Particularly, hybrid inorganic-organic 1D nanomaterials has been increasingly researched for its synergistic behavior directly bounded to the charming characteristics of 1D nanomaterials. The initial motivation for introducing organic molecules into inorganic nanostructures was to improve its stability for being used in future practical applications, in which 1D hybrid nanomaterials are very useful. In fact, 1D hybrid nanomaterials possess improved colloidal stability by passivating the 1D inorganic surface, reducing the surface tension, and even solubilizing them in solution.²⁵ The combination of organic and inorganic components in a controlled manner can evidently enhance the complexity and functionality of the 1D nanomaterial. For instance, a 1D inorganic nanostructure can present toxicity which makes them not suitable for biomedical applications since it cannot realize its optical or electronic function without damaging the organism, but this problem can be reverted if its surface is coated with biocompatible polymers or biomacromolecules (organic compounds). Still concerning its biomedical applications, it is possible to incorporate stimuli-responsive polymers into 1D inorganic structures in order to create structures that are suitable for biomedical applications and can be controlled through external environment variations. Sometimes, an advantage of 1D nanohybrids in relation to 1D inorganic nanomaterials is that they are easy to scale up, because the organic phase of 1D hybrid nanomaterials facilitates a low-cost production. Finally, 1D organic-inorganic nanostructures are often necessary as an intermediate for the preparation of pure inorganic or organic materials, especially in the case of porous 1D objects with ultra-large surface areas.²⁵ In its synthesis process, organic compounds are easily modifiable and are used as building blocks for hybrid polymeric materials, as for the inorganic counterparts, they allow the construction of coordination polymers with metals directly incorporated in the polymer chains and frameworks. This flexible nature of the metal–ligand coordination bonds enables the formation of nanohybrids capable of adaptive recognition of chemical environments, which ensures dynamic selectivity towards particular reactants in complex mixtures.²⁴ The main interest associated with the synthesis of hybrid organic-inorganic nanostructures, is that new appealing properties can be attained through the interfacial interaction of organic and inorganic phases in a sole nano-object.²⁵ Hence, it drastically enhances both physicochemical properties of the organic and inorganic materials that compose them, leading to a wide range of possible applications, such as photoactive devices, photocatalysis, high-performance electrochemical capacitors, solar cells, or electronic, optoelectronic, electrochemical, and electromechanical nanoscale devices.^{24,25} Concerning biomedical applications, hybrid organic-inorganic biomaterials can be used in various biomedical fields, with the ultimate goal of efficiently diagnosing and treating various human diseases.²⁶

Hybrid organic-organic nanomaterials consists in the incorporation of at least two organic compounds, generally polymer-based, in the same nanomaterial, providing a huge interest for biomedical applications, since polymer-hybrids can change biodistribution, solubility and improve the system stability, consequently increasing bloodstream circulation time, as well as maintain biological actions.²⁷ The incorporation of polymers on these type of nanomaterials is very useful concerning drug delivery applications, since it stabilizes and improves the therapeutic activity of the drug, providing more effective drug delivery systems. Regarding the synthesis process, it is possible to create polymer-hybrid nanomaterials by attaching synthetic polymers at atomic level instead of blending them, resulting in a very advantageous process, since it enables to combine the desired properties of both polymers without the disadvantage of separation phase, which is generally seen when polymers are blended together.²⁷ The main purpose of this newly interesting method is to increase conjugates solubility and/or stability, thus decreasing the toxicity of the system. The toxicity issue is more relevant on biomedical applications and by attaching polymers at the atomic level to create polymer-based hybrid nanomaterials this problem is solved, making it possible for instance to deliver cytotoxic drugs, such as anti-tumor agents that nowadays are based on conventional systemic biodistribution and present low specificity and selectivity.²⁷ This way, the development of new strategies focused on finding biocompatible hybrid materials has led to remarkable advancements in the biomedical field on finding more effective, non-toxic drug delivery carriers capable of reaching specific places such as tumor sites, providing a slow, controlled release of the drug, while protecting it from degradation and enhancing its circulation time on the blood stream of the patient. Furthermore, blending organic compounds (such as phospholipids, proteins and lipids) to natural or synthetic polymers can result in novel hybrid nanosystems capable of combining the advantages of these biomacromolecules to those of the synthetic polymers.²⁷

Inorganic-inorganic nano hybrids are defined as hybrid nanosystems composed by two or three major inorganic components. By joining various inorganic compounds in the same nanomaterial, we can obtain nano hybrids with potential multifunctional properties, since the coupling of multiple inorganic nanomaterials lead to a resulting nano hybrid with better therapeutic efficacy than their individual counterparts: if an individual inorganic compound is not suitable for a specific function into the desired application, it is possible to combine it with another inorganic compound which can improve a novel property to the nano hybrids. In particular, for biomedical applications, hybrid inorganic-inorganic nanomaterials improve both physical and chemical stabilities, in vivo clearance, biocompatibility, and biodegradability to a large extent compared to their individual forms.²⁸ The novel properties acquired by these hybrid materials are hard to achieve by conventional solid-state reactions, therefore it is important to explore other synthesis methods such as chemical vapor deposition, Langmuir–Blodgett technique, self-assembly and intercalation reaction methods. Similarly to organic-organic hybrids, inorganic-inorganic hybrid nanomaterials also have provided a multi-purpose system for the transportation of a variety of anticancer and diag-

nostic agents, providing newly drug delivery systems that have great advantages over the conventional ones, such as improved drug-retaining ability, better pharmacokinetic properties, well-controlled release properties, and a targeted therapeutic approach.²⁸ Besides drug delivery, these types of nanohybrids can be used in a wide range of applications like phototherapy and bio-imaging, including optical (visible, IR, NIR, NIR-II), magnetic resonance imaging, X-ray, nuclear and photo-acoustic imaging.²⁸ Therefore, such nanomaterials have brought huge opportunities to the biomedical field, with the biggest difficulty being associated with toxicity issues, limiting its clinical applicability.

Whether it incorporates inorganic and/or organic materials, hybrid nanostructures can have different architectures concerning the arrangement of the organic and inorganic species. Figure 1.4 demonstrates some of the most common architectures that can be found: structure (A) represents the most simple distribution of both materials, in which both phases are dissolved in each other in a homogeneous way, structure (B) exhibits phase separation of both materials, disposed in a core-shell type of structure, structure (C) represents a scattered-type structure, in which the scattered phase can be in the entire structure, in the shell or in its core. Finally, a multiblock structure is represented by (D), being the first example di-block and the second one tri-block.²⁵

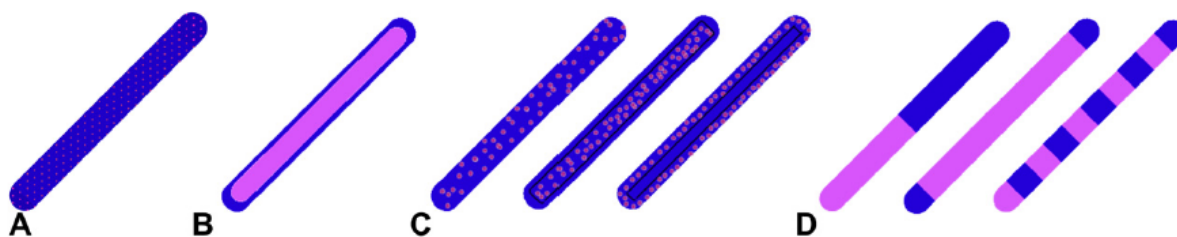


Figure 1.4: Types of hybrid nanoparticles.²⁵

Besides the structures demonstrated on Figure 1.4, it is possible to observe other not so common architectures, such as core-shell, yolk-shell, heterodimer, Janus, dot-in-nanotube, dot-on-nanorod, nanobranches, etc.²⁹ This way, by combining these different architectures with a variety of different materials, there is a vastly wide range of possibilities for hybrid nanoparticles, leading to some interesting combination of properties regarding the materials chosen, such as magnetic/luminescent, plasmonic/-catalytic or magnetic/catalytic.

The spatial arrangement of the inorganic and organic phases not only determines the intrinsic properties and functions of the resulting hybrid, but also relates directly to different synthetic strategies.²⁵ Moreover, by combining different structures observed on Figure 1.4, it is possible to have innovative structures with improved properties. For instance, on structures (B) and (D) of Figure 1.4, the organic or inorganic block can be substituted by a hybrid one, originating a novel structure. This way, it is to be expected that new architectures will be explored in the future.

Mainly, the interesting thing about these hybrid nanostructures is that by combining different materials, their individual properties can be changed in order to create hybrid materials with new and unique features, not only by the accumulating of functions or properties into a single structure but also by creating new ones in a synergistic way.²⁹

The research and development of hybrid nanomaterials provides an outstanding driving force for the progress in several research fields, resulting into the development of new technologies, including new platforms for drug delivery and stimuli-responsive smart materials and sensors, to facilitate various sectors of industrial technologies, materials science, nanomedicine and energy applications.

This master thesis focuses on the synthesis of inorganic-inorganic hybrid nanoparticles, containing gold and iron in the same nano-object, thus combining optical and magnetic properties, respectively.

1.4.1 Magnetic Nanoparticles

Magnetic Nanoparticles (MNPs) are defined as particles with a size smaller than 100nm that reacts to an external magnetic field. MNPs have very interesting properties, as it not only possess general properties of NPs but also magnetic properties, making them suitable for applications in various different fields.

MNPs are mainly metal alloys NPs, metal oxide and metal NPs, and present important properties such as excellent reactivity, a larger surface-to-volume ratio, unique magnetic response compared to their bulk materials, including individual magnetic properties like low *Curie* Temperature (T_C), magnetic susceptibility, superparamagnetism and high coercivity.¹⁶

Concerning nanoparticles, there are two types of materials that exhibit magnetism at the nanoscale: magnetic nanomaterials that already present magnetic properties in its bulk form and nanoparticles that while in bulk are nonmagnetic, in the nanosize exhibit the appearance of magnetic features.⁵

Magnetic materials that are magnetic in bulk form are defined as materials that change their magnetic behavior as a result of an external magnetic field. Mainly, there are five types of magnetism: diamagnetism, paramagnetism, ferromagnetism, antiferromagnetism and ferrimagnetism.³⁰

Diamagnetic materials have atoms with no magnetic moment when there is no applied field,³⁰ their magnetic response to an external magnetic field is to be repelled but it's a very weak response and after its removal they do not retain any magnetic moment.⁵ All materials present diamagnetism but it is often masked by a larger paramagnetic or ferromagnetic effect.³⁰

In paramagnetic materials, according to the Langevin model, each atom has a magnetic moment which is randomly oriented as a result of thermal agitation.³⁰ Upon an external magnetic field, the atoms align along the direction of the field resulting in a weak net magnetic moment, and when the magnetic field is removed, paramagnetic materials do not have a remanent magnetization.⁵ Paramagnetic materials also show a behavior called the Curie Law, in which its atoms become harder to align to the external magnetic field applied when the thermal agitation increases provoked by an increasing of temperature.³⁰

Such materials include gadolinium, magnesium, lithium and tantalum.⁵

Ferromagnetism only occurs when the atoms of a material are arranged in a lattice and the atomic magnetic moments can interact to align parallel to each other.³⁰ Ferromagnetic materials have domains containing large numbers of atoms with parallel magnetic moments, each domain having a net magnetic moment pointing in a specific direction,⁵ and the movements of these domains determines how the material responds to an applied magnetic field:³⁰ when an external magnetic field is applied, these domains align along its direction, resulting in a large net magnetic moment, and when the magnetic field is removed there is a residual magnetic moment left.⁵ With an increasing of temperature, the thermal agitation increases as well, and for ferromagnetic materials above a certain value of temperature denominated *Curie Temperature*, the thermal agitation is so great that it causes the misalignment of its magnetic dipole moments, leading to a change from ferromagnetic to paramagnetic behavior (as demonstrated on Figure 1.5). Some ferromagnetic materials include iron, nickel and cobalt.

In antiferromagnetic materials, the coupled magnetic moments lay in opposite directions, resulting in an anti-parallel alignment of the atomic magnetic moments along the lattice, therefore the magnetic moment cancels out and the material appears to behave in the same way as a paramagnetic material.³⁰ Likewise for ferromagnetic materials, antiferromagnetic materials become paramagnetic above a certain temperature, so-called *Néel Temperature* (T_N). Antiferromagnetic materials include MnO, CoO and NiO,⁵ and the only element exhibiting antiferromagnetism at room temperature is chromium.³⁰

In ferrimagnetic materials, the magnetic coupling is antiferromagnetic and is between atoms with different magnetic moment directions occupying different lattice sites, but with different magnitudes, meaning that the magnetic moments do not cancel each other out.⁵ Hence, individual atoms on ferrimagnetic materials, under an external magnetic field, align themselves to this magnetic field, some parallel (as in ferromagnetism) and some antiparallel (as in antiferromagnetism), as demonstrated on Figure 1.5. One of the most studied ferrimagnetic materials is the magnetite.

Most elements of the periodic table present diamagnetism or paramagnetism, therefore they are often referred to as non-magnetic. On the contrary, the materials that are designated as magnetic materials are actually ferromagnetic. In pure elements at room temperature, the only other type of magnetism at state is antiferromagnetism. As for ferrimagnetism, there is no pure element that presents this type of magnetism, but can only be found in compounds, such as the mixed oxides, known as ferrites.³⁰

The direction of magnetic moments for each type of magnetic behavior is represented on Figure 1.5.

The magnetic behaviors presented in a nanoparticle is dependent on diverse factors, such as its chemical composition, crystallinity, particle shape, size and interactions between the particle and the adjacent particles.¹⁶ Among these factors, the particle size is perhaps the most relevant one, since below a specific critical diameter, magnetic nanoparticles show magnetic responses similar to paramagnetic materials, but when its magnetization is null in the absence of an external magnetic field, these are

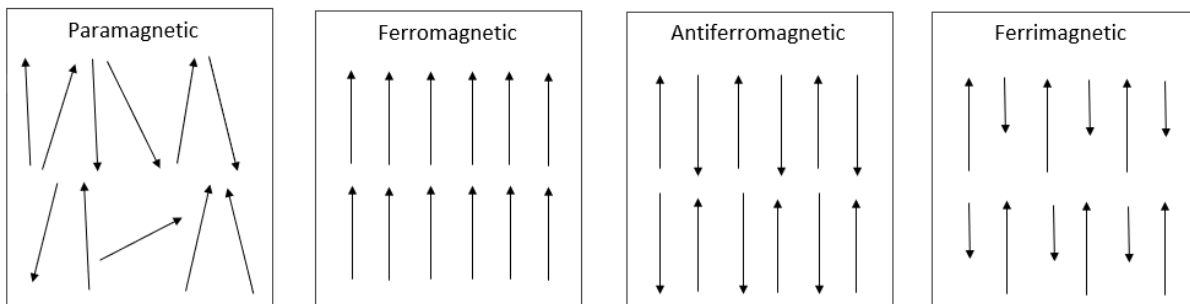


Figure 1.5: Types of magnetic behaviors.

called superparamagnetic nanoparticles.⁵ Superparamagnetic behavior can be defined as the ability of magnetic nanoparticles to show paramagnetic nature with high saturation magnetization under the influence of a magnetic field and the tendency of losing the same nature completely once the magnetic field is removed, resulting in zero magnetic remanence.¹⁹ Nanoparticles that exhibit this kind of behavior are designated by superparamagnetic nanoparticles and are currently used in applications such as drug delivery for cancer treatments or magnetic resonance imaging.

The superparamagnetism is exhibited by MNPs that are of single-magnetic-domain size: each individual nanoparticle behaves like a giant paramagnetic atom with a fast response to applied magnetic fields.²⁹ Superparamagnetic NPs exhibit superparamagnetism above a specific temperature, the so-called Blocking Temperature (T_B),¹⁹ and ferro or ferrimagnetism below this temperature. In a magnetic material, the transition from multi-domain phase to single-domain phase begins at the nanoscale. Superparamagnetic Iron Oxide Nanoparticles (SPIONs) are the most representative example of superparamagnetism.

Resuming, the size, shape, crystallinity and surface coatings of NPs play an important role on the magnetic response that a nanoparticle can present. However, these characteristics can be manipulated using different synthesis procedures.¹⁹ Regarding this, it is very important to choose the synthesis method in order to produce MNPs according to several aspects, including a monodisperse particle size distribution, size and shape control, stability, high crystallinity and desirable crystal structure.¹⁶ Some of the most used methods for synthesizing MNPs are: hydrothermal or solvothermal, coprecipitation, microemulsion, thermal decomposition, self-assembly, sol-gel and electrochemical.

Besides choosing its synthesis method according to the final application of the desired MNPs, it is also important to take into account its characterization, since the magnetic properties are very influenced by their physical and chemical properties. In this sense, several techniques have been used for determining the physicochemical characterization of these NPs: Scanning Electron Microscopy (SEM), Transmission Electron Microscopy (TEM), High Resolution Transmission Electron Microscopy (HRTEM), Energy-Dispersive X-ray Spectroscopy (EDX) and X-Ray Diffraction (XRD) are some of the most com-

monly used.

Overall, it is important to choose both synthesis and characterization techniques in order to be simple, fast and cost-effective.¹⁶

Concluding, MNPs are very promising nanoparticles to be incorporated in almost all fields of nanotechnology and nanoscience. Currently, MNPs are used in semiconductor transistors, nanocomposites, catalysis, materials for optical fibers and lasers, optical devices capacitors, biomaterials, fluids for heat transfer, and much more.¹⁶ However, their controlled synthesis in order to create MNPs with low toxicity and oxidative properties suitable for biomedical applications remains a challenge.

1.4.2 Plasmonic Nanoparticles

Some metallic NPs exhibit unique optical properties and enhanced electromagnetic field, which leads to an area of research called plasmonic effect.¹⁷ The most common nanoparticles that present this effect are gold and silver NPs which present a unique characteristic: Localized Surface Plasmon Resonance (LSPR), a strong light-matter interaction that results from the interaction between an incident light and the delocalized electrons inside conductive nanoparticles that are smaller than the incident wavelength:^{31,32} when a light beam passes through the nanoparticle, its oscillating electric field interact with the free electrons on the metal nanoparticle causing resonant oscillations, which are called surface plasmons.¹⁷ LSPR give rise to enhanced light absorption, scattering, and local confinement of the electric field near the particle's surface,^{31,33} and strongly depends on geometry, size, composition and separation between nanoparticles.³²

Surface Plasmon Resonance (SPR) is generated by a continuous film of conductor metal, in comparison to LSPR that is generated by metal NPs. Thus, biosensors implemented using LSPR present some advantages regarding the ones implemented using SPR: the optical instruments needed for LSPR are easier to use and maintain, as well as they are smaller and more affordable, since no strict temperature control is needed. However, SPR sensors have a much higher refractive index sensitivity than LSPR sensors, due to a much shorter electromagnetic decay length of NPs compared to metal films, confining the response to a smaller sensing volume, and resulting in eventual errors in experimental data.³⁴

In order to understand this phenomenon more clearly, Mie's theory³⁵ results from the resolution of Maxwell's equations and it assumes that there's a shift in the plasmon absorption to longer wavelengths when the size of the nanoparticle increases. Moreover, a slight change in particle geometry can produce a significant change in the properties of the surface plasmon absorption.³⁶ For instance, comparing gold nanospheres that are isotropic (i.e. presents uniform behavior in all directions) with gold nanorods that are anisotropic (i.e. reacts differently depending on the direction), while isotropic gold nanospheres exhibit only one plasmon absorption band, anisotropic AuNRs reveal two plasmon absorption bands,³⁶ as demonstrated by Figure 1.6: in this case, AuNRs usually exhibit two plasmon modes, a longitudi-

nal mode that is associated with the electron oscillations along the length direction and a transverse mode associated with the oscillations along the nanorod width. Due to the longer path of the electron movements, the longitudinal mode is located at the red side of the transverse one,³⁷ meaning that its plasmonic absorption happens at a longer wavelength.

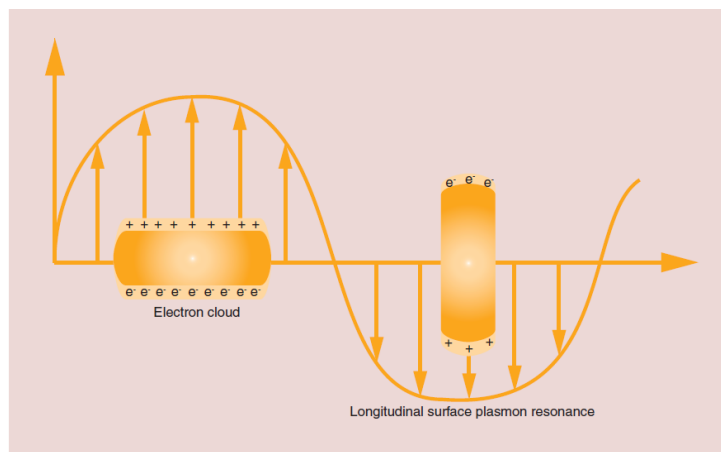


Figure 1.6: Plasmonic properties of gold nanorods.²²

Plus, under a non uniform electromagnetic field, the electron oscillations in the nanorod contain multipolar components of all orders, enabling the examination of various higher-order plasmon modes.³⁷

There are several reasons why nanorods are more advantageous than nanospheres for biomedical applications, but the most relevant one is that longitudinal plasmon resonance of nanorods can provide the absorption of wavelength radiation in the Near-Infrared (NIR) region,²² also called the biological window. The NIR region enables deep penetration in biological tissues,³⁶ providing a great innovative feature to be implemented on medical applications, since the rate of absorption of this type of radiation by the living tissue is relatively very small.²²

Relatively to the other types of nanostructures, AuNRs present more significant extinction coefficients, higher photothermal conversion efficiencies and better sensitivity to local dielectric constant shifts, giving rise to many applications regarding the use of AuNRs for NIR resonant biomedical imaging methods, such as Two-photon Lithography, Photographic Activity Test, Optical Coherence Tomography and X-ray Computed Tomography.¹¹

Due to their remarkable plasmon-related properties, AuNRs have very promising applications, not only on imaging methods but also on biomedical sensing, cancer therapy, drug delivery, nanophotonics, and optoelectronics.³⁷ Most importantly, these applications can be managed remotely by NIR light, penetrating deep into human tissue with limited invasion.

Therefore, when characterizing plasmonic NPs, it is crucial to evaluate its optical properties. Concerning AuNRs, UV-Vis spectroscopy is the most common method used: experimental studies reveal that the transversal mode verified on nanorods is situated in the visible region (at 520 nm), while the lon-

itudinal one is situated at the NIR region of the spectrum.³⁸ On Figure 1.7, there are demonstrated the UV-Vis spectrums for different shapes of AuNPs: (a) are gold nanospheres, (b) nanorods, (c) nanostars and (d) nanocages.³⁸

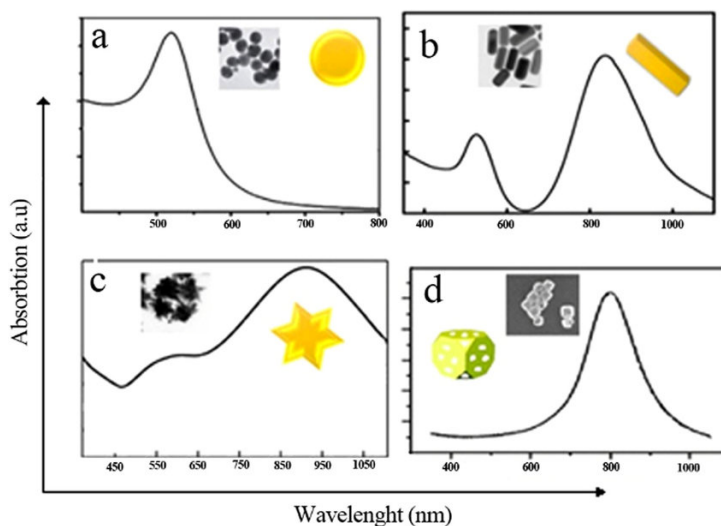


Figure 1.7: UV-Vis spectrums of AuNPs exhibiting different shapes.³⁸

Observing fig. 1.7, we can verify that not only nanorods, but also the nanostars and nanocages have peaks on NIR region.

Concluding, to optimize plasmonic NPs for specific applications, it is important to manipulate their shape in order to control its LSPR and thus enhance its optical behavior.³³ For biomedical applications, it is mandatory to make sure that these NPs present low toxicity, relatively high stability and biocompatibility, which remains a challenge to this day. However, cytotoxicity and changes caused by environmental conditions are expected to be surpassed with the help of green synthesis methods or wet chemistry synthesis upgrades.²²

1.4.3 Hybrid Magneto-Plasmonic Nanoparticles

As stated on 1.4.1, MNPs react under an external magnetic field, meaning that by manipulating this magnetic field it is possible to enhance targeting efficiencies for drug delivery and imaging applications. On the other hand, as stated on 1.4.2, plasmonic nanomaterials (for instance AuNRs) exhibit strong absorption of an incident light, being this effect stronger when LSPR occurs under the electromagnetic field with the resonance frequency. The tunability of this LSPR into the NIR region can overcome limited penetration of optical imaging systems and achieve efficient penetration into deep tissues. Therefore, to implement hybrid nanoparticles with these properties combined would be a great achievements for its usage at biomedical applications.

Nanoparticles possessing both magnetic and plasmonic properties in a single nano-object are highly

promising for image-guided therapy, being able to provide more efficient treatments by incorporating imaging properties into therapeutics (i.e. theranostic applications).³⁹

The improved properties of these types of hybrid NPs for biomedical applications are highly dependent on their shape. As demonstrated by Figure 1.7, the shape of plasmonic nanoparticles can be changed in order to be NIR responsive, which is a crucial and innovative feature concerning biomedical applications. Among all the possible shapes and conformations that these NPs can acquire, Janus NPs (i.e. NPs whose surfaces have two or more distinct physical properties) have attracted increased scientific interest in the technological and biomedical fields.

In fact, strong magnetic and NIR responsive plasmonic properties of engineered nanostars can overcome cellular and physiological barriers, target the entities of tumor environment, and induce physical therapeutic effects after being stimulated by a remote signal, thereby enabling a targeting treatment, which prevents the damage of surrounding healthy cells and limit the unwanted side effects of current treatments currently performed.⁴⁰ This represents an innovative research field on the implementation of novel drug delivery systems, since NIR-triggered controlled release of a therapeutic drug provide the possibility of releasing the drug at the right location with the desired time and drug release rate,³⁹ while providing its protections and increasing its bioavailability.

Along with drug delivery applications, hybrid magneto-plasmonic NPs can bring a number of innovations on imaging applications. The combined magnetic and NIR-responsive plasmonic properties of these type of nanoparticles enable multimodal quantitative imaging combining advantageous functions of Magnetic Resonance Imaging (MRI), Magnetic Particle Imaging (MPI), Photoacoustic Imaging (PAI) and image guided drug delivery with controllable drug release,³⁹ thus it can overcome the disadvantages of each individual imaging technique by combining advantageous features from other imaging techniques. For instance, it has been proved that core-shell nanostars with SPIONs core and a gold star-shaped plasmonic shell were bounded to drug molecules and released upon NIR illumination due to the heat generation from the nanostars.³⁹

Furthermore, it was demonstrated that Janus magneto-plasmonic nanoparticles, made of gold nanostars and iron oxide nanospheres are not only good nanoheaters for magnetic hyperthermia but also (and mostly) for photothermia.⁴⁰ Its NIR-responsive feature is advantageous for both optical imaging systems and laser-assisted biomedical applications due to the high penetration efficiency of NIR light into deep tissues³⁹ without its damaging in a non-invasive way.

Hybrid magneto-plasmonic nanoparticles have also been investigated for viral sensing, since the combination of these properties is particularly attractive for analytical science as the strong extinction band in the UV-visible region of AuNPs allows for the hybrid nanoparticles to be used as LSPR sensors, while the resonance light scattering properties make them ideal platforms for Surface-Enhanced Raman Spectroscopy (SERS) sensing.⁴¹ This way, it is possible to incorporate hybrid magneto-plasmonic

nanoparticles on viral sensors to detect for instance, the COVID-19 virus, leading to a new additional and fast approach to determine the presence of the virus in a patient and whether he needs to be isolated, treated, etc.

1.4.4 Brief state-of-the-art of Au-Fe based Nanorods

Resuming the stated on sections above, the main purpose of having hybrid nanorods incorporating both iron and gold in the same nanoparticle for biomedical applications is to take advantage of both magnetic and plasmonic properties of these structures, along with its NIR-responsive feature provided by the rod shape. Hence, we would have nanoparticles capable of taking tasks such as drug delivery, enhance contrast on imaging techniques or improve magnetically-based diseases treatments, in a non-invasive way and with less side-effects than the techniques currently used for the same purpose.

To obtain hybrid nanoparticles with both gold and iron is a great challenge, being one of the biggest problems the fact that it is still very difficult to combine them without the risk of iron oxidation. This way, there is not a lot of articles on bibliography regarding this matter, however a lot of research has been made in the last decades in relation to hybrid nanoparticles composed by gold and iron oxide, given the high stability and simplicity of synthesis of iron oxide NPs, and the excellent stability, biosafety and surface modification facility of AuNPs.⁴² Most of these hybrid NPs are core-shell shaped, and it has been showed that the room-temperature synthesis of core-shell magnetite-gold NPs are especially attractive if the gold shell completely covers the magnetic core, consequently protecting it from oxidation, minimizing possible toxicity, and enabling the functionalization with ligands.⁴³ A wide variety of synthesis methods have been investigated when researching different shapes of hybrid iron oxide and gold NPs. Various morphologies of these hybrids have already been developed including spherical and non-spherical core-shell nanoparticles, nanoflowers, nanorods, etc., leading to new interesting joined magnetic and optical properties.⁴⁴

Regarding iron-gold alloy NPs, there is just a few articles published concerning this matter, as the miscibility of these two elements is very low. The synthesis method most commonly used is laser ablation,⁴⁵ since it is a relatively simple method in which there is no need to use capping and stabilizing agents or reductants and it allows to stabilize metastable phases. However, when using this technique, the main challenge is to have control over the shape and size of the synthesized NPs. As explained on section 1.3.2, the control over its shape is crucial to determine the properties of the synthesized nanoparticles, hence it is urgent to find an alternative technique that enables this control. Regarding this, the protocol used in this Master Thesis to develop these hybrids was based on the protocol developed by Chiang et al.,⁴⁶ in which monodisperse hybrid iron and gold-based nanoparticles were obtained by the reduction of gold acetate with 1,2-hexadecanediol and thermal decomposition of iron pentacarbonyl with oleic acid and oleylamine as stabilizers. This protocol was adapted to incorporate gold nanoparticles

as seeds to grow the alliance between gold and iron, aiming, ultimately to adapt this template-based protocol and to obtain Au-AuFe core-shell nanorods.

Besides the protocol developed by Chiang et al.,⁴⁶ there is also colloidal synthesis published by Kwizera et al.,⁴² in which AuNPs smaller than 10nm can be absorbed on the surface of SPIONs via electrostatic interactions to serve as nucleation sites to grow the a gold shell and consequently form uniform iron oxide-gold core–shell NPs.

Concluding, even though there are some synthesis strategies of Au-Fe based hybrids, most studies based on these hybrids are still in a proof-of-concept stage, highlighting a need to establish detailed preclinical studies.

2

Materials and Methodologies

Contents

2.1 Materials	22
2.2 Characterization Techniques	22
2.3 Au-AuFe Core-Shell NPs Synthesis	24

2.1 Materials

The materials used in the synthesis methods explained on section 2.3 will be described in this section.

2.1.1 AuNPs Seeds Synthesis

In the synthesis of AuNPs seeds, the gold precursor used was gold (III) chloride trihydrate (Alfa Aesar, $\text{HAuCl}_4 \cdot \text{H}_2\text{O}$, 99.99%), the surfactants used were oleic acid (Aldrich, 90%) and oleylamine (Aldrich, 70%), and the solvent 1-octadecene (Aldrich, 90%). For the washing and re-dispersion of the samples, isopropanol (VWR, $\text{C}_3\text{H}_8\text{O}$, 99.9%) and hexane (Sigma-Aldrich, C_6H_{14} , 98.5%) were used, respectively.

2.1.2 Au-AuFe Core-Shell NPs Synthesis

In the synthesis of the hybrids, the iron precursor used was iron(0) pentacarbonyl (ACROS Organics, $\text{Fe}(\text{CO})_5$, 99.5%), the gold precursor used was gold (III) acetate (Alfa Aesar, $\text{Au}(\text{COOCH}_3)_3$, 99.9%), and its reducing agent 1,2-hexadecanediol (Aldrich, $\text{C}_{16}\text{H}_{34}\text{O}_2$, 90%), the surfactants used were oleic acid (Aldrich, 90%) and oleylamine (Aldrich, 70%), and the solvents tested were 1-octadecene (Aldrich, 90%) and dioctyl ether (Aldrich, 99%). For the washing and re-dispersion of the samples, isopropanol (VWR, $\text{C}_3\text{H}_8\text{O}$, 99.9%) and toluene (VWR, C_6H_{14} , $\geq 99.5\%$) were used, respectively.

The iron pentacarbonyl was handled inside a PureLab HE Glovebox in an atmosphere kept under 5ppm of oxygen, the solid materials were measured in a OHAUS pioneer analytical balance and the volumes of the liquid materials were measured with micropipettes *Transferring pipette S*.

Throughout all the synthesis, the solution was kept inside a three neck flask heated by a heating HORST mantle (60W) and with vigorous agitation from a IKA RCT Basic Hot Plate Stirrer.

The washing step of all the samples were performed in a Hettich EBA 21 centrifuge.

2.2 Characterization Techniques

The characterization techniques used to characterize the nanoparticles synthesized in this master thesis were TEM, UV-Visible spectroscopy, HRTEM-EDX, X-ray Photoelectron Spectroscopy (XPS) and XRD.

TEM: The images of TEM were carried out both in a JEOL JEM-1010 80kV microscope and in a Tecnai Spirit 120kV microscope, with EMCN copper coated grids.

UV-Vis Spectroscopy: The UV-visible spectra were obtained in a Cary 100 UV-visible spectrophotometer with Hellma Analytics QS high precision cells.

HRTEM: The images of HRTEM were carried out in a JEOL JEM-2100 200kV high resolution microscope, with 200 Mesh agar scientific holey carbon grids. The crystalline plan analysis carried out on the

HRTEM images obtained throughout all this work was performed using published data for the distance between crystalline plans of both gold⁴⁷ and magnetite.⁴⁸

EDX: EDX data was collected with an Xplore TEM of Oxford Instruments, with an Aztec control software.

XPS: XPS data was obtained with a photoelectron spectrometer (ESCA), from Physical Electronics, model PHI 5500, covering the entire periodic table of elements, with the exception of H and He, with a depth of analysis not exceeding 10 nm and with an analysis chamber in ultra-high vacuum (UHV) working in the range of 10^{-8} Torr to 10^{-9} Torr of pressure.

XRD: XRD spectrum was obtained with a *PANalytical X'Pert PRO MPD alpha1* powder diffractometer in *Bragg-Brentano* $\theta/2\theta$ geometry of 240 millimetres of radius, with a work power of 45 kV. The sample was prepared on a glass plate substract that was mounted in a standard sample holders PW1813/32.

The peak analysis performed on the XRD spectrum obtained on this work was achieved using published data for the $2-\theta$ degrees of both gold⁴⁷ and magnetite.⁴⁸

2.3 Au-AuFe Core-Shell NPs Synthesis

During this master thesis, AuNPs were synthesized to be used as seeds to grow a shell of FeAu alloy. In this section, the synthesis protocols used for both the AuNPs seeds and the final Au-AuFe NPs obtained will be explained.

2.3.1 AuNPs Seeds Synthesis

The AuNPs seeds were synthesized by a thermal decomposition method that was adapted from the protocol used by C. Shen et al.⁴⁹ In this protocol, schematized on Figure 2.1, the solvent (Octadecene (ODE)) is added to a 100mL three neck flask along with both the Oleic Acid (OLAc) and Oleylamine (OLAm) where both OLAc and OLAm act as surfactants whereas OLAm also as reducing agent, with vigorous stirring and heating at 120°C for 20 minutes. In the final part of this synthesis, the gold precursor (gold(III) chloride trihydrate, $\text{HAuCl}_4 \cdot 3\text{H}_2\text{O}$) was injected and the temperature was increased to 150°C for half an hour. An atmosphere of nitrogen was kept inside the flask throughout the entire synthesis.

Afterwards, the samples were washed with isopropanol, centrifuged for 8 minutes at 6000 RPM and re-dispersed in hexane.

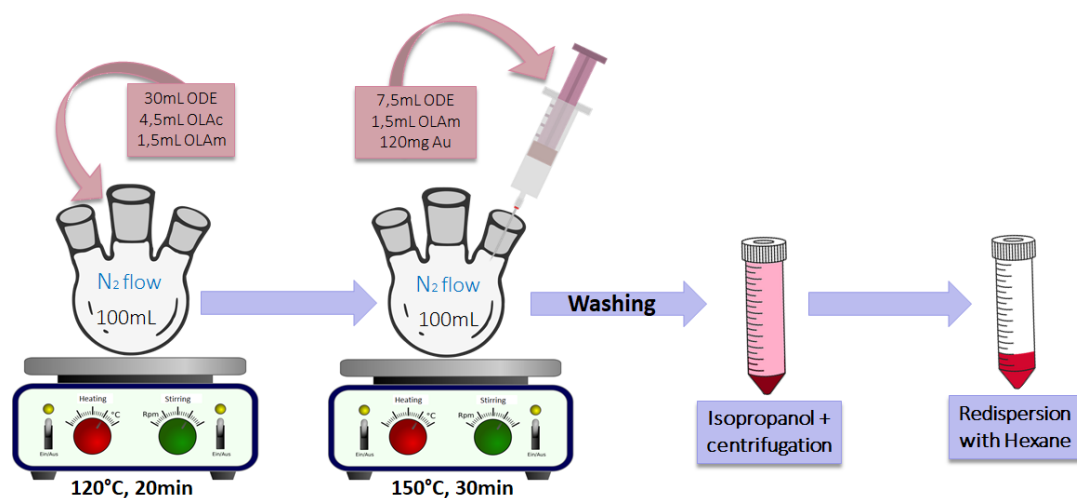


Figure 2.1: AuNPs seeds synthesis protocol.⁴⁹

2.3.2 Au-AuFe Core-Shell NPs Synthesis

The protocol used to synthesize the Au-AuFe core-shell NPs was adapted from Chiang et al.⁴⁶ and it's schematized on Figure 2.2.

In this protocol, the AuNPs (Section 2.3.1) were used as seeds to grow a AuFe shell via the reduction of gold (III) acetate, $\text{Au}(\text{COOCH}_3)_3$, (used as the gold precursor) by 1,2-hexadecanediol and the

thermal decomposition of iron pentacarbonyl, $\text{Fe}(\text{CO})_5$ (i.e. iron precursor). OLAc and OLAm were used surfactants and stabilizers.

As schematized on Figure 2.2, the first part of the protocol involves keeping the mixture of AuNPs seeds, gold precursor and its reducing agent, the surfactants and the solvent, on vacuum at 120°C for 30 to 40 minutes until the hexane where the AuNPs were dispersed was totally evaporated.

Into the second part of the protocol, the $\text{Fe}(\text{CO})_5$ was injected under an atmosphere of nitrogen and the temperature was increased to 250°C for one hour.

Afterwards, the samples were washed with isopropanol, centrifuged for 8 minutes at 6000RPM and re-dispersed in toluene.

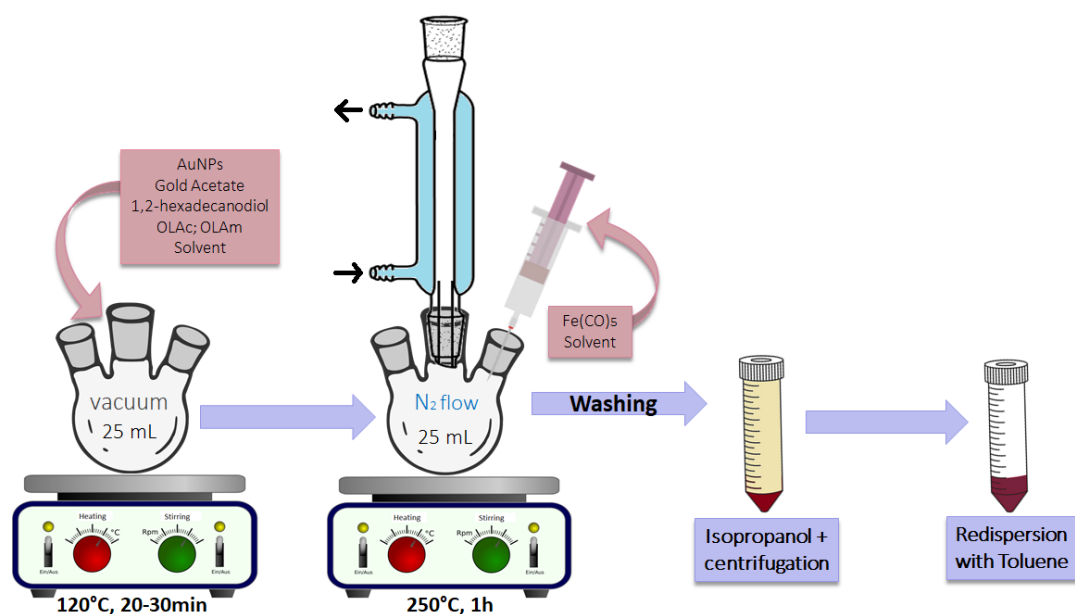


Figure 2.2: Au-AuFe Core-Shell NPs synthesis protocol.⁴⁶

In this master thesis, the protocol schematized on Figure 2.2 was optimized by adjusting some parameters, such as the use of $\text{Au}(\text{COOCH}_3)_3$ and the ratio of AuNPs seeds in relation to $\text{Fe}(\text{CO})_5$ and $\text{Au}(\text{COOCH}_3)_3$, with the purpose of studying their effect on the size and shape of the Au-AuFe core-shell nanohybrids. This protocol was also implemented using two different solvents with different polarities, octadecene and dioctyl ether, in order to test their influence on the final hybrid NPs obtained. The synthesis parameters are resumed on tables 3.2 and 3.3, and its respective results are discussed on Section 3.2.

On every synthesis performed in this Master thesis, small amounts of sample at different reaction times were characterized in order to study the reaction progress.

3

Results and Discussion

Contents

3.1 AuNPs Seeds	28
3.2 Au-AuFe Core-Shell Nanoparticles Synthesis	32

3.1 AuNPs Seeds

In this section, the results of the optimization of the AuNPs synthesis protocol will be discussed.

3.1.1 Protocol Selection

3.1.1.A First Protocol

For the synthesis of the AuNPs seeds, a protocol using gold acetate as gold precursor and 1,2-hexadecanediol as its reducing agent, OLAm and OLAc as surfactants, and octadecene as solvent was used following a reported procedure.⁵⁰ All the materials were firstly heated up to 105°C for 30 minutes under vacuum and then the temperature was increased up to 180°C for one hour under an atmosphere of Argon. The samples were then washed with acetone and centrifuged at 4500 RPM for 15 minutes (Figure 3.1).

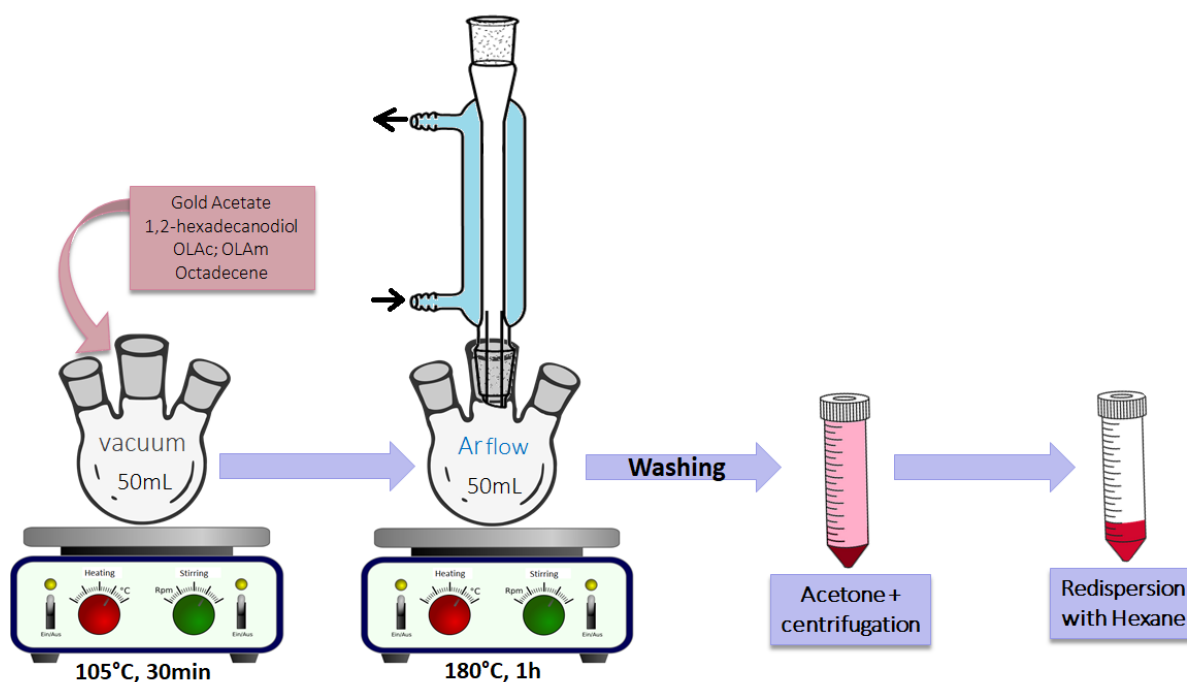


Figure 3.1: First AuNPs seeds synthesis protocol.

This protocol was optimized changing the amount of one of the reagents, in order to study their effect aiming at attaining monodisperse AuNPs. As represented on table A.1, after a first try on this protocol (SS01), the 1,2-hexadecanediol was decreased on a second trial (SS02), the OLAc was decreased on a third trial of the protocol (SS03) and finally, the 1,2-hexadecanediol was increased in relation to the third synthesis on a fourth trial (SS04). After each one of these synthesis, two characterization techniques were implemented, TEM to determine the size and shape of the AuNPs and UV-visible spectroscopy to

study their optical properties. These characterization results of both TEM and UV-visible spectroscopy are disposed on Figures A.1 to A.4.

The TEM results obtained reveal that all the AuNPs synthesized present high monodispersity, and the size increases when the quantity of 1,2-hexadecanediol is decreased and vice-versa, however the variation observed is just around a nanometer. Since the role of the 1,2-hexadecanediol is to serve as reducing agent of the gold precursor added, it was expected that an increase in the amount of 1,2-hexadecanediol would lead to a faster reduction of gold precursor, resulting on smaller nanoparticles due to its adsorption and stabilizing effect.^{51,52}

The effect of OLAc in the AuNPs synthesis was also studied by decreasing its quantity from synthesis SS01 to SS03 (table A.1). It was to expect that the decreasing of OLAc on the reaction mixture would provoke a decreasing of the nucleation temperature and consequently the growth process can be tuned,⁵³ however the results obtained for the shape, size and monodispersity of the final NPs demonstrate a lot of similarities, thus analysing these results, the effect of OLAc studied in these synthesis ended up being inconclusive.

UV-visible spectroscopy allows the understanding of size, shape, surface structure and agglomeration state of the NPs studied. In particular, and as stated on chapter 1, AuNPs exhibit a distinct optical feature (LSPR), meaning the collective oscillation of electrons in the conduction band of AuNPs in resonance with a specific wavelength of incident light, and the LSPR of AuNPs creates an absorption peak in the visible region (500 nm-600 nm) of its UV-visible spectrum. In fact, there is a lot of bibliography concerning this matter dictating that spherical AuNPs have SPR on the range from 520nm to 580nm on UV-visible spectra,⁵⁴ and according to the spectra represented on Figures A.1 to A.4, the results were as expected since the SPR is visible as a peak observed in the range from 527 nm to 539 nm.

Observing its UV-visible spectra, the peak absorbance wavelength increases with particle diameter,⁵⁵ which is not visible in the results obtained since the diameter of particles synthesized are very similar and this absorption peak can be shifted by various factors, namely the shape and aggregation state of the NPs. Actually, it is possible to observe on the UV-visible spectra of Figures A.1 to A.4, that at higher wavelengths, the absorbance is not as close to zero as it should be, suggesting the presence of aggregates on the sample, consequently translating into low colloidal stability.⁵⁵

3.1.1.B Second Protocol

Since the UV-visible spectra of the samples obtained by the first protocol suggested the existence of aggregates, the protocol was adapted to the one explain in detail on section 2.3.1.⁴⁹ The main difference on both protocols is the gold precursor used, that changed from gold acetate to gold chloride trihydrate, and the reaction temperature that is higher on the second protocol used.

Similarly to the first protocol, this second protocol was also tested: a first try (SS09) that was per-

formed as described by Figure 2.1, a second try (SS10) that was a repetition of SS09, with the difference that the isopropanol was added to the reaction mixture sooner in order to stop the reaction faster, and a third try (SS11) in which the reaction was kept at 110 °C for two hours, instead of 150 °C for half an hour (Figure 2.1).

The samples were also characterized by UV-visible spectroscopy and TEM (Figures A.5 to A.7). Comparing to the results obtained by the first method, the AuNPs obtained by the second protocol resulted on slightly higher-sized monodisperse nanoparticles. Importantly, it was possible to obtain UV-visible spectra that demonstrate high colloidal stability since at higher wavelengths the absorbance is practically zero. The comparison (UV-visible spectrum and respective TEM images) between the two protocols (samples SS03 and SS09) is represented in Figure 3.2.

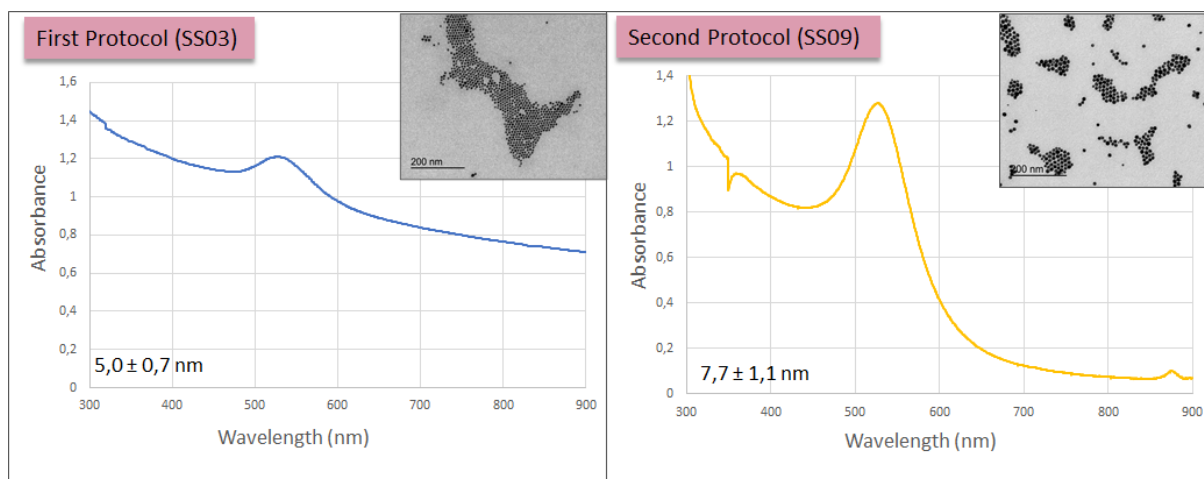


Figure 3.2: Comparison (UV-visible spectrum and respective TEM images) between the two protocols (samples SS03 and SS09) used to synthesize AuNPs.

With the testing of the protocol, it was possible to observe that a decreasing of temperature leads to slightly lower monodispersity and that an increasing of the reaction time would lead to generally higher-sized NPs with lower dispersion (as represented on Figures A.5 to A.7). However, this change observed was not very significant when increasing the reaction time from half an hour to two hours, so the protocol chosen for the following AuNPs synthesis was the one described on Figure 2.1 (30 minutes of reaction). The isopropanol was added to the reaction mixture as soon as possible in order to quench the reaction faster and thus prevent the Ostwald ripening,⁵⁶ in which the smaller NPs in solution would dissolve and deposit on larger NPs in order to achieve thermodynamic stability, hence leading to polydispersity rather than monodispersity.

3.1.2 Calculation of Gold Concentration

In order to use the AuNPs (Section 3.1) as seeds to grow an AuFe shell, it is useful to have an approximation of its gold concentration as a parameter to further calculate the amount of reagents used on the Au-AuFe core-shell nanoparticles synthesis (Section 3.2). This molar concentration would be merely an approximation since the AuNPs are not totally monodisperse.

Inductively Coupled Plasma Mass Spectrometry (ICP-MS) is a technique widely used to determine metal elements. Nonetheless, this technique is highly time-consuming both for the preparation of the sample as well as for the waiting time of the results (a total of, minimum, 2 weeks).

There is an alternative, and widely implemented⁵⁷ way to obtain the gold concentration of AuNPs, which is from the UV-visible spectrum. From the Lambert Beer's law⁵⁸ represented by eq. (3.1), in which A is the absorbance, ϵ the molar absorption coefficient ($M^{-1}cm^{-1}$), c the concentration in molar (M) and l the optical path in cm, it is viable to consider a linear correlation between the absorbance obtained with UV-visible spectroscopy and the concentration of gold in the AuNPs. Particularly, in the case of gold, there is the advantage that its molar absorption coefficient at 400 nm has been precisely estimated and it is constant ($2400 M^{-1}cm^{-1}$) regardless of the shape and size of the NPs.⁵⁷

$$A = \epsilon cl \quad (3.1)$$

Hence, using eq. (3.1) and knowing that the optical path (i.e. cell width) is 1 cm and a ϵ_{400} of $2400 M^{-1}cm^{-1}$, the gold concentration can be subtracted. Furthermore, in order to obtain a more accurate value of concentration some dilutions were made in each synthesis and the final Au concentration was estimated as the average of the concentrations of the different dilutions.

To evaluate the accuracy of this method, ICP-MS was also performed on some samples. The concentration obtained with both UV-visible spectroscopy and ICP-MS were compared and summarized on table 3.1.

Table 3.1: Concentration of AuNPs: comparison of results between ICP and UV-Vis spectroscopy.

Synthesis	ICP (M)	UV-vis (M)	%Error
SS09	$6,3 \times 10^{-3}$	$6,2 \times 10^{-3}$	2,6
SS10	$1,7 \times 10^{-2}$	$1,6 \times 10^{-2}$	1,1
SS11	$1,8 \times 10^{-2}$	$9,7 \times 10^{-3}$	45

From table 3.1, both synthesis SS09 and SS10 present low percentage of error from ICP-MS to UV-vis. On the other hand, sample SS11 present a high percentage of error, which can be associated with the preparation of this sample for ICP-MS measurements, since this sample got substantially evaporated overnight during the preparation process. Stated this, it is possible to conclude that the calculation of gold concentration from UV-visible spectrum is an accurate method, and it was performed on every following AuNPs synthesis as it is a faster, easier and cheaper method comparing to ICP-MS.

3.2 Au-AuFe Core-Shell Nanoparticles Synthesis

After synthesizing the AuNPs seeds as described in Section 3.1, the following step was attempting the growth of an AuFe shell on the preformed AuNPs seeds.

3.2.1 First Protocol

Initially, the protocol used was a first adaption of the one reported by Chiang et al. where FeAu NPs of different compositions were obtained.⁴⁶ In our case, the major difference from the latter is that we included the preformed AuNPs within the reaction system aiming at obtaining Au-AuFe core-shell NPs. In this first protocol (represented on Figure 3.3), gold acetate along with its reducing agent, 1,2-hexadecanediol, the surfactants (OLAc and OLAm) and the solvent used (octadecene) were kept under vacuum, for 10 to 15 minutes. Afterwards, the atmosphere was changed to nitrogen and the iron precursor ($\text{Fe}(\text{CO})_5$) was injected. Forty minutes after, the AuNPs synthesized by the protocol described on Figure 2.1 were injected, the environment was changed to vacuum and the temperature increased until 120 °C for about half an hour in order to evaporate the solvent (hexane) where the AuNPs were dispersed. Afterwards, the environment was changed to nitrogen and the reaction was kept at 250 °C for one hour. The molar ratio of gold and iron precursors versus the Au of the preformed AuNPs (AuNPs: Au:Fe) was of 1:2:2.

The samples were then washed with isopropanol and centrifuged for 8 minutes at 6000 RPM.

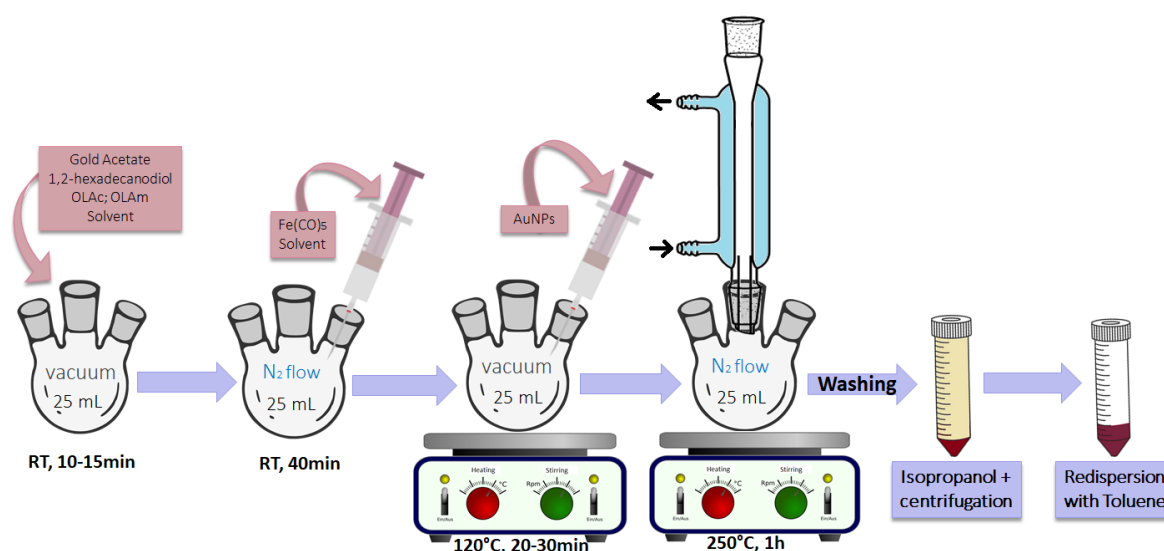


Figure 3.3: First Au-AuFe core-shell NPs synthesis protocol.⁴⁶

The results of this first protocol are represented on Figure 3.4: both UV-visible spectra and TEM images show an appearance of aggregates on the final NPs in comparison to the AuNPs that were used as seeds.

UV-visible spectrum demonstrate that the final NPs present two broad peaks that may suggest the existence of different sizes and shapes, which was further confirmed by the TEM images. Furthermore, the UV-Vis spectrum does not reach values near zero at longer wavelengths, inferring the presence of aggregates.

The histograms that represents the NPs size distribution of both the sample SS20 and the respective AuNPs used as seeds (SS19) are displayed in Figure B.1.

Observing these characterization results, and in order to prevent the formation of aggregates, thus improving colloidal stability, the protocol of Figure 3.3 was re-evaluated and changed to the protocol described by Figure 2.2.

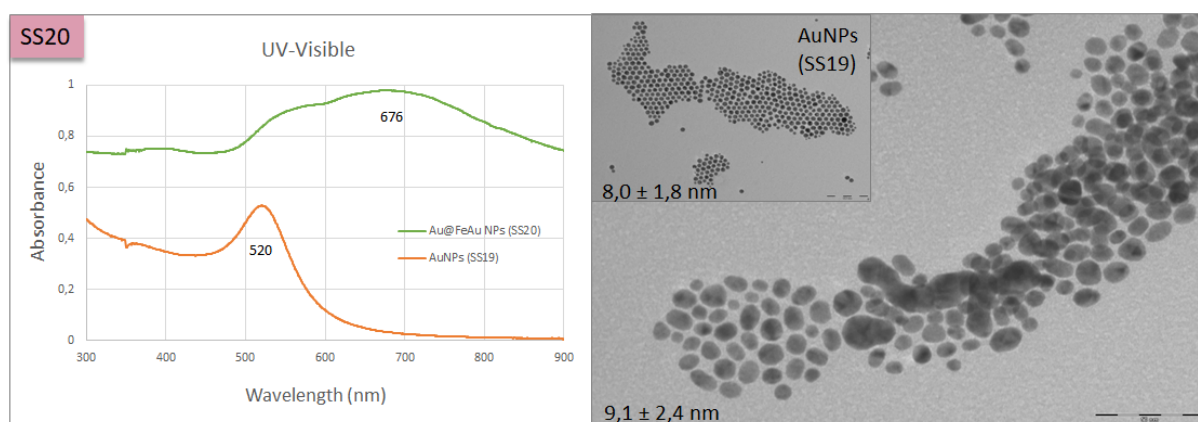


Figure 3.4: Characterization results of synthesis SS20 and respective AuNPs seeds (SS19): UV-visible spectra and TEM images with 200kX of magnification.

HRTEM analysis was performed in order to determine whether the NPs present more than one type of material. The images obtained were analyzed with Digital Microsoft software and some of these images are represented on Figure 3.5 with the respective analysis of crystalline plans. The analysis reveals only the presence of Au.

Since $\text{Fe}(\text{CO})_5$ was also added to the reaction mixture, an EDX analysis was performed to determine the presence or not of Fe within the NPs. The images analyzed and the respective Au and Fe percentages obtained on different parts of the sample are represented on Figure 3.6.

The EDX results obtained demonstrate a percentage of about 1% of Fe in different regions of the TEM grid (one nanoparticle isolated, a group of NPs and a group of aggregates). Another group of aggregates in a grayer colour was also analyzed and a higher percentage of Fe was obtained (about 25% of Fe to 75% of Au). This grey material could be a Fe-based material arisen, probably, from the deterioration of the $\text{Fe}(\text{CO})_5$ during an inappropriate manipulation of the vacuum process of the reaction. Nevertheless, on the nanoparticle isolated that was analyzed (Figure 3.6), Fe_3O_4 domains are not visible, which can signify the presence of metallic Fe in the form of AuFe alloy, as metallic Fe is unstable at air conditions and would immediately get oxidized to an Fe-based oxide.

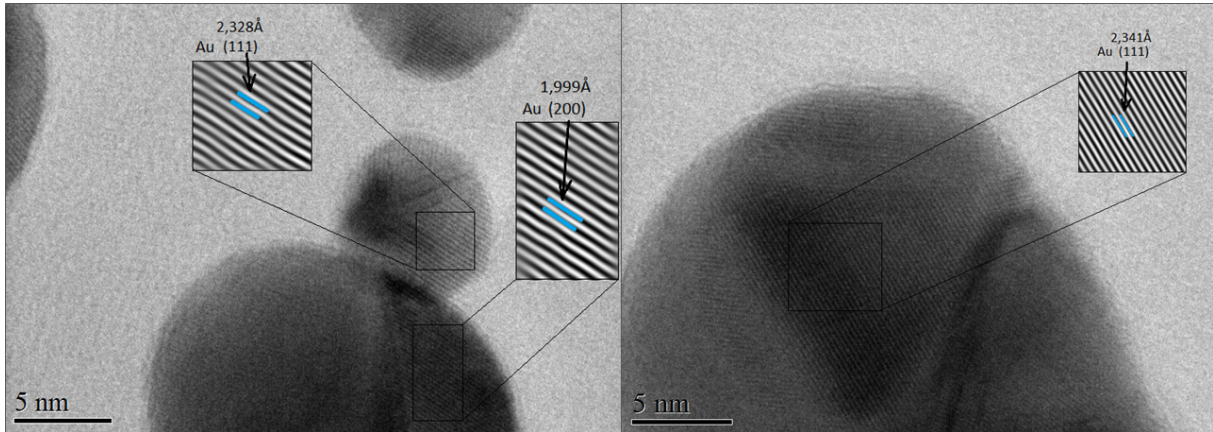


Figure 3.5: HRTEM images of sample SS20 and respective crystalline plan analysis with Digital Microsoft.

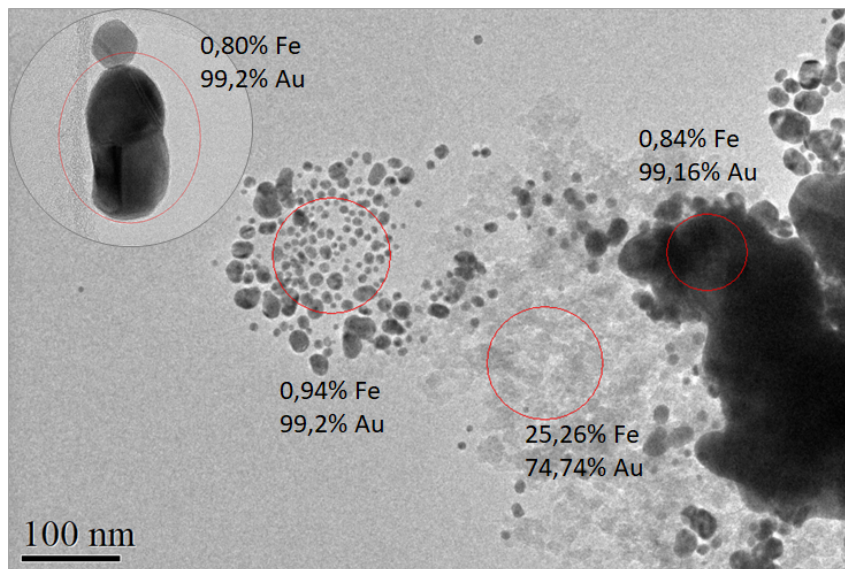


Figure 3.6: TEM-EDX results of sample SS20.

This way, XPS was performed to determine whether the sample presents metallic Fe or not. The high resolution XPS spectrum for the energy range corresponding to Fe 2p obtained is represented on Figure 3.7.

A general XPS measurement of its surface was also performed and it is described on Figure B.11.

Analysing Figure 3.7, apart from the noise observed, no peaks are visible in the spectrum of Fe 2p, meaning that it is undetectable by the XPS analysis performed.

Thus, it is possible to conclude that the sample SS20 does not present a detectable quantity of AuFe alloy, and the protocol performed to obtain this sample (the one described by Figure 3.3) seems not appropriate to obtain AuFe alloys. Hence, it was a good call to dismiss this protocol.

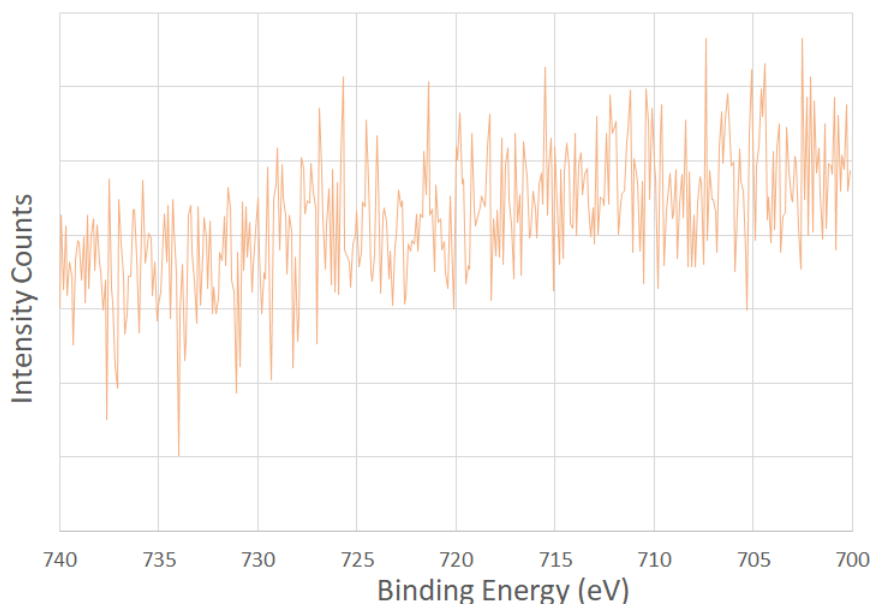


Figure 3.7: High resolution XPS spectrum of energy ranges corresponding to Fe 2p of sample SS20.

3.2.2 Second Protocol

The first protocol (Figure 3.3) presented some drawbacks, probably in the handling of the iron pentacarbonyl. By injecting the $\text{Fe}(\text{CO})_5$ before the hexane evaporation process through vacuum, we suspected that a deterioration of $\text{Fe}(\text{CO})_5$ could occur, thus limiting its reactivity.

Hence, the protocol was changed with the intention of not having $\text{Fe}(\text{CO})_5$ in the reaction mixture whilst in vacuum conditions. Consequently, it was injected after the evaporation of the hexane where the AuNPs seeds were dispersed, leading to the protocol described in Figure 2.2.

This second protocol was also tested in different synthesis conditions, namely the molar ratio of AuNPs seeds versus $\text{Au}(\text{COOCH}_3)_3$ and $\text{Fe}(\text{CO})_5$, and the usage of two distinct solvents, octadecene and dioctyl ether.

3.2.2.A Synthesis with $\text{Au}(\text{COOCH}_3)_3$

Primarily, the protocol was tested with a molar ratio of AuNPs seeds in relation to $\text{Au}(\text{COOCH}_3)_3$ and $\text{Fe}(\text{CO})_5$ of 1:1:1, both using octadecene and dioctyl ether, leading to samples SS21 and SS22, respectively. Subsequently, the amount of precursors used was increased to the double of AuNPs, translating into a ratio of 1:2:2, and it was also tested using octadecene and dioctyl ether as solvents, leading to samples SS30 and SS33, respectively.

On table 3.2, the conditions of each synthesis and respective TEM observations are summarized.

Table 3.2: Au-AuFe nanoparticles synthesis with gold precursor. The number of magnets beside each sample represents, qualitatively, the magnitude of the magnetic susceptibility of the sample.

Sample	AuNPs: Au:Fe Ratio	Solvent	Synthesis Parameters		TEM observations
			Temperature	Time	
SS21	1:1:1	Octadecene	250°C	1h	3,4 ± 1,0 nm 7,1 ± 1,3 nm 10 ± 1,1 nm presence of dimers
SS30	1:2:2				4,7 ± 2,3 nm 9,8 ± 1,3 nm presence of dimers
SS22	1:1:1	Diethyl ether	250°C	1h	4,4 ± 1,5 nm 10 ± 3,8 nm a lot of aggregates; mostly small nanoparticles
SS33	1:2:2				3,6 ± 1,3 nm 10 ± 1,3 nm



Characterization Results:

A – SS21 TEM images of SS21 (Figure 3.8) present a few dimers and show three different sizes of nanoparticles. Additionally, comparing to the size of the initial AuNPs, there is the formation of lower-sized NPs, indicating that new NPs have been formed, beyond the possible formation of Au-AuFe core-shell nanoparticles. Its UV-visible spectrum is also represented on Figure 3.8 along with the spectrum of AuNPs used as seeds. It is noticeable that at high wavelengths the absorbance in both spectra is null, suggesting good colloidal stability and probably the absence of aggregates. Furthermore, there is a red-shift of 17,5 nm of the LSPR peak of the initial AuNPs, implying its surface modification.

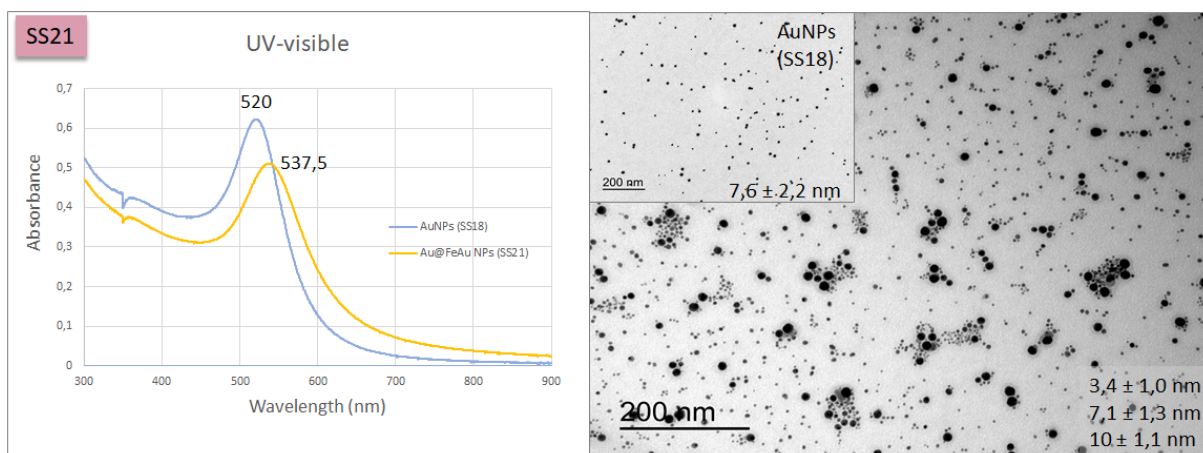


Figure 3.8: Characterization results of synthesis SS21 and respective AuNPs seeds (SS18): UV-visible spectra and TEM images with 200kX and 150kX of magnification, respectively.

Since TEM images demonstrate the existence of three different sizes of NPs, it is important to analyse the composition of each group size of nanoparticles, in order to have a better understanding of its composition and the evolution of the reaction.

Hence, HRTEM was performed and the results are represented on Figure 3.9, along with an analysis of its crystalline plans by Digital Microsoft.

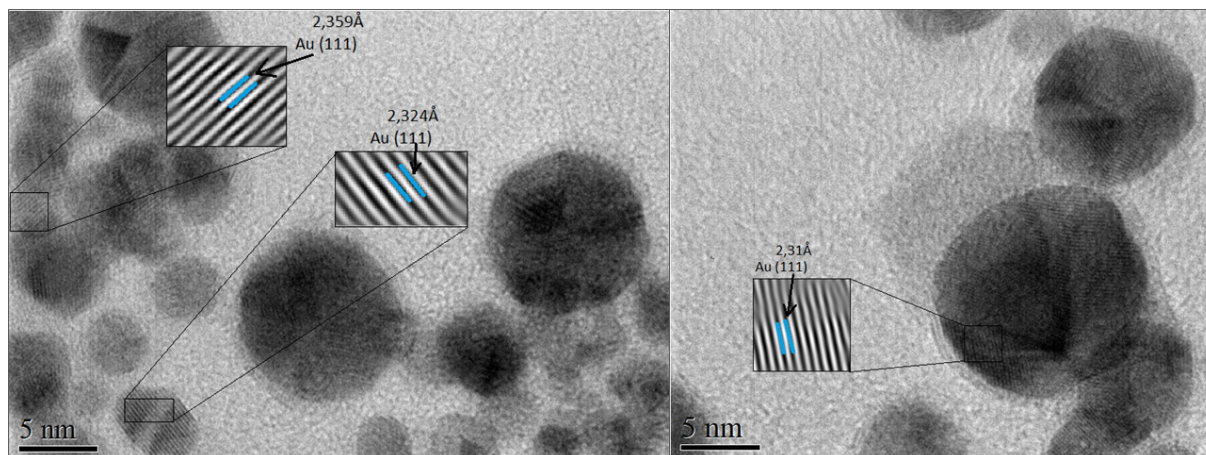


Figure 3.9: HRTEM images of sample SS21 and respective crystalline plan analysis with Digital Microsoft.

The crystalline plan analysis revealed only the presence of Au in the NPs formed, however it is visible in the HRTEM images the presence of lighter domains that may suggest the existence of Fe_3O_4 in the sample, which is concordant to the fact that the sample has magnetic response to a magnet.

Thus, an EDX analysis was carried out to find out the percentage of both Fe and Au presented on the sample. The results are represented on Figure 3.10.

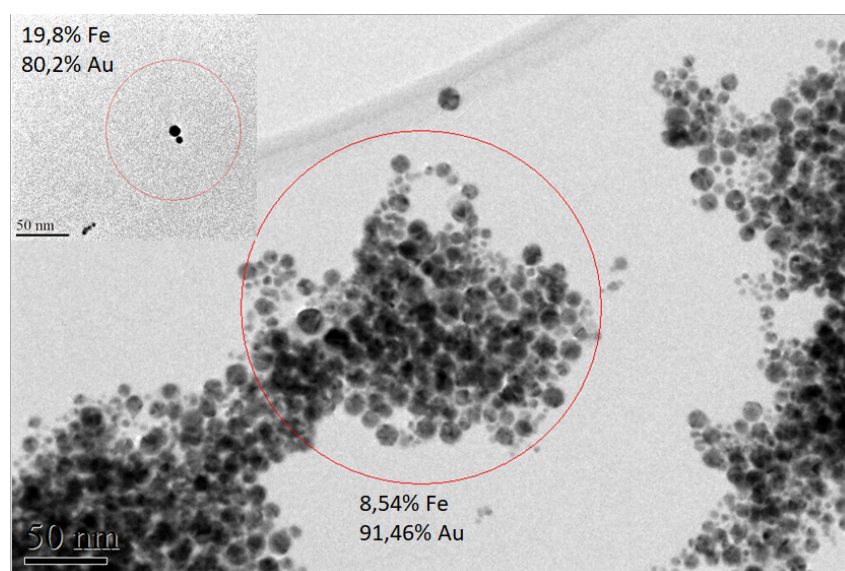


Figure 3.10: TEM-EDX results of sample SS21.

As demonstrated by Figure 3.10, the EDX analysis was carried out both in regions where a group of NPs is visible and in regions where only a couple of NPs are visible. An Fe percentage of about 9% and 20% was obtained, respectively. It should be pointed out that the values obtained when analyzing a

group of NPs is a more realistic approach than the one obtained when only a few NPs are considered, since it is a global measurement and the risk of contamination is lower.

Some small grayed domains were observed, although an analysis by HRTEM was not possible. Hence the Fe percentage determined by EDX could be due to the formation of Fe_3O_4 rather than metallic Fe. Therefore, an analysis of XPS was taken place to determine the oxidation state of the existing Fe, and the results for the high resolution XPS spectrum of Fe 2p of sample SS21 is showed on Figure 3.11.

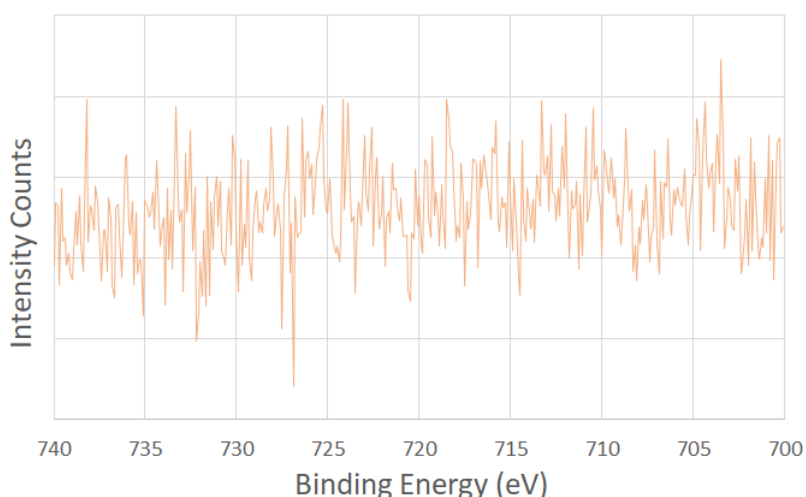


Figure 3.11: High resolution XPS spectrum of energy ranges corresponding to Fe 2p of sample SS21.

Likewise for sample SS20, there are no visible peaks on the XPS spectrum of Fe 2p of sample SS21, which is not in agreement neither to the EDX analysis, that shows a considerable Fe percentage, nor to the fact that the sample has a high response to the magnet. In order to make sure that the XPS data obtained was in fact correspondent to the sample studied, this measurement was repeated and the results obtained for the general surface's measurements (Figure B.13) indicate, once again, the absence of Fe, since no peak is visible around 700 eV of binding energy. Subsequently, XRD analysis was also performed, aiming to examine crystalline phases present within the sample.

The XRD spectrum obtained for sample SS21 together with the reported crystallographic plans list for the Au and Fe_3O_4 phases (0011140 and 00-019-0629, respectively), along with the respective peak analysis is represented on Figure 3.12. The peaks observed seem to correspond only to Au, thus suggesting the absence of any Fe-based phase and thus confirming the results obtained by XPS (Figure 3.11).

The absence of Fe inferred by both XPS and XRD analysis is not concordant to the high magnetic susceptibility presented by this sample (as referenced on table 3.2). A repetition of the synthesis of this sample should be performed, in order to discard any sample confusion during the sample's labeling process.

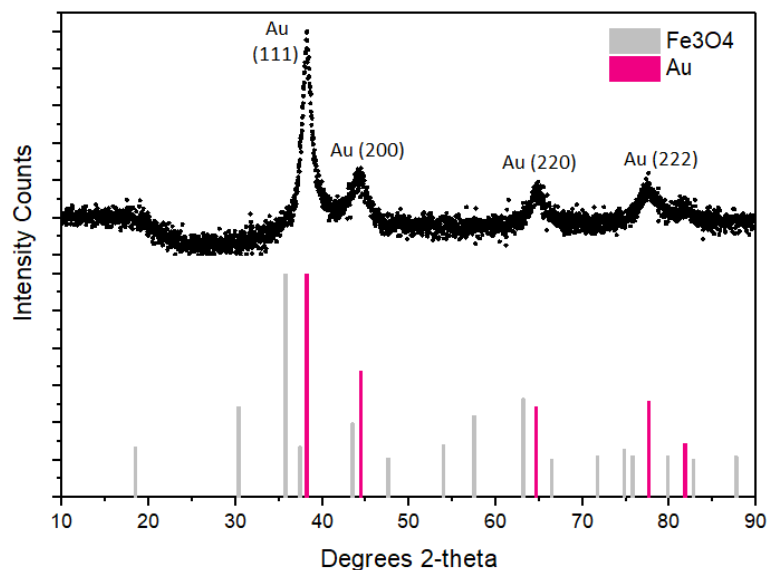


Figure 3.12: XRD results of sample SS21 together with the Au (0011140)⁴⁷ and Fe₃O₄ (00-019-0629)⁴⁸ peaks.

B – SS22 Concerning the synthesis of SS22, both TEM images and UV-visible spectrum (Figure 3.13) indicate the presence of aggregates. The UV-visible spectrum presents a LSPR red-shift of 28,5 nm from the initial AuNPs seeds. On TEM images, it is visible that there are two sizes of NPs, being the lower-sized nanoparticles smaller than the original AuNPs seeds used, suggesting the formation of new smaller nanoparticles.

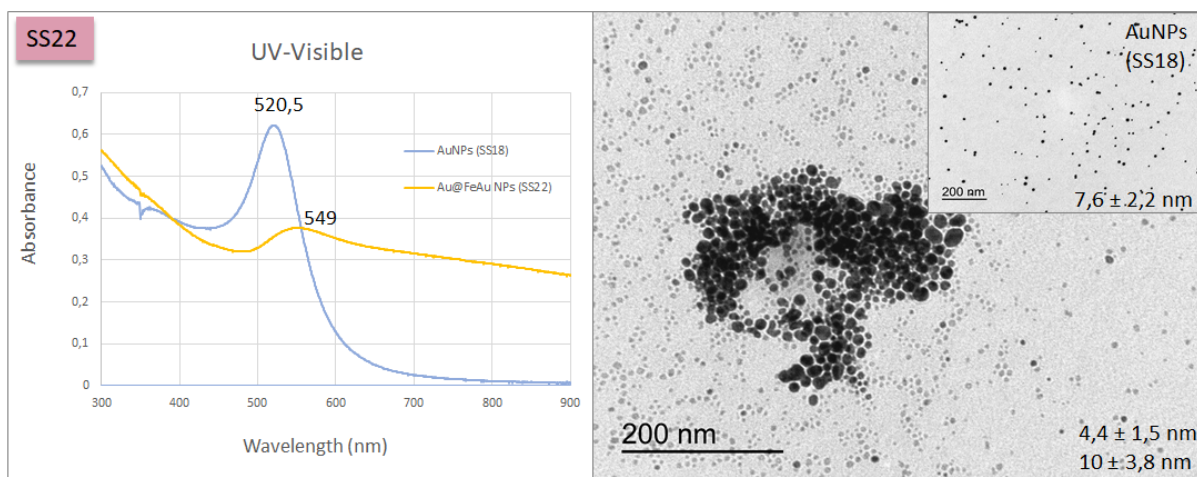


Figure 3.13: Characterization results of synthesis SS22 and respective AuNPs seeds (SS18): UV-visible spectra and TEM images with 250kX and 150kX of magnification, respectively.

Due to the great amount of aggregates observed indicating low colloidal stability, no further characterization techniques were carried out on this sample throughout this work.

C – SS30 The UV-visible spectrum of SS30 (represented on Figure 3.14) compared to the spectrum of the respective AuNPs seeds shows a red-shift of 58,5 nm on the LSPR peak of the initial AuNPs. TEM images show the presence of dimers along with two different sizes of nanoparticles, suggesting the possibility of the presence of either a Au-AuFe core-shell NPs or an overgrowth onto the AuNPs initial seeds, but also of newly formed Au or AuFe hybrid NPs.

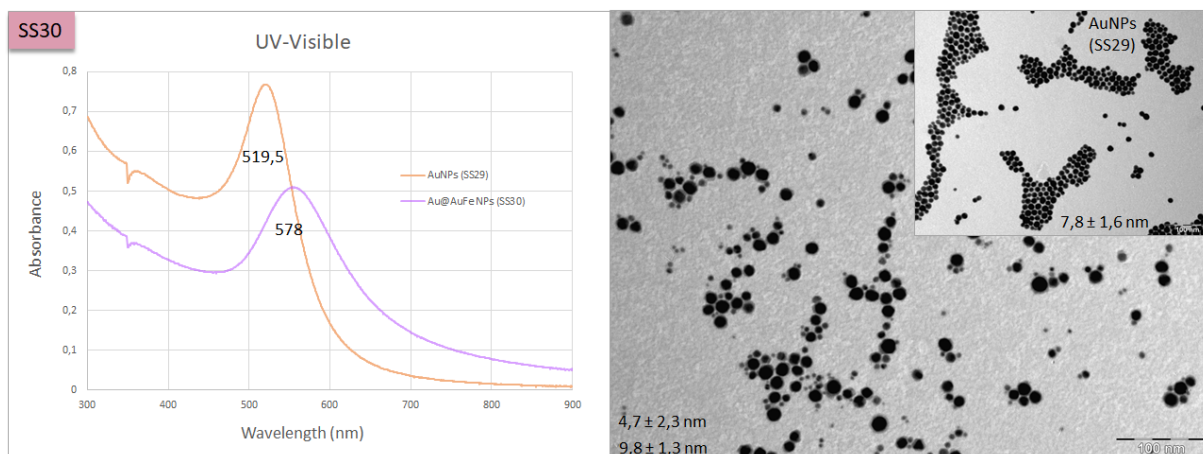


Figure 3.14: Characterization results of synthesis SS30 and respective AuNPs seeds (SS29): UV-visible spectra and TEM images with 200kX of magnification.

In order to acquire more detailed information about the existence of the AuFe alloy on either the smaller and larger NPs, HRTEM images were obtained (Figure 3.15).

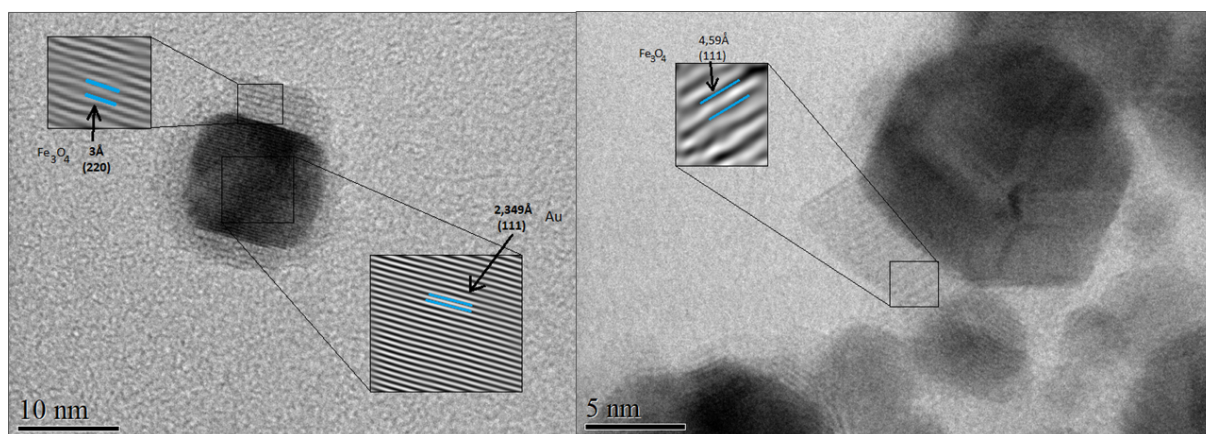


Figure 3.15: HRTEM images of sample SS30 and respective crystalline plan analysis with Digital Microsoft.

The analysis of the crystalline plans by HRTEM illustrates the existence of AuNPs with either a shell or dimers of Fe_3O_4 . In addition, EDX analysis was carried out on the HRTEM images obtained, and the results (Figure 3.16) demonstrate an Fe percentage of about, roughly, 10%, that is concordant when analyzing either a major group of NPs or just a few NPs. This quantity of Fe can probably be attributed to the Fe_3O_4 shell observed on Figure 3.15, although a shell of AuFe alloy at the interface between the

Fe_3O_4 shell and the AuNPs surface cannot be ruled out as having a small content of metallic Fe inserted into the crystalline structure of Au would not strongly affect Au cell parameters.

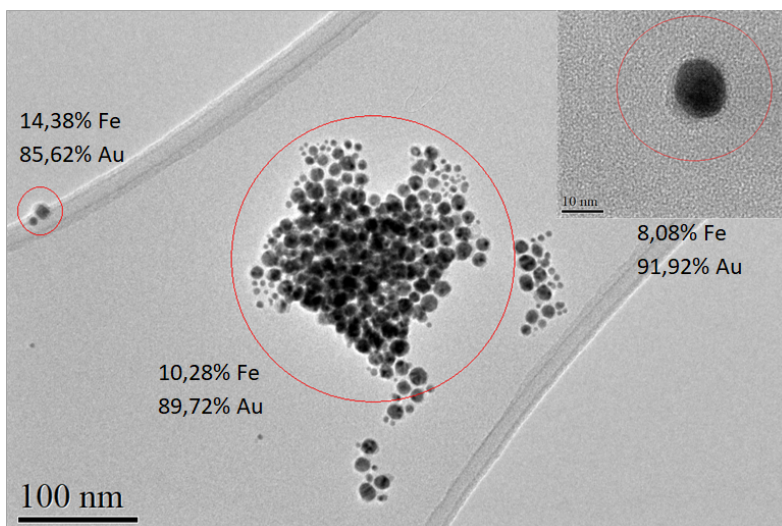


Figure 3.16: TEM-EDX results of sample SS30.

To evaluate the degree of oxidation of the existent Fe content, an XPS analysis was taken place, and the high resolution XPS spectrum of Fe 2p of sample SS30 is represented on Figure 3.17.

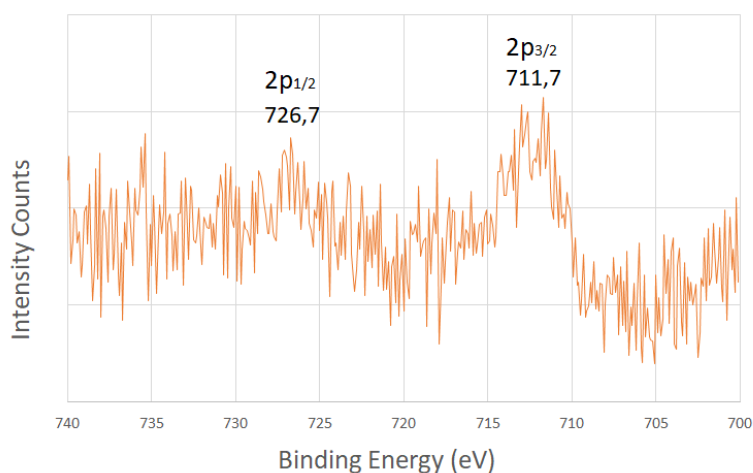


Figure 3.17: High resolution XPS spectrum of energy ranges corresponding to Fe 2p of sample SS30.

Contrarily to the XPS results obtained for the previous samples, on sample SS30 two peaks are observable on the Fe spectrum: one roughly centered at 711,7 eV and the other at 726,7 eV of binding energy, being the first one the most accentuated peak. Consulting the bibliography on the binding energies for each material, as described on table B.1,⁵⁹ the first peak observed fits into the published information for the Fe 2p_{3/2} and the second one represents the 2p_{1/2} for the ion Fe³⁺, which are symmetric

peaks and thus represent the existence of Fe_3O_4 on this sample.

Although the high width observed on the first peak can be translated into a mixture of more than one oxidized state, in which metallic iron can be included, it is very difficult to claim the existence of an AuFe alloy given this data.

D – SS33 Likewise for the samples mentioned above, UV-visible spectrum and TEM images of sample SS33 demonstrate interesting results on colloidal stability, along with the formation of two different sizes of NPs, as demonstrated by Figure 3.18.

Moreover, its UV-visible spectrum exhibits a red-shift of 24,5 nm from the original AuNPs, demonstrating a conformational change in relation to the initial NPs, and according to its TEM images, in which two different NPs sizes are visible, one of them has a smaller size comparing to the original AuNPs, thus again inferring the formation of newly formed NPs.

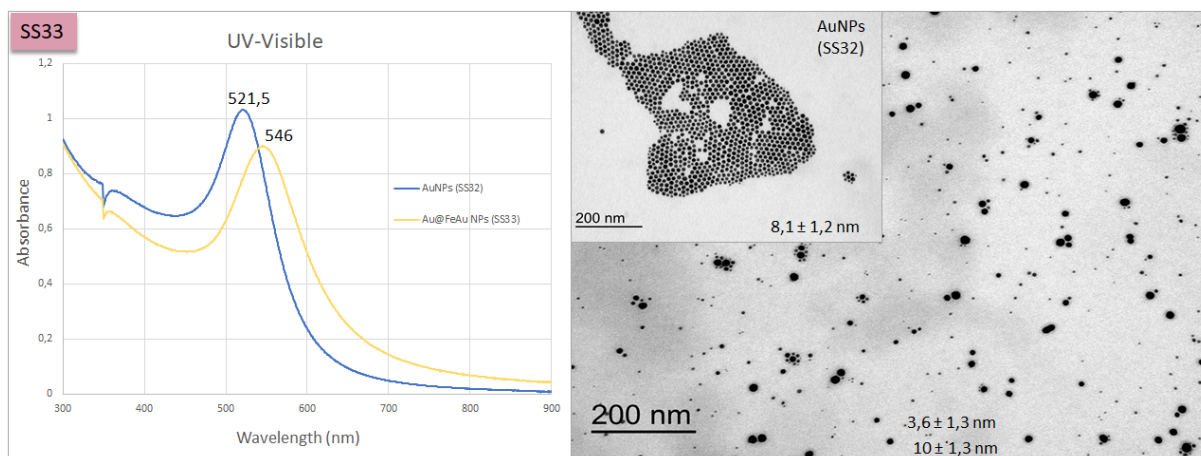


Figure 3.18: Characterization results of synthesis SS33 and respective AuNPs seeds (SS32): UV-visible spectra and TEM images with 150kX and 200kX of magnification, respectively.

This way, this sample was also submitted to HRTEM to have a better understanding of its composition, as represented on Figure 3.19, and the crystalline plans found were analyzed with Digital Microsoft software.

The analysis of the crystalline plans suggested the presence of only Au, which can be a positive data towards our objective, since the absence of Fe_3O_4 domains can be a good indicative for the presence of an AuFe alloy, considering that upon the formation of an AuFe alloy, the iron contained within is protected from oxidation.

Since only the Au crystalline plans were detected, an EDX analysis was also performed in order to determine the Fe percentage contained in the characterized sample.

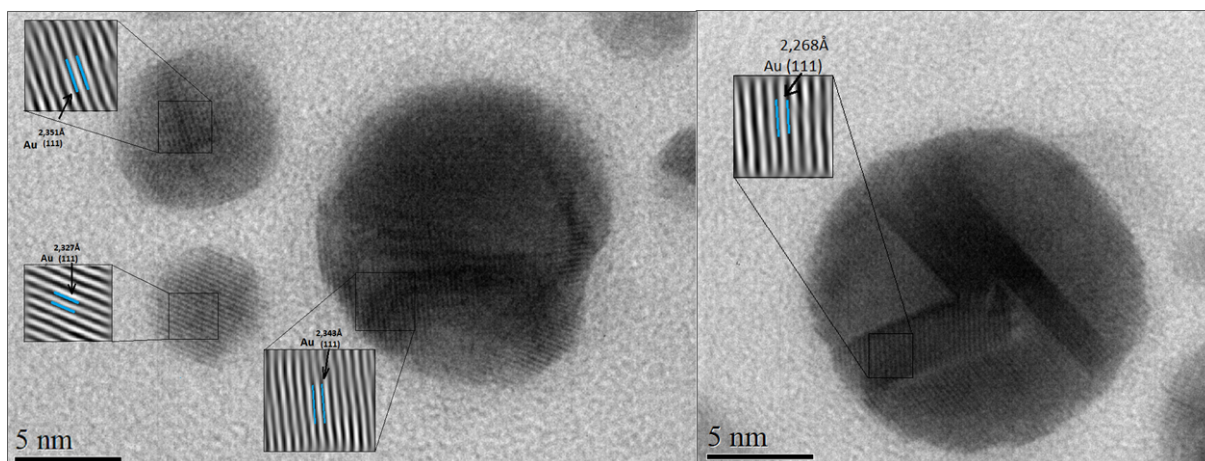


Figure 3.19: HRTEM images of sample SS33 and respective crystalline plan analysis with Digital Microsoft.

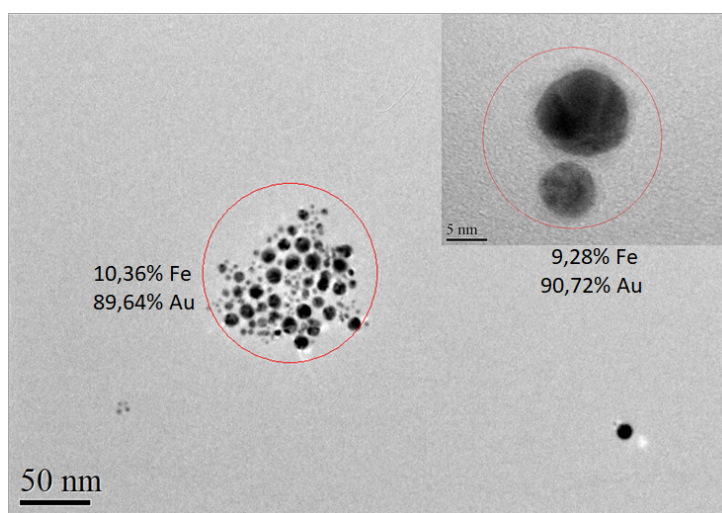


Figure 3.20: TEM-EDX results of sample SS33.

The EDX results expressed on Figure 3.20, consistently reveal an Fe percentage of about 10% to 90% of Au, which is concordant to the previous sample analyzed (SS30), since the only protocol difference between both samples is the solvent used.

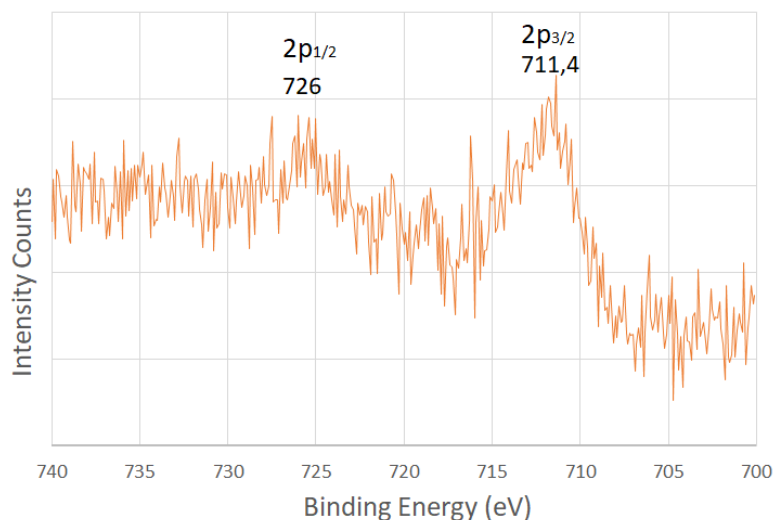


Figure 3.21: High resolution XPS spectrum of energy ranges corresponding to Fe 2p of sample SS33.

Contrarily to what was observed on HRTEM images for sample SS30, on sample SS33 no Fe_3O_4 domains were detected, and along with an Fe percentage of 10% detected with EDX, it is important to determine whether the sample contained metallic Fe or Fe_3O_4 . Hence, the sample was submitted to an XPS analysis.

The XPS results for the high resolution Fe 2p spectrum observable on Figure 3.21 reveal the existence of two peaks, likewise to the previous sample, one accentuated peak with a value of 711,4 eV and another one with 726 eV of binding energy, which are very similar values to the ones obtained on sample SS30, meaning that Fe_3O_4 seems to be predominant on this sample, being the first peak registered correspondent to Fe $2p_{3/2}$ and the second one to Fe $2p_{1/2}$.

Again, the Fe_3O_4 peak observed, as stated above, can present a wider form due to the existence of a mixture of different chemical states of iron, which does not exclude completely the possibility of having an AuFe alloy.

Exceptionally for this sample, the supernatant obtained upon washing had a darker color than the ones obtained for previous samples, which is translated into the existence of possibly smaller NPs that were unable to precipitate. It was decided to characterize this supernatant obtained as well in order to determine its composition.

D –.1 SS33-Supernatant The supernatant separated from the precipitate of sample SS33 was firstly characterized with UV-visible spectroscopy and TEM, comparing its results to the ones obtained for the initial AuNPs used, as demonstrated by Figure 3.22.

TEM images demonstrate that the NPs contained on the supernatant have a mean size of 3,3 nm, which is smaller than the size of the AuNPs used as seeds on this synthesis, meaning that these are NPs

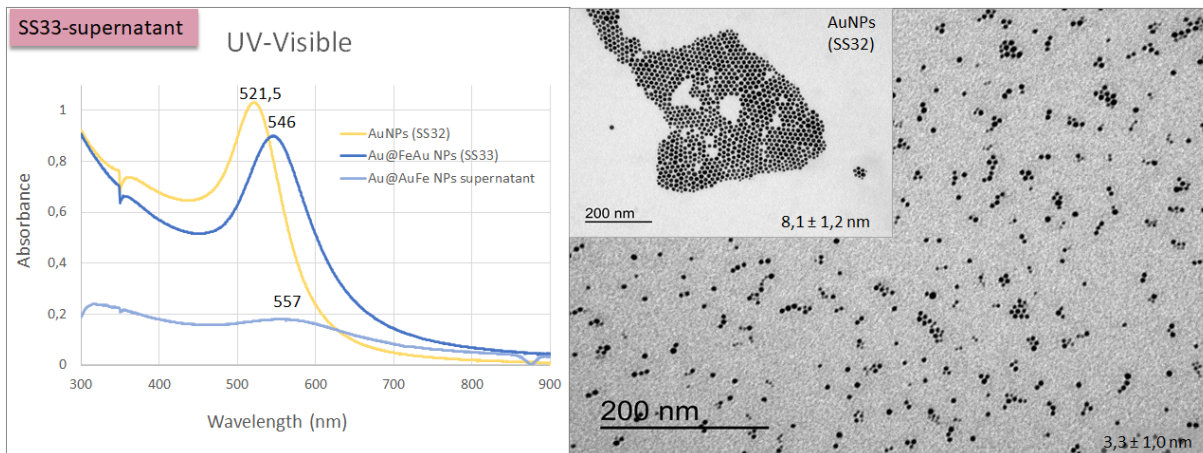


Figure 3.22: Characterization results of supernatant of synthesis SS33 and respective AuNPs seeds (SS32): UV-visible spectra and TEM images with 250kX and 200kX of magnification, respectively.

formed afterwards and have no relation to the AuNPs added into the reaction mixture. The histograms displaying the size distribution of each sample aforementioned together with the respective AuNPs seeds are depicted on Figures B.2 to B.5 and B.7.

This way, HRTEM was also performed in order to realize if these NPs contain Fe and/or Au. The HRTEM images and correspondent crystalline plan analysis is represented on Figure 3.23.

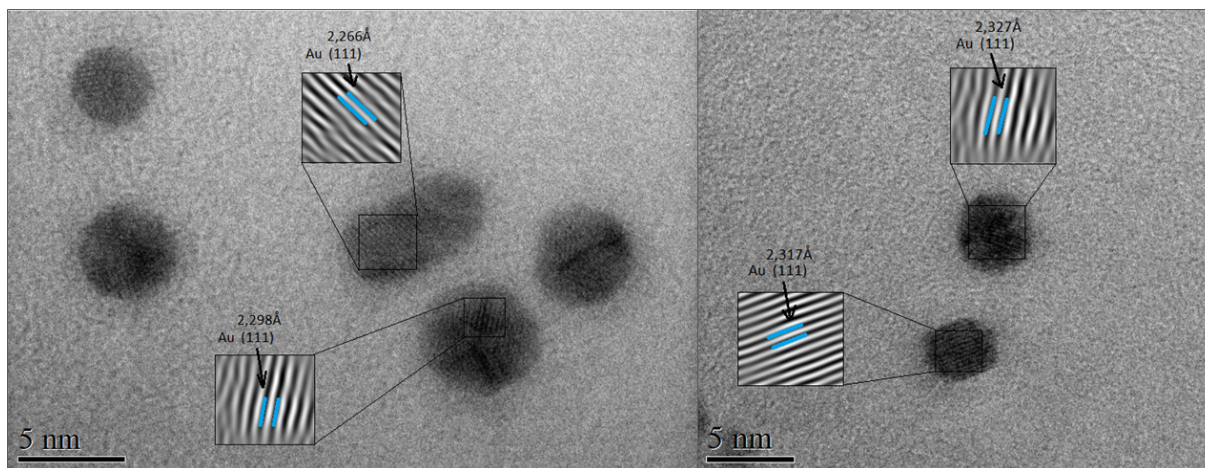


Figure 3.23: HRTEM images of the supernatant of sample SS33 and respective crystalline plan analysis with Digital Microsoft.

The analysis of the crystalline plans reveals the presence of peaks corresponding to only Au. Taking into account that no Iron Oxide Nanoparticles (IONPs) were detected on these HRTEM images, along with the fact that the supernatant solution hasn't showed magnetic response (which can also be due to its low concentration), most probably implies that these NPs are either only composed by Au or the AuFe alloy. Thus, an EDX analysis was also performed to make sure that the NPs formed are only composed by gold.

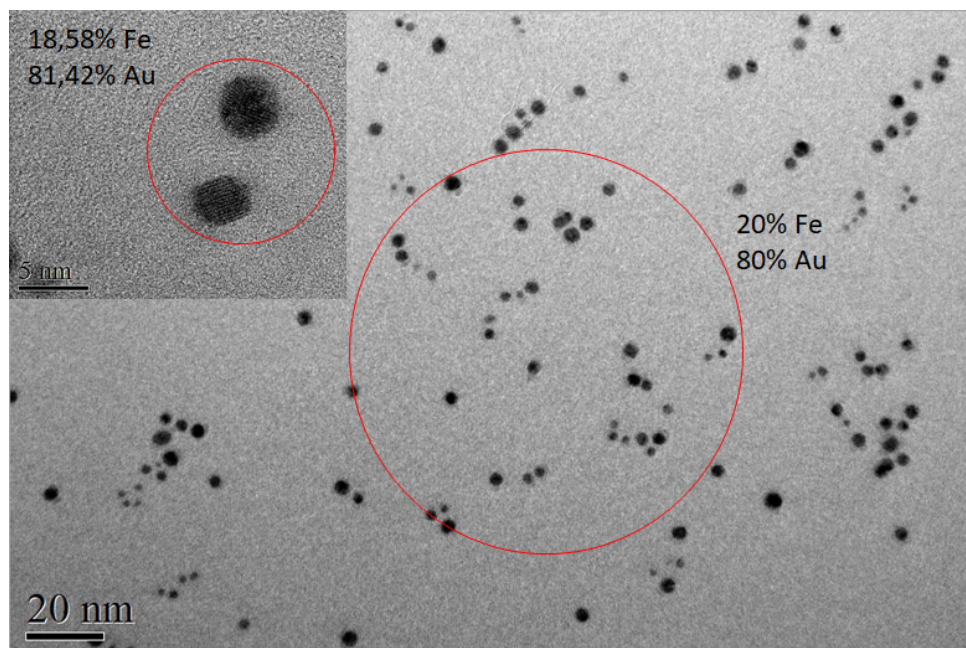


Figure 3.24: TEM-EDX results of supernatant of sample SS33.

Interestingly, the EDX results displayed on Figure 3.24 showed an amount of 20% of Fe in relation to 80% of Au, which is a considerable quantity of Fe and can be related to the existence of a AuFe alloy on these small NPs newly formed. Consequently, an XPS analysis was also performed to analyze its oxidized state.

The XPS analysis for the global surface's measurement (Figure B.16) suggest the presence of Fe, since a peak is visible around 700 eV of binding energy. Even though this peak is less visible than the ones observed on samples SS30 and SS33 (Figure B.14 and Figure B.15, respectively), it is possible to assume the presence of either metallic Fe or Fe_3O_4 in this sample.

The high resolution XPS for the Au 4f of samples SS20, SS21, SS30 and SS33 are described on Figures B.17 to B.20, and in all the samples it is possible to observe the presence of two peaks, Au 4f_{5/2} and Au 4f_{7/2}, since its binding energies coincide to the published values (table B.2).

Overall, the shapes obtained were nearly spherical, except for the sample SS22, in which the NPs formed suffered coalescence, thus forming irregular shaped particles and aggregates. Regarding the solvent, the use of octadecene seems to favor the formation of dimers and shells, although the usage of dioctyl ether seems to lead to rounder nanoparticles. The choice of doubling the amount of $\text{Au}(\text{COOCH}_3)_3$ and $\text{Fe}(\text{CO})_5$ in relation to AuNPs seeds derived from the idea that if there is excess of precursors in relation to AuNPs, it would facilitate the formation of an hybrid AuFe shell, which from the TEM images obtained it is not possible to confirm if it worked, since the images were taken by low resolution TEM and there is not a substantial growth observed from the samples SS21 and SS30, where the molar ratio of AuNPs: Au:Fe was 1:1:1, and the samples SS22 and SS33 in which the same molar

ratio was 1:2:2.





On table 3.2, the magnets beside each sample represent the experiment that was performed after each synthesis in which a powerful magnet was used to test whether the sample presents magnetic response or not. In the samples where there are two magnets instead of only one it means that the sample reacts greatly to the magnet, resulting in a qualitative analysis of the magnitude of its magnetic susceptibility.

As we have observed for all these samples the formation of new Au or AuFe NPs, we have adapted the synthesis aiming at avoiding the formation of these new NPs by not adding the $\text{Au}(\text{COOCH}_3)_3$ precursor to the reaction system.

3.2.2.B Synthesis without $\text{Au}(\text{COOCH}_3)_3$

The synthesis performed without using $\text{Au}(\text{COOCH}_3)_3$ are described on table 3.3.

Table 3.3: Au-AuFe nanoparticles synthesis without gold precursor. The number of magnets beside each sample represents, qualitatively, the magnitude of the magnetic susceptibility of the sample.

Sample	AuNPs:Fe Ratio	Solvent	Synthesis Parameters		TEM observations	
			Temperature	Time		
SS24	1:1	Octadecene	i) 250°C ii) 290°C	i) 1h ii) 30min	7,5 ± 1,9 nm iron oxide domains grown around the gold nanoseeds	
SS27	1:1		180°C	2h	7,9 ± 1,2 nm lots of aggregates; presence of iron oxide	
SS25	1:1	Dioctyl ether	i) 250°C ii) 290°C	i) 1h ii) 30min	7,8 ± 2,1 nm some gold nanoseeds present iron oxide domains	
SS28	1:1		180°C	2h	6,2 ± 1,5 nm lots of aggregates	

At first, the protocol of Figure 2.2 was tested at higher temperatures: after reacting for one hour at 250 °C, the temperature was increased until 290 °C (closer to the boiling point of the solvent) for half an hour, using once again distinct solvents, octadecene and dioctyl ether, hence leading to samples SS24 and SS25, respectively. Afterwards, the protocol was tested at lower temperatures, and instead of having 250 °C for one hour, the temperature was decreased to 180 °C for two hours. Once again, octadecene and dioctyl ether were used to perform the same protocol, resulting into samples SS27 and SS28, respectively. All of the synthesis mentioned without using $\text{Au}(\text{COOCH}_3)_3$ were performed using a molar ratio of AuNPs seeds to $\text{Fe}(\text{CO})_5$ (AuNPs:Fe) of 1:1.

UV-visible spectra of both sample SS24 and respective AuNPs seeds (SS23) are represented on Figure 3.25, in which it is visible that the NPs synthesized are colloidally stable and present a peak shift from the AuNPs seeds of 34 nm, suggesting conformational changes. Furthermore, this conformational changes are then confirmed by TEM images (Figure 3.25), that demonstrate the formation of big gray

domains around the black AuNPs seeds, probably implying, from its lighter color, the formation of iron oxide domains. However, it is also perceptible that there is a growth of about 0,6 nm from the initial AuNPs seeds to the black NPs visible on TEM images, which can be due to the formation of an AuFe alloy in the interface between the iron oxide domains and the AuNPs.

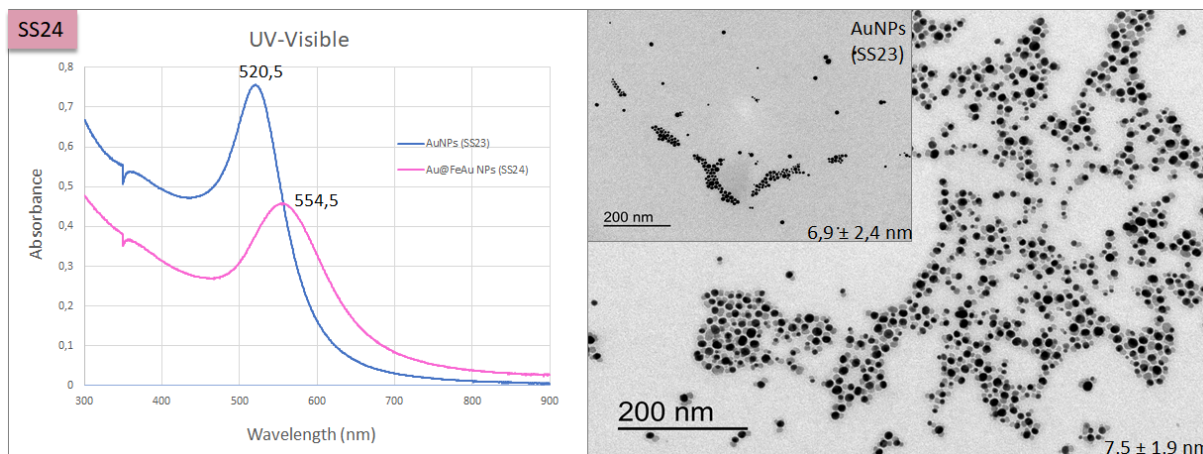


Figure 3.25: Characterization results of synthesis SS24 and respective AuNPs seeds (SS23): UV-visible spectra and TEM images with 200kX and 150kX of magnification, respectively.

Concerning sample SS25, the UV-visible spectra demonstrated on Figure B.8 indicates colloidal stability and a peak shift of 14 nm from the initial AuNPs seeds to the newly formed NPs, that comparing to the results observed on sample SS24, indicate less conformational changes. These results are once again confirmed by the TEM images presented on Figure B.8, since it is visible the formation of some grayer dimers around the black AuNPs, clearly presenting less gray domains than the ones observed on sample SS24. Likewise for the previous sample, these grayer domains are thought out to be iron oxide, since both SS24 and SS25 samples present high magnetic response (represented on table 3.2). There is also a growth of the black AuNPs of about 0,9 nm, which may suggest the formation of an AuFe alloy on the interface between the black NPs and the gray domains.

Observing UV-visible spectrum of sample SS27 on Figure B.9, the absorbance noticed at higher wavelengths present high values, suggesting the presence of a great amount of aggregates. Furthermore, a peak shift from the AuNPs seeds to the final NPs is visible with a value around 49 nm, however it is not viable to claim that this shift can be all due to conformational changes caused by the presence of AuFe hybrid NPs, since it is not considerably pronounced and also, this shift should be mainly caused by the aggregates observed on TEM images (Figure B.9). Despite all of the aggregates contemplated, there is an increase of 1,3 nm in the size of NPs from the initial AuNPs seeds to the final AuFe hybrid NPs, indicating that the NPs outside the aggregates could have formed a shell around the AuNPs seeds.

Regarding sample SS28, both UV-visible spectrum and TEM images (Figure B.10) suggest the presence of aggregates, nevertheless the amount of aggregates observed on sample SS28 is lower than

the one observed on sample SS27, which is sustained with both the UV-visible data and TEM images of both samples. However, UV-visible spectra present a peak shift from the AuNPs seeds to the final NPs obtained of 58,5 nm, which is higher than the one observed on sample SS27, not concordant to the fact that more aggregates are verified on this sample. From TEM images, it is also perceptible that there hasn't been a visible growth from the initial AuNPs seeds to the final NPs obtained, implying that a shell hasn't been formed.

Additionally, samples SS27 and SS28 show magnetic response (less than samples SS24 and SS25, as represented on table 3.3), therefore there is the presence of either metallic Fe or Fe₃O₄ into the NPs formed, since Au in the bulk form is not magnetic.

Comparing to the synthesis described on table 3.2, it is visible that there is only one size of nanoparticles when excluding the Au(COOCH₃)₃, suggesting that the formation of smaller AuNPs from the precursor was avoided, as intended. However, when using the protocol at lower temperatures for longer (samples SS27 and SS28, 180 °C for 2h), a great amount of aggregates are observed, meaning that the samples are not colloidally stable. Thus, more interesting samples are obtained when using higher temperatures (samples SS24 and SS25, 250 °C for one hour and 290 °C for half an hour), although there is also the formation of what appears to be Fe₃O₄ domains.

Comparing the solvent used, the protocol was tested using both octadecene and dioctylether, in which it has been reported by E. Fantechi et al.⁶⁰ that the morphology can be tuned from dimer to flower-like by changing solvent polarity. As demonstrated on Figure 3.26, when using octadecene, flower-like NPs are obtained, contrariwise to the dimers obtained when using dioctylether, which is accordingly to the expected since the different polarities of the solvents lead to NPs with different morphologies.

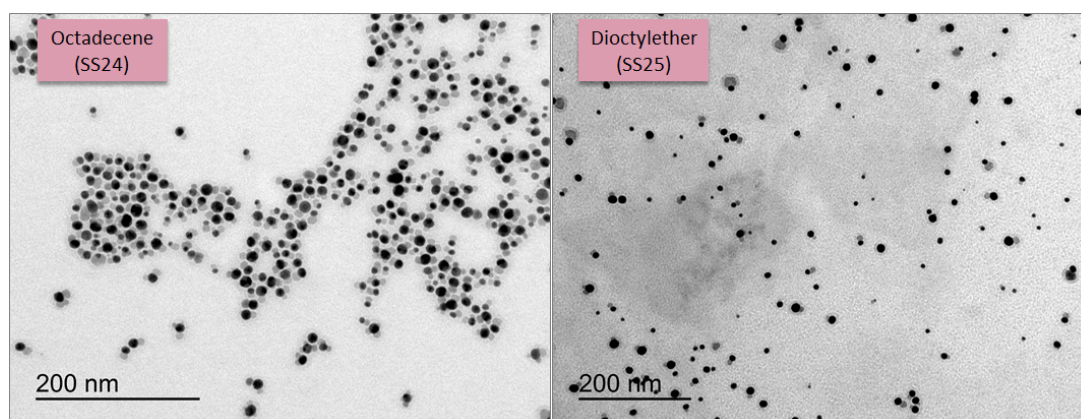


Figure 3.26: TEM images of samples SS24 and SS25.

Overall, UV-visible spectra obtained for all the samples mentioned above present wider peaks than the ones observed for the respective AuNPs seeds, meaning that there are different sizes of NPs in the same sample, and can be indicative to an AuFe alloy. However, in the samples where the Au(COOCH₃)₃

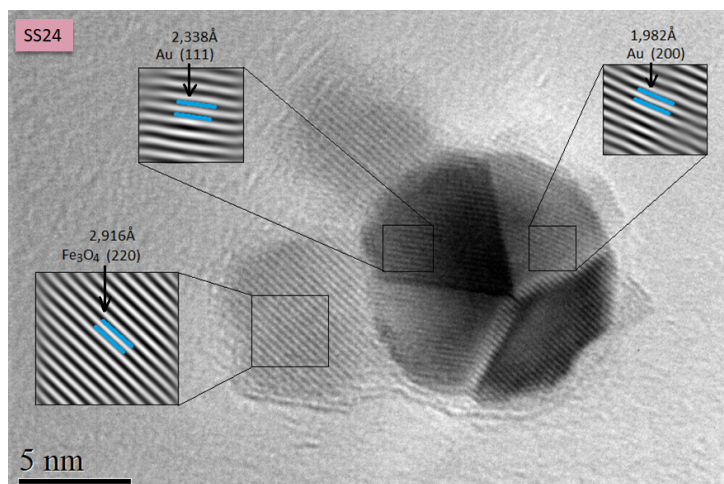


Figure 3.27: HRTEM image of sample SS24 and respective crystalline plans analysis with Digital Microsoft.

was excluded, the formation of either aggregates or Fe_3O_4 domains was observed. In fact, since in the low resolution TEM images it is not reliable to claim that the gray domains are in fact Fe_3O_4 , the sample SS24 (that present the biggest gray domains) was submitted to HRTEM, and the crystalline plans were then analysed with Digital Microsoft software. It was confirmed the existence of AuNPs with Fe_3O_4 domains on its surface, as demonstrated on Figure 3.27.

Concluding, most probably when excluding the $\text{Au}(\text{COOCH}_3)_3$, the AuFe alloy is not formed. On the other hand, when $\text{Au}(\text{COOCH}_3)_3$ was used, new NPs were formed. In any of the two protocols it cannot be completely proven the presence of AuFe alloy either as a shell of the preformed AuNPs or in the form of the newly NPs arisen.

Reaction Progress

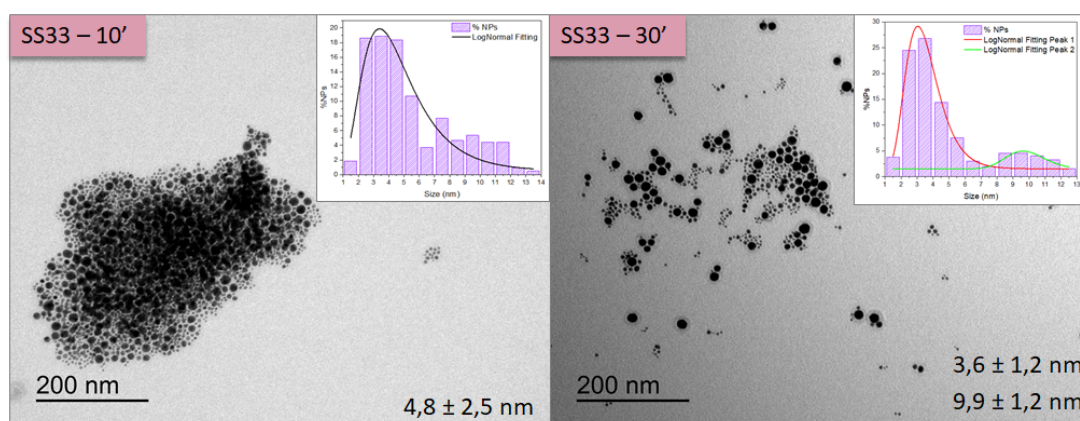


Figure 3.28: TEM images of sample SS33 at 10', 30' and 60' of reaction.

In all the samples mentioned on this master thesis, the reaction progress was studied by characterization of the sample at different reaction times. For sample SS33, TEM images at 10 and 30 minutes

of reaction (Figure 3.28) demonstrate that after 10 minutes of $\text{Fe}(\text{CO})_5$ injection a lot of aggregates are formed and with the increasing of reaction time the sample presents higher colloidal stability. Its UV-visible spectra are demonstrated on Figure B.6.

Overall, the reaction progress registered for the other samples was similar to the one described herein.

3.2.3 UV-visible Spectroscopy

Since the samples studied in this master thesis contained gold, the evaluation of its optical properties was crucial, hence UV-visible spectroscopy was a widely used technique throughout all the experiment procedures.

As stated on section 2.2, the hardware used to acquire this data was a Cary 100 UV-visible spectrophotometer using a simple design that reduces the chance of user error due to mismatched cuvettes or incorrect sample placement,⁶¹ and it's designated as a double beam optical system, as schematized on Figure 3.29. In the double beam system, the light emitted from the source is split into two beams, a reference beam and a sample beam, each of them with separate optical paths that lead to its own detector. Thus, there are two detectors, one for the reference and the other for the sample. In fact, to register the base line, the solvent is measured in both the sample and reference position, being then subtracted from the sample spectrum after each collection. This way, the reference detector is used to correct brightness fluctuations on each measurement.⁶¹

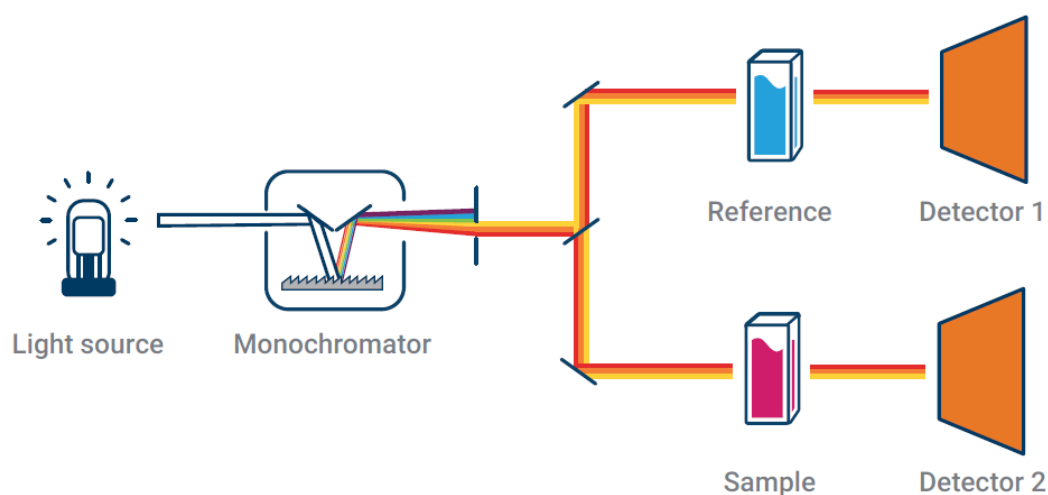


Figure 3.29: Schematic diagram of UV-visible spectroscopy with double beam optical system.⁶¹

The UV-visible spectra mentioned on section 3.2.2 compare the AuNPs seeds with the Au-AuFe core-shell NPs, however the gold nanoseeds solvent is hexane while toluene is the solvent of the core-

shell NPs. Since the reference used to obtain each spectrum was achieved by using the solvent of each sample, the spectra that compare both NPs can present a shift related to the different polarities of the solvents used, that present different dielectric constants, leading to differences on the interaction between the solvent and the NPs surface, then translating into different UV-visible responses.

In order to evaluate the magnitude of this shift, UV-visible spectra were obtained with the same sample of AuNPs, using toluene and hexane as reference. The spectra obtained are represented on Figure 3.30.

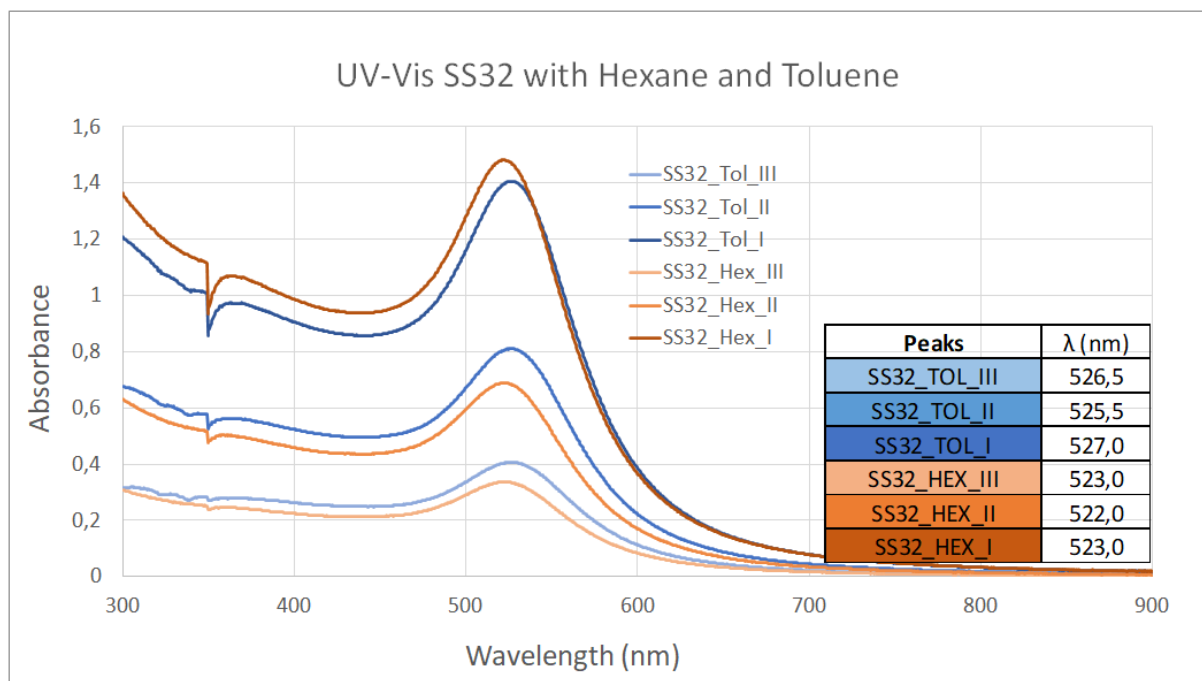


Figure 3.30: UV-visible spectra using both toluene and hexane as reference, and respective peak wavelengths.

Analysing Figure 3.30, the peak shift is about 3,5-4 nm, which can be translated into the contribution of polarities differences between each solvent.

This analysis show that the peak shift observed on UV-visible spectra is mainly due to reasons other than the different polarities of the solvents used, such as different sized nanoparticles and/or with different compositions. Hence, the observations concluded on sections above are accurate.

4

Conclusions and Future Work

The main purpose of this Master Thesis was to synthesize spherical Au-AuFe core-shell hybrid magneto-plasmonic nanoparticles, developing a functional protocol that could further be adapted to the synthesis of Au-AuFe core-shell nanorods. The synthesis of this type of nanorods was motivated by the extensive list of biomedical applications in which it can be incorporated into.

To obtain hybrid magneto-plasmonic nanorods would be a great achievement for all sorts of biomedical approaches, as it would take advantages of both magnetic and plasmonic properties of these structures, along with its NIR-responsive feature provided by the rod shape. In fact, such NPs would be crucial for both cancer diagnostic and treatment techniques:

- **Diagnostic:** It could be incorporated into imaging techniques based on its magnetic susceptibility, namely MRI, in which magneto-plasmonic nanorods could serve as contrast agents to enhance contrast on the MRI images obtained and thus provide higher resolution images aiming to detect smaller, growing tumours that the present contrast agent used for the same purpose cannot.
- **Treatment:** Regarding cancer treatment, it can be incorporated on already existing magnetically-based treatments or it can be used as magnetically-guided drug carriers.
 - **Magnetic Hyperthermia:** Provided that the desired nanorods would have high magnetic susceptibility, it could be incorporated magnetic hyperthermia cancer treatments, which takes advantage of magnetic NPs to produce the local heating of the target cells, and since tumour cells have low levels of oxygen, its heating aims to kill this cells without affecting healthy cells in the surroundings. Its NIR-responsive nature permits its handling after being stimulated to a remote signal, which would as well lead to the accumulation of the synthesized nanorods into the target site, thus improving cancer treatment through magnetic hyperthermia.
 - **Drug Delivery:** Magnetically-guided drug delivery systems could also be improved by incorporating such nanomaterials. Cancer treatment drugs, namely doxorubicin used on chemotherapy are also lethal to healthy cells, leading to a number of undesired side-effects, which can be avoided by encapsulating the same drugs on magnetic, NIR-responsive NPs that have the capacity of delivering the drug on the target site by external stimuli, in a non-invasive way and with less side-effects than the techniques currently used for the same purpose, while not only providing its protection but also increasing its bioavailability.

In order to achieve our goal, the synthesis of spherical AuNPs were firstly carried out, and as it is a widely investigated matter, there are a lot of reported protocols to be followed. This way, two different protocols were tested and it was possible to choose the one that showed more interesting results and it was optimized, in order to obtain AuNPs that would be suitable to be used as seeds to grow an AuFe alloy shell on the second part of the experimental work.

The attempt to synthesize Au-AuFe core-shell NPs was performed by following a published protocol in which monodisperse FeAu NPs were synthesized, testing different Au:Fe molar ratios. This protocol was adapted in order to use the AuNPs previously obtained to grow an AuFe shell, and was then tested by changing a few parameters, such as the use of gold precursor, the molar ratio of AuNPs:Au:Fe and the solvent used, in order to study their effect on the final NPs obtained.

In the absence of gold precursor, a decreasing of temperature and increasing of the reaction time led to NPs with low colloidal stability. On the other hand, an increasing of temperature and decreasing of reaction time led to the formation of a great amount of iron oxide domains on the resulted NPs, which was enough data to dismiss deeper characterization analysis on these samples. Furthermore, it is possible to conclude that the use of octadecene as solvent originated the formation of flower-like NPs, while the use of dioctyl ether led to the formation of iron oxide dimers on the AuNPs.

In the presence of gold precursor, more interesting results were obtained. In fact, when the molar ratio of AuNPs:Au:Fe used was 1:1:1 and the solvent was octadecene, we were able to obtain highly magnetic nanoparticles that didn't exhibit the peaks of iron on both XPS and XRD spectra, consisting on conflicting data, since the gold does not present magnetism. Further on, more data should be collected towards the investigation of why this sample presents magnetism if the values of iron verified are lower enough not to appear on both XPS and XRD measurements.

Finally, for a molar ratio AuNPs:Au:Fe of 1:2:2 and using dioctyl ether as solvent, we were able to obtain small NPs with a mean size of 3,3 nm that seems to contain the desired AuFe alloy with an amount of 80% of Au and 20% of Fe, which is the maximum amount of iron we would be able to obtain on an AuFe alloy. This way, it is possible to infer that the majority of NPs obtained on this sample were simply AuNPs seeds initially added to the reaction that then grew in size with the assistance of the gold precursor added, and a minority of smaller NPs that can probably contain AuFe, which is concordant to the obtained by the original protocol.

Although the desired spherical Au-AuFe core-shell nanoparticles seems not to have been achieved, it was possible to conclude that through a colloidal synthesis it is very difficult to obtain the AuFe alloy as a shell. Futurely, since higher temperatures demonstrated to lead to better results, it would be interesting to use a non-colloidal synthesis in which more energy (i.e. higher temperature) is provided in order to promote the binding between gold and metallic iron.

Bibliography

- ¹ M. C. Gonçalves, "Nanomaterials," pp. 727–771, 2015.
- ² L. H. Madkour, "Classification of nanostructured materials," in *Nanoelectronic Materials*. Springer, 2019, pp. 269–307.
- ³ Y. Gogotsi, *Nanomaterials handbook*. CRC press, 2006.
- ⁴ M. N. Sadiku, T. J. Ashaolu, A. Ajayi-Majebi, and S. M. Musa, "Future of nanotechnology," *International Journal of Scientific Advances*, vol. 2, 2021.
- ⁵ C. Buzea and I. Pacheco, "Nanomaterials and their classification," in *EMR/ESR/EPR Spectroscopy for Characterization of Nanomaterials*. Springer, 2017, pp. 3–45.
- ⁶ V. Nayak, S. M. Munawar, K. B. Sabjan, S. Singh, and K. R. Singh, "Nanomaterials' properties, classification, synthesis, and characterization 1," in *Nanomaterials in Bionanotechnology*. CRC Press, 2021, pp. 37–68.
- ⁷ S. Haldar and H. J. Grzyb, "Nanoparticles: The wonders of nanoscale," 2021.
- ⁸ S. Y. Lim, W. Shen, and Z. Gao, "Carbon quantum dots and their applications," *Chemical Society Reviews*, vol. 44, no. 1, pp. 362–381, 2015.
- ⁹ J. Park, J. C. Hwang, G. G. Kim, and J.-U. Park, "Flexible electronics based on one-dimensional and two-dimensional hybrid nanomaterials," *InfoMat*, vol. 2, no. 1, pp. 33–56, 2020.
- ¹⁰ J. Wong-Leung, I. Yang, Z. Li, S. K. Karuturi, L. Fu, H. H. Tan, and C. Jagadish, "Engineering iii–v semiconductor nanowires for device applications," *Advanced Materials*, vol. 32, no. 18, 2020.
- ¹¹ S. Mousavi, S. Hashemi, S. Mazraedoost, K. Yousefi, A. Gholami, G. Behbudi, S. Ramakrishna, N. Omidifar, A. Alizadeh, and W. Chiang, "Multifunctional gold nanorod for therapeutic applications and pharmaceutical delivery considering cellular metabolic responses, oxidative stress, and cellular longevity. *nanomaterials* 2021, 11, 1868," 2021.

- ¹² A. Ranzoni and M. Cooper, "The growing influence of nanotechnology in our lives," in *Micro and nanotechnology in vaccine development*. Elsevier, 2017, pp. 1–20.
- ¹³ V. S. Raghuwanshi and G. Garnier, "Cellulose nano-films as bio-interfaces," *Frontiers in chemistry*, vol. 7, p. 535, 2019.
- ¹⁴ H. Pang, X. Cao, L. Zhu, and M. Zheng, "Synthesis of three-dimensional nanomaterials," in *Synthesis of Functional Nanomaterials for Electrochemical Energy Storage*. Springer, 2020, pp. 79–105.
- ¹⁵ T. Y. Poh, N. A. B. M. Ali, M. Mac Aogáin, M. H. Kathawala, M. I. Setyawati, K. W. Ng, and S. H. Chotirmall, "Inhaled nanomaterials and the respiratory microbiome: clinical, immunological and toxicological perspectives," *Particle and fibre toxicology*, vol. 15, no. 1, pp. 1–16, 2018.
- ¹⁶ L. Rashidi, "Magnetic nanoparticles: synthesis and characterization," in *Magnetic Nanoparticle-Based Hybrid Materials*. Elsevier, 2021, pp. 3–32.
- ¹⁷ P. N. Sudha, K. Sangeetha, K. Vijayalakshmi, and A. Barhoum, "Nanomaterials history, classification, unique properties, production and market," in *Emerging Applications of Nanoparticles and Architecture Nanostructures*. Elsevier, 2018, pp. 341–384.
- ¹⁸ M. Singh, S. Lara, and S. Tlali, "Effects of size and shape on the specific heat, melting entropy and enthalpy of nanomaterials," *Journal of Taibah University for Science*, vol. 11, no. 6, pp. 922–929, 2017.
- ¹⁹ G. Kandasamy and D. Maity, "Recent advances in superparamagnetic iron oxide nanoparticles (spions) for in vitro and in vivo cancer nanotheranostics," *International journal of pharmaceutics*, vol. 496, no. 2, pp. 191–218, 2015.
- ²⁰ S. Singh, V. K. Pandey, R. P. Tewari, V. Agarwal *et al.*, "Nanoparticle based drug delivery system: advantages and applications," *Indian J Sci Technol*, vol. 4, no. 3, pp. 177–180, 2011.
- ²¹ D. Peddis, S. Laureti, and D. Fiorani, *New Trends in Nanoparticle Magnetism*. Springer, 2021.
- ²² A. Onaciu, C. Braicu, A.-A. Zimta, A. Moldovan, R. Stiufiuc, M. Buse, C. Ciocan, S. Buduru, and I. Berindan-Neagoe, "Gold nanorods: From anisotropy to opportunity. an evolution update," *Nanomedicine*, vol. 14, no. 9, pp. 1203–1226, 2019.
- ²³ M. Goyal and M. Singh, "Size and shape dependence of optical properties of nanostructures," *Applied Physics A*, vol. 126, no. 3, pp. 1–8, 2020.
- ²⁴ V. P. Ananikov, "Organic–inorganic hybrid nanomaterials," *Multidisciplinary Digital Publishing Institute*, 2019.

- ²⁵ J. Yuan and A. H. Müller, "One-dimensional organic–inorganic hybrid nanomaterials," *Polymer*, vol. 51, no. 18, pp. 4015–4036, 2010.
- ²⁶ W. Park, H. Shin, B. Choi, W.-K. Rhim, K. Na, and D. K. Han, "Advanced hybrid nanomaterials for biomedical applications," *Progress in Materials Science*, vol. 114, 2020.
- ²⁷ D. C. F. Soares, S. C. Domingues, D. B. Viana, and M. L. Tebaldi, "Polymer-hybrid nanoparticles: Current advances in biomedical applications," *Biomedicine & Pharmacotherapy*, vol. 131, 2020.
- ²⁸ G. Choi, N. S. Rejinold, H. Piao, and J.-H. Choy, "Inorganic–inorganic nanohybrids for drug delivery, imaging and photo-therapy recent developments and future scope," *Chemical Science*, 2021.
- ²⁹ S. Mohapatra, T. A. Nguyen, and P. Nguyen-Tri, *Noble metal-metal oxide hybrid nanoparticles: Fundamentals and applications*. Elsevier, 2018.
- ³⁰ N. Vyšetrovanie, M. S. V. Feromagnetických, and N. P. H. Magnetometrie, "Noninvasive control of magnetic state in ferromagnetic nanodots by hall probe magnetometry," *Research Gate*, 2016.
- ³¹ J. Asselin, C. Boukouvala, E. R. Hopper, Q. M. Ramasse, J. S. Biggins, and E. Ringe, "Tents, chairs, tacos, kites, and rods: Shapes and plasmonic properties of singly twinned magnesium nanoparticles," *ACS nano*, vol. 14, no. 5, pp. 5968–5980, 2020.
- ³² K. Khurana and N. Jaggi, "Localized surface plasmonic properties of au and ag nanoparticles for sensors: A review," *Plasmonics*, pp. 1–19, 2021.
- ³³ E. Ringe, "Shapes, plasmonic properties, and reactivity of magnesium nanoparticles," *The Journal of Physical Chemistry C*, vol. 124, no. 29, pp. 15 665–15 679, 2020.
- ³⁴ Nicoya. (2021, August) LSPR vs SPR. Accessed 25-August-2021. [Online]. Available: <https://nicoyalife.com/nicoya-surface-plasmon-resonance-resources/what-is-spr/lSpr-vs-spr-2/>
- ³⁵ T. Wriedt, "Mie theory: a review," *The Mie Theory*, pp. 53–71, 2012.
- ³⁶ J. E. Ortiz-Castillo, R. C. Gallo-Villanueva, M. J. Madou, and V. H. Perez-Gonzalez, "Anisotropic gold nanoparticles: A survey of recent synthetic methodologies," *Coordination Chemistry Reviews*, vol. 425, p. 213489, 2020.
- ³⁷ H. Chen, L. Shao, Q. Li, and J. Wang, "Gold nanorods and their plasmonic properties," *Chemical Society Reviews*, vol. 42, no. 7, pp. 2679–2724, 2013.
- ³⁸ F. Fathi, M.-R. Rashidi, and Y. Omid, "Ultra-sensitive detection by metal nanoparticles-mediated enhanced spr biosensors," *Talanta*, vol. 192, pp. 118–127, 2019.

- ³⁹ A. Tomitaka, H. Arami, A. Ahmadivand, N. Pala, A. J. McGoron, Y. Takemura, M. Febo, and M. Nair, "Magneto-plasmonic nanostars for image-guided and nir-triggered drug delivery," *Scientific reports*, vol. 10, no. 1, pp. 1–10, 2020.
- ⁴⁰ A. Espinosa, J. Reguera, A. Curcio, Á. Muñoz-Noval, C. Kuttner, A. Van de Walle, L. M. Liz-Marzán, and C. Wilhelm, "Janus magnetic-plasmonic nanoparticles for magnetically guided and thermally activated cancer therapy," *Small*, vol. 16, no. 11, 2020.
- ⁴¹ S. Szunerits, T. Nait Saada, D. Meziane, and R. Boukherroub, "Magneto-optical nanostructures for viral sensing," *Nanomaterials*, vol. 10, no. 7, p. 1271, 2020.
- ⁴² E. A. Kwizera, E. Chaffin, Y. Wang, and X. Huang, "Synthesis and properties of magnetic-optical core-shell nanoparticles," *RSC advances*, vol. 7, no. 28, pp. 17 137–17 153, 2017.
- ⁴³ M. V. Efremova, M. Spasova, M. Heidelmann, I. S. Grebennikov, Z.-A. Li, A. S. Garanina, I. O. Tcareva, A. G. Savchenko, M. Farle, N. L. Klyachko *et al.*, "Room temperature synthesized solid solution au/fe janus nanocrystals," *Nanoscale*, 2021.
- ⁴⁴ M. A. M. Tarkistani, V. Komalla, and V. Kayser, "Recent advances in the use of iron-gold hybrid nanoparticles for biomedical applications," *Nanomaterials*, vol. 11, no. 5, p. 1227, 2021.
- ⁴⁵ A. J. Haider, M. A. Al-Kinani, and S. Al-Musawi, "Preparation and characterization of gold coated super paramagnetic iron nanoparticle using pulsed laser ablation in liquid method," in *Key Engineering Materials*, vol. 886. Trans Tech Publ, 2021, pp. 77–85.
- ⁴⁶ I.-C. Chiang and D.-H. Chen, "Synthesis of monodisperse fe₃o₄ nanoparticles with tunable magnetic and optical properties," *Advanced Functional Materials*, vol. 17, no. 8, pp. 1311–1316, 2007.
- ⁴⁷ R. Downs, K. Bartelmehs, G. Gibbs, and M. Boisen, "Interactive software for calculating and displaying x-ray or neutron powder diffractometer patterns of crystalline materials," *American Mineralogist*, vol. 78, no. 9-10, pp. 1104–1107, 1993.
- ⁴⁸ H. E. Swanson, *Standard X-ray diffraction powder patterns*. US Department of Commerce, National Bureau of Standards, 1971, vol. 25.
- ⁴⁹ C. Shen, C. Hui, T. Yang, C. Xiao, J. Tian, L. Bao, S. Chen, H. Ding, and H. Gao, "Monodisperse noble-metal nanoparticles and their surface enhanced raman scattering properties," *Chemistry of Materials*, vol. 20, no. 22, pp. 6939–6944, 2008.
- ⁵⁰ L. Wang, L. Wang, J. Luo, Q. Fan, M. Suzuki, I. S. Suzuki, M. H. Engelhard, Y. Lin, N. Kim, J. Q. Wang *et al.*, "Monodispersed core-shell fe₃o₄@au nanoparticles," *The Journal of Physical Chemistry B*, vol. 109, no. 46, pp. 21 593–21 601, 2005.

- ⁵¹ H.-s. Kim, Y. S. Seo, K. Kim, J. W. Han, Y. Park, and S. Cho, "Concentration effect of reducing agents on green synthesis of gold nanoparticles: size, morphology, and growth mechanism," *Nanoscale research letters*, vol. 11, no. 1, pp. 1–9, 2016.
- ⁵² P. F. de Oliveira, A. A. Michalchuk, J. Marquardt, T. Feiler, C. Prinz, R. M. Torresi, P. H. Camargo, and F. Emmerling, "Investigating the role of reducing agents on mechanosynthesis of au nanoparticles," *CrystEngComm*, vol. 22, no. 38, pp. 6261–6267, 2020.
- ⁵³ C. Moya, X. Battle, and A. Labarta, "The effect of oleic acid on the synthesis of $Fe_{3-x}O_4$ nanoparticles over a wide size range," *Physical Chemistry Chemical Physics*, vol. 17, no. 41, pp. 27 373–27 379, 2015.
- ⁵⁴ W. Haiss, N. T. Thanh, J. Aveyard, and D. G. Fernig, "Determination of size and concentration of gold nanoparticles from uv- vis spectra," *Analytical chemistry*, vol. 79, no. 11, pp. 4215–4221, 2007.
- ⁵⁵ Cytodiagnosics. (2021, October) Introduction to gold nanoparticle characterization. Accessed 8-October-2021. [Online]. Available: <https://www.cytodiagnosics.com/pages/introduction-to-gold-nanoparticle-characterization>
- ⁵⁶ B. Liu and X. Hu, "Hollow micro-and nanomaterials: Synthesis and applications," in *Advanced Nanomaterials for Pollutant Sensing and Environmental Catalysis*. Elsevier, 2020, pp. 1–38.
- ⁵⁷ L. Scarabelli, A. Sánchez-Iglesias, J. Pérez-Juste, and L. M. Liz-Marzán, "A "tips and tricks" practical guide to the synthesis of gold nanorods," *The Journal of Physical Chemistry Letters*, vol. 6, no. 21, pp. 4270–4279, 2015.
- ⁵⁸ D.-K. Kim, Y. J. Hwang, C. Yoon, H.-O. Yoon, K. S. Chang, G. Lee, S. Lee, and G.-R. Yi, "Experimental approach to the fundamental limit of the extinction coefficients of ultra-smooth and highly spherical gold nanoparticles," *Physical Chemistry Chemical Physics*, vol. 17, no. 32, pp. 20 786–20 794, 2015.
- ⁵⁹ T. Yamashita and P. Hayes, "Analysis of xps spectra of Fe^{2+} and Fe^{3+} ions in oxide materials," *Applied surface science*, vol. 254, no. 8, pp. 2441–2449, 2008.
- ⁶⁰ E. Fantechi, C. Innocenti, G. Bertoni, C. Sangregorio, and F. Pineider, "Modulation of the magnetic properties of gold-spinel ferrite heterostructured nanocrystals," *Nano Research*, vol. 13, no. 3, pp. 785–794, 2020.
- ⁶¹ Agilent. (2021, October) The basics of uv-vis spectrophotometry. Accessed 13-October-2021. [Online]. Available: <https://explore.agilent.com/basics-of-uv-vis/>
- ⁶² W. Ding, Y. Liu, Y. Li, Q. Shi, H. Li, H. Xia, D. Wang, and X. Tao, "Water-soluble gold nanoclusters with ph-dependent fluorescence and high colloidal stability over a wide ph range via co-reduction of glutathione and citrate," *RSC advances*, vol. 4, no. 43, pp. 22 651–22 659, 2014.



AuNPs seeds: Synthesis and Characterization

Table A.1: Reagents quantities used on the first AuNPs seeds synthesis protocol.

Reagents (mmol)	SS01	SS02 (decreased 1,2-hexadecanediol in relation to SS01)	SS03 (decreased OLAc in relation to SS01)	SS04 (increased 1,2-hexadecanediol in relation to SS03)
Gold Acetate	0,44	0,44	0,44	0,44
1,2-hexadecanediol	2,4	1,1	2,4	4,4
Oleic acid (OLAc)	1,5	1,5	0,30	0,30
Oleylamine	1,0	1,0	1,0	1,0
Octadecene	5mL			
Gold:1,2-hexadecanediol	1:5,5	1:2,5	1:5,5	1:10
Gold:OLAc	1:3,4	1:3,4	1:0,7	1:0,7

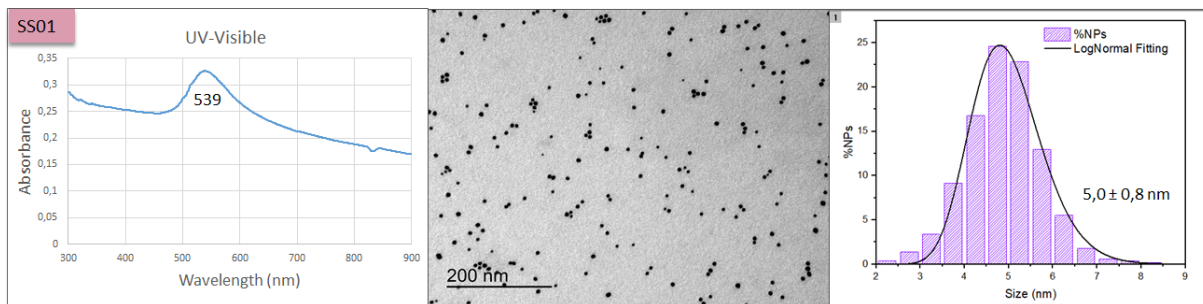


Figure A.1: First Protocol; Characterization results of synthesis SS01: UV-visible spectrum, TEM image with 250kX of magnification and size distribution histogram.

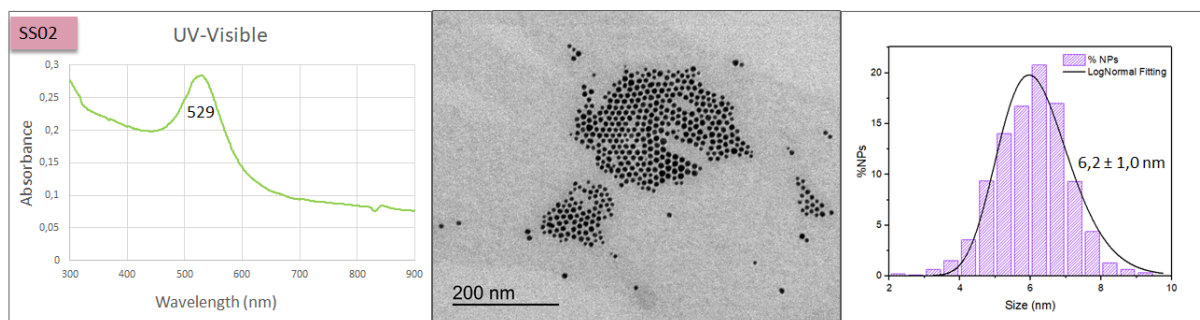


Figure A.2: First Protocol; Characterization results of synthesis SS02: UV-visible spectrum, TEM image with 250kX of magnification and size distribution histogram.

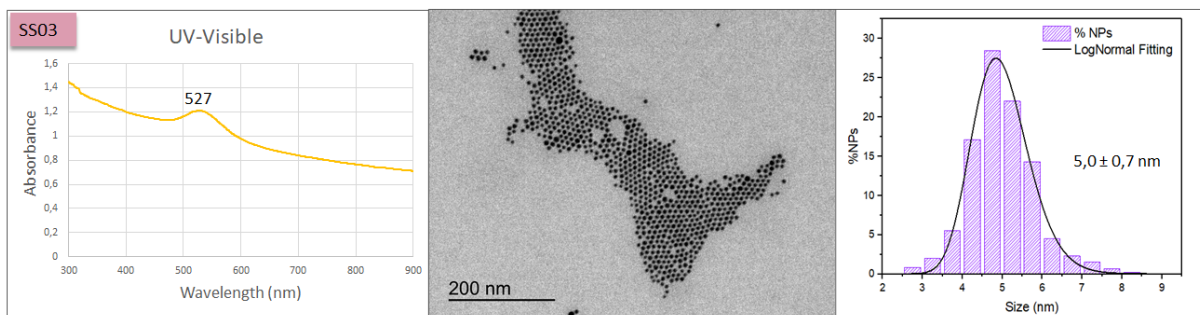


Figure A.3: First Protocol; Characterization results of synthesis SS03: UV-visible spectrum, TEM image with 250kX of magnification and size distribution histogram.

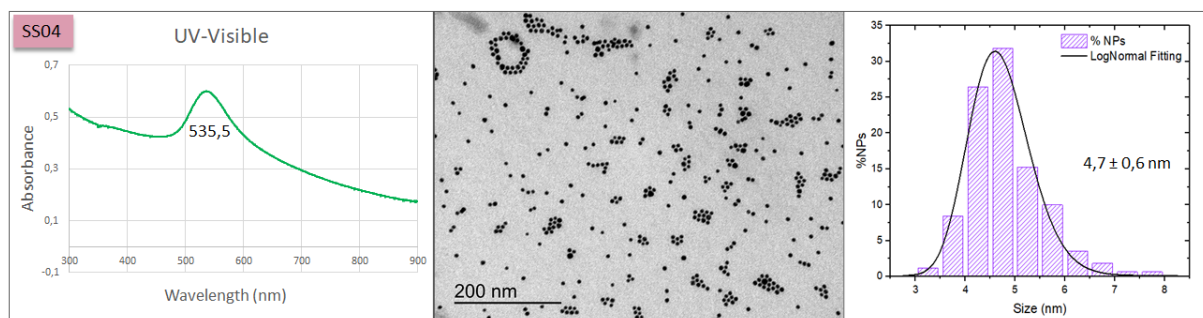


Figure A.4: First Protocol; Characterization results of synthesis SS04: UV-visible spectrum, TEM image with 250kX of magnification and size distribution histogram.

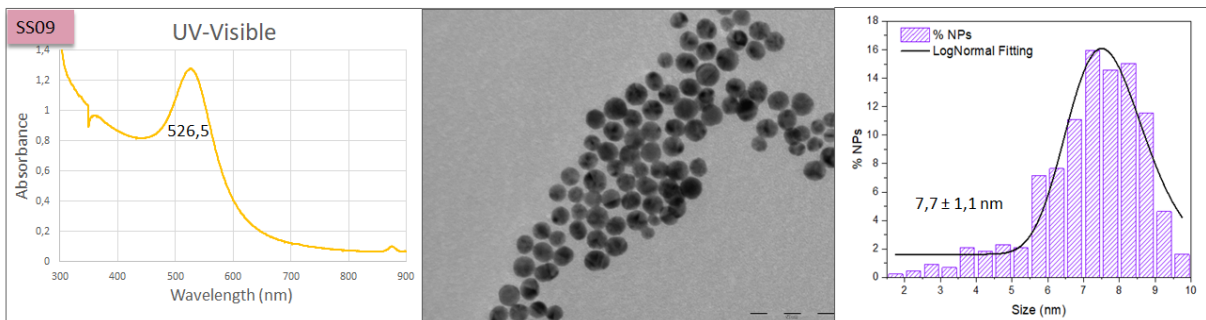


Figure A.5: Second protocol; Characterization results of synthesis SS09: UV-visible spectrum, TEM image with 200kX of magnification and size distribution histogram.

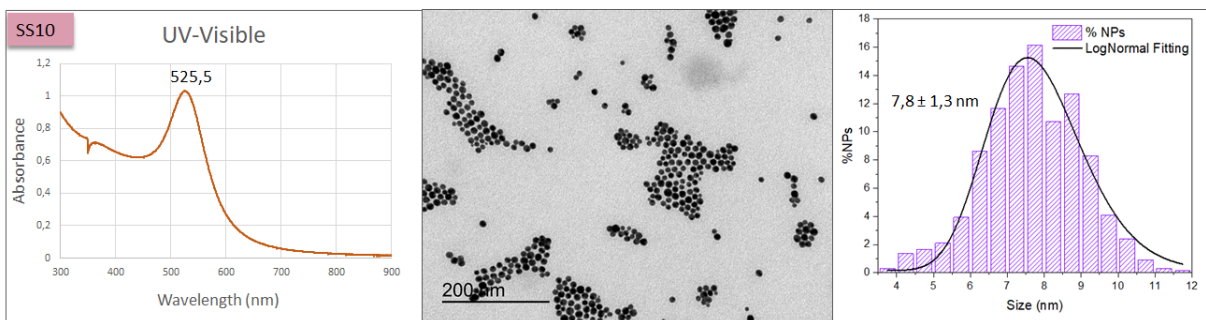


Figure A.6: Second protocol; Characterization results of synthesis SS10: UV-visible spectrum, TEM image with 250kX of magnification and size distribution histogram.

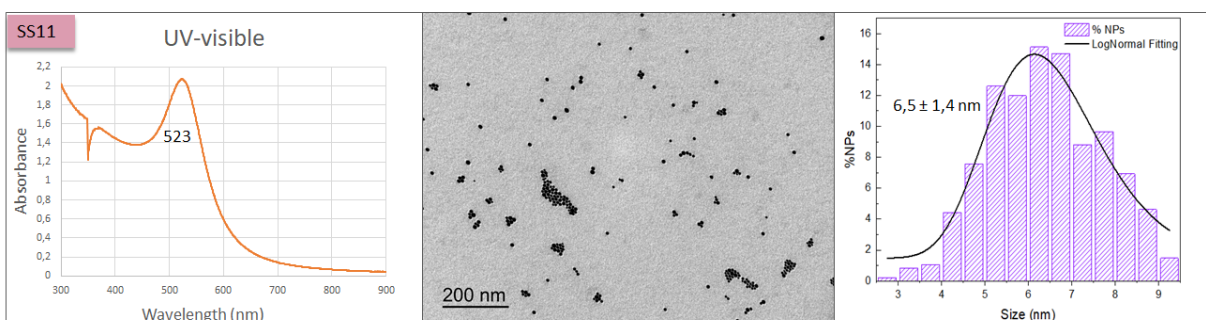


Figure A.7: Second protocol; Characterization results of synthesis SS11: UV-visible spectrum, TEM image with 150kX of magnification and size distribution histogram.

B

Au-AuFe Nanohybrids: Synthesis and Characterization

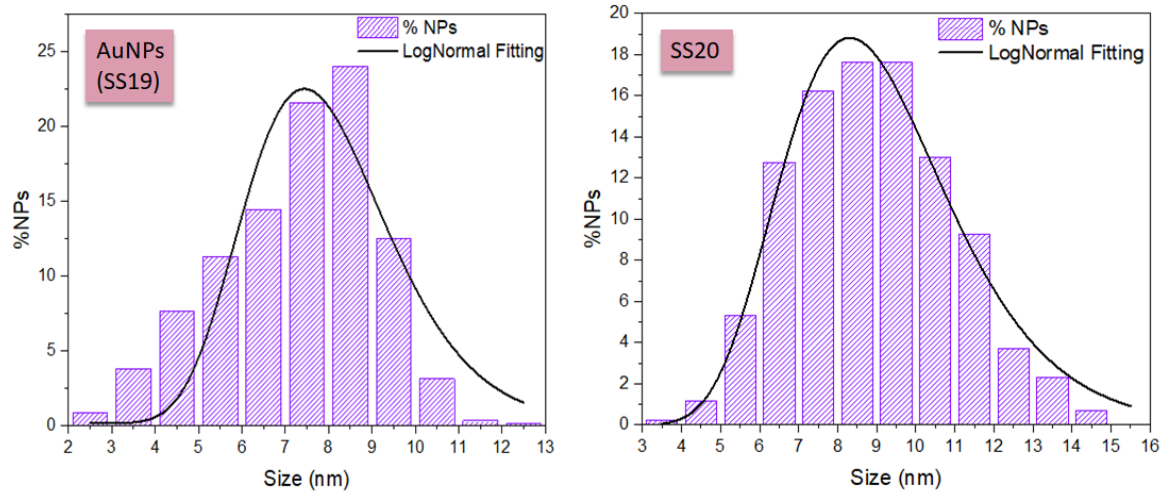


Figure B.1: SS20 Histogram and SS19 (respective AuNPs) Histogram.

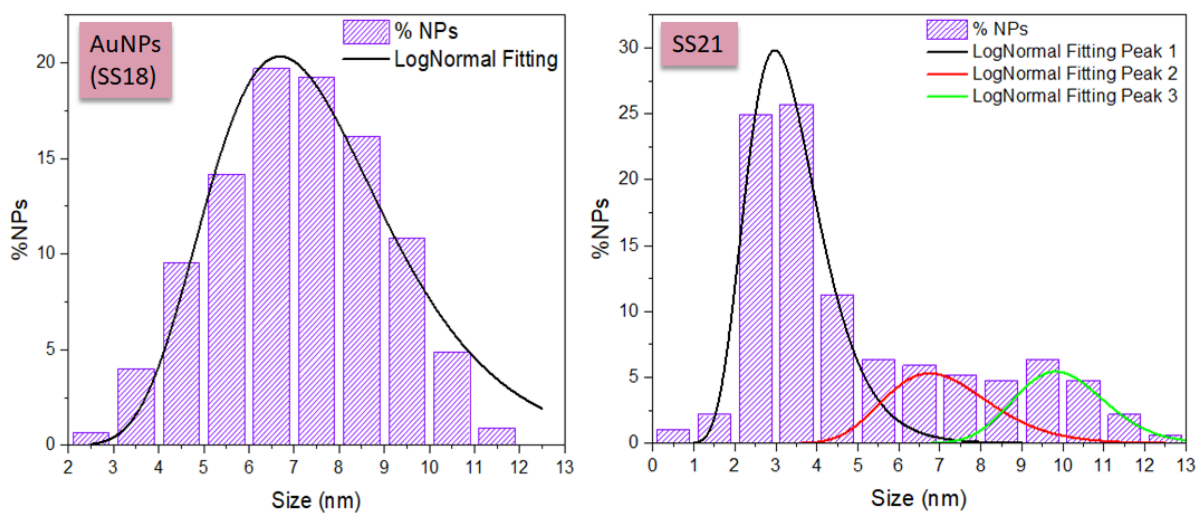


Figure B.2: SS21 Histogram and SS18 (respective AuNPs) Histogram.

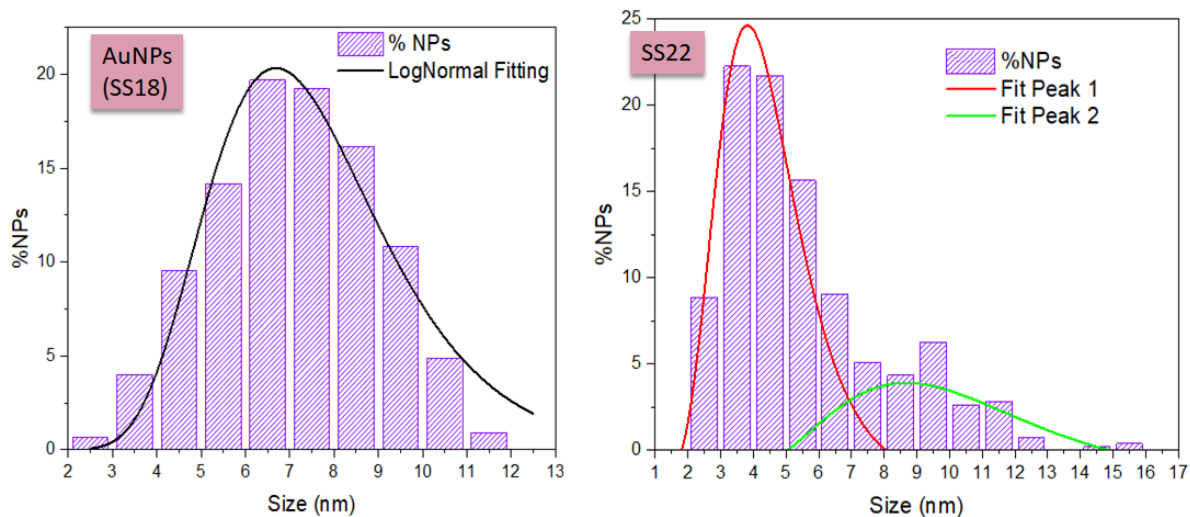


Figure B.3: SS22 Histogram and SS18 (respective AuNPs) Histogram.

Table B.1: Binding energy profiles of Fe 2p.⁵⁹

Oxidized State	Binding Energy (eV)	
	Fe 2p _{3/2}	Fe 2p _{1/2}
Fe ⁰	706,8	719,8
Fe ²⁺	709,8	722,8
Fe ³⁺	711,2	724,3

Table B.2: Binding energy profiles of Au 4f.⁶²

Au (⁰)	Binding Energy (eV)
4f _{7/2}	83,8
4f _{5/2}	87,7

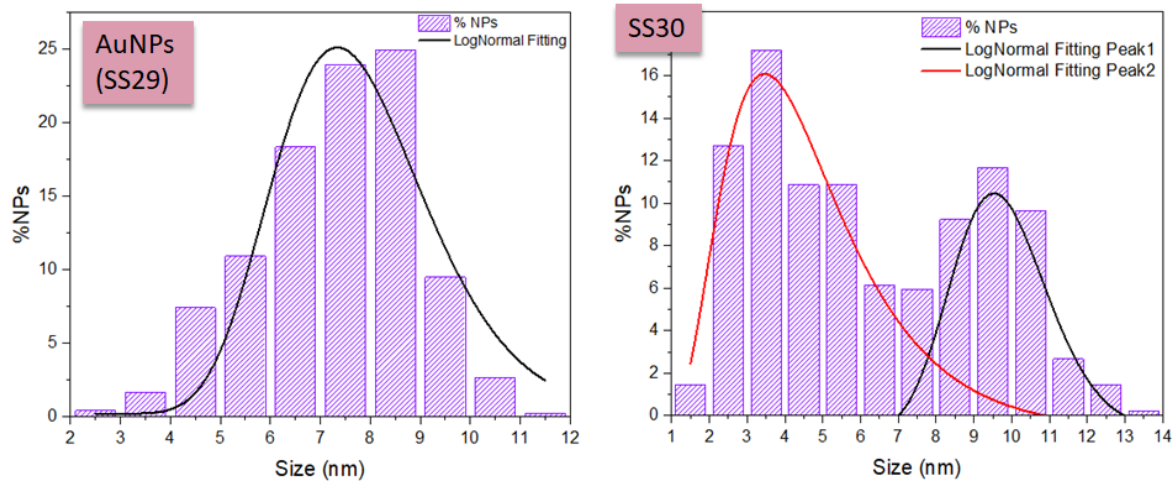


Figure B.4: SS30 Histogram and SS29 (respective AuNPs) Histogram.

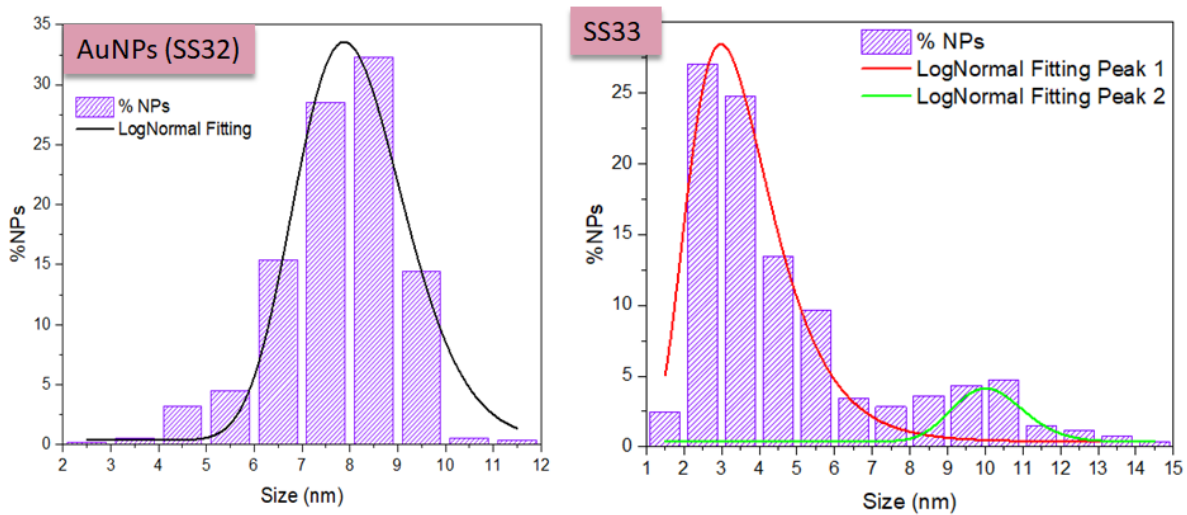


Figure B.5: SS33 Histogram and SS32 (respective AuNPs) Histogram.

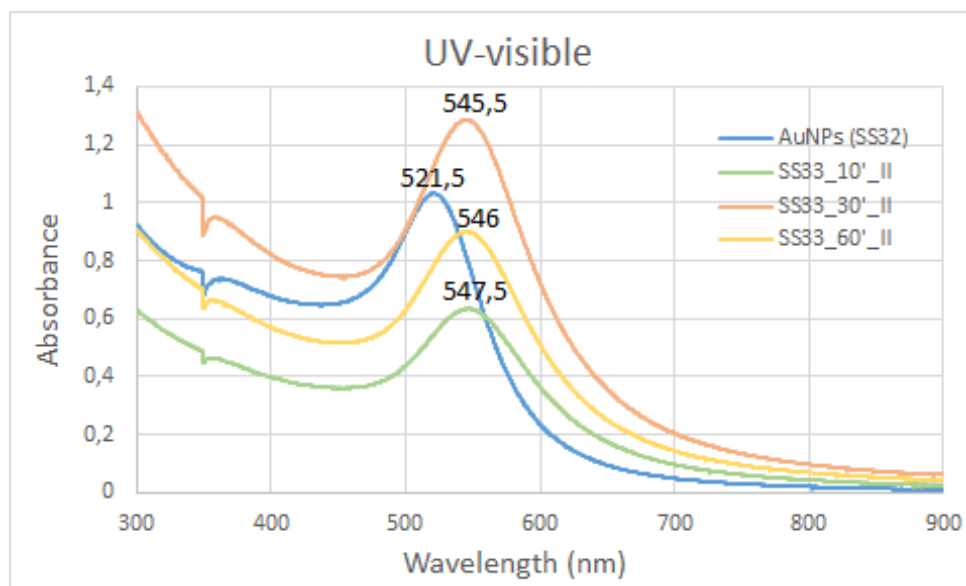


Figure B.6: UV-visible spectra of sample SS33 at 10', 30' and 60' of reaction, and respective AuNPs (SS32).

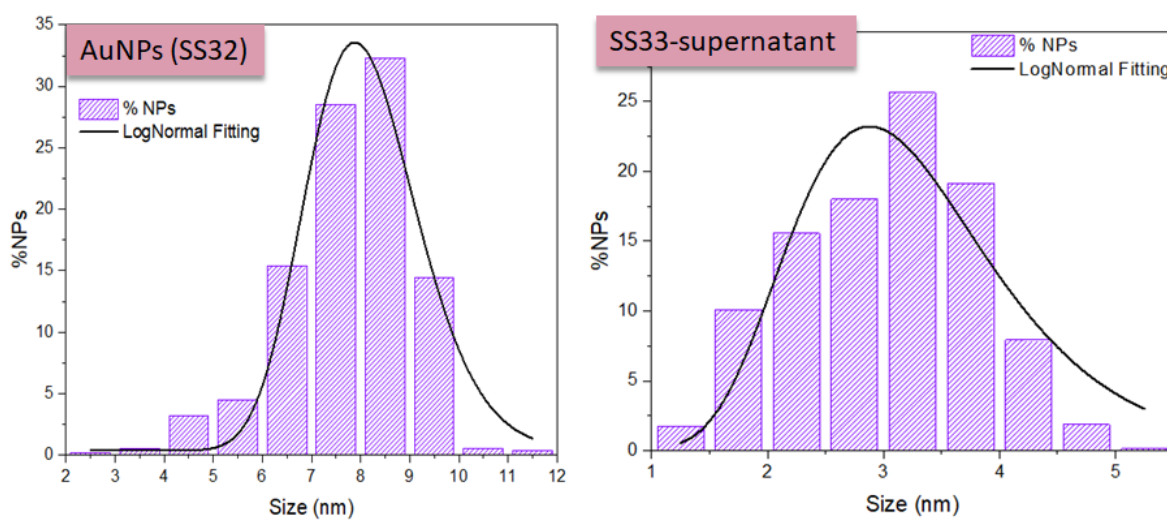


Figure B.7: SS33 supernatant Histogram and SS32 (respective AuNPs) Histogram.

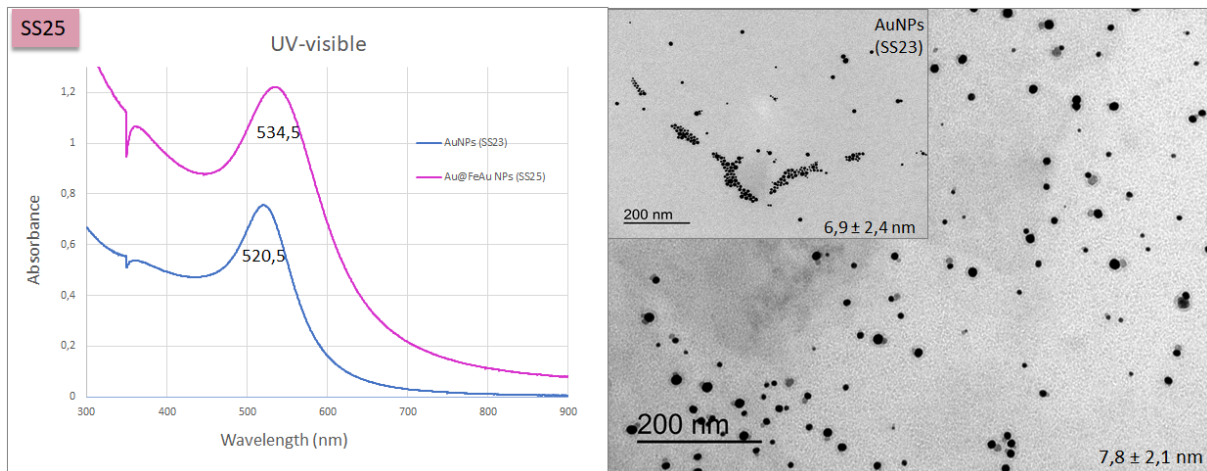


Figure B.8: Characterization results of synthesis SS25 and respective AuNPs seeds (SS23): UV-visible spectra and TEM images with 200kX of magnification.

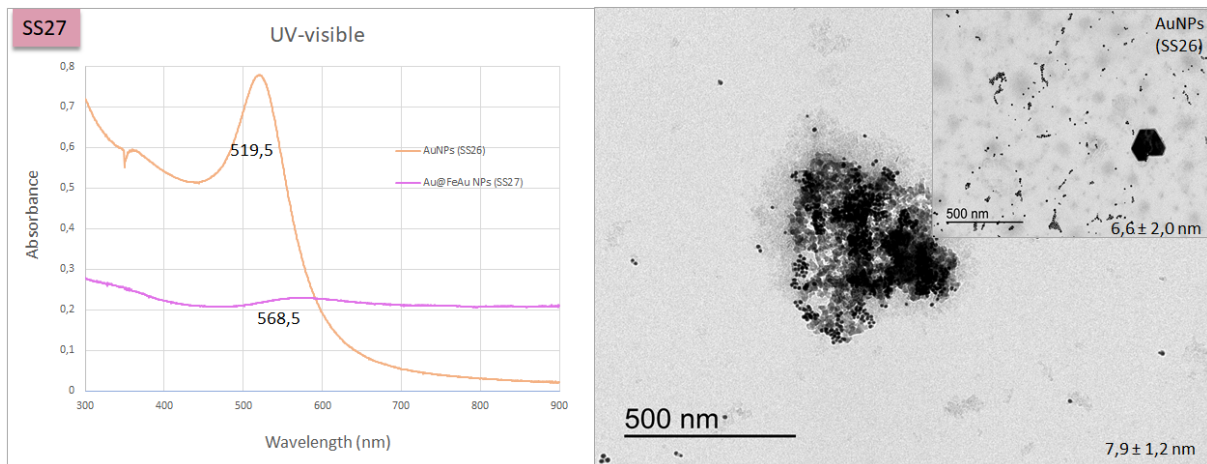


Figure B.9: Characterization results of synthesis SS27 and respective AuNPs seeds (SS26): UV-visible spectra and TEM images with 100kX of magnification.

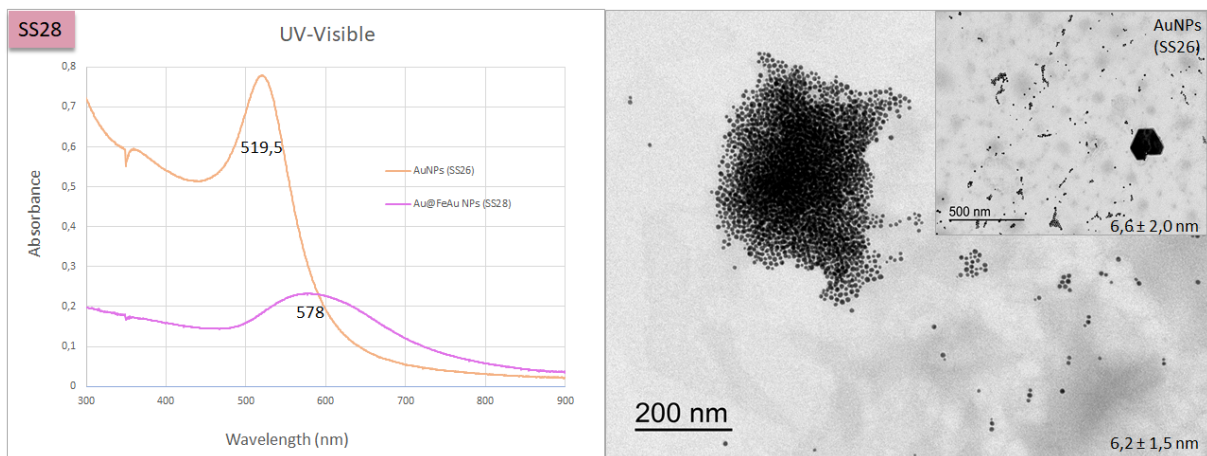


Figure B.10: Characterization results of synthesis SS28 and respective AuNPs seeds (SS26): UV-visible spectra and TEM images with 150kX and 100kX of magnification, respectively.

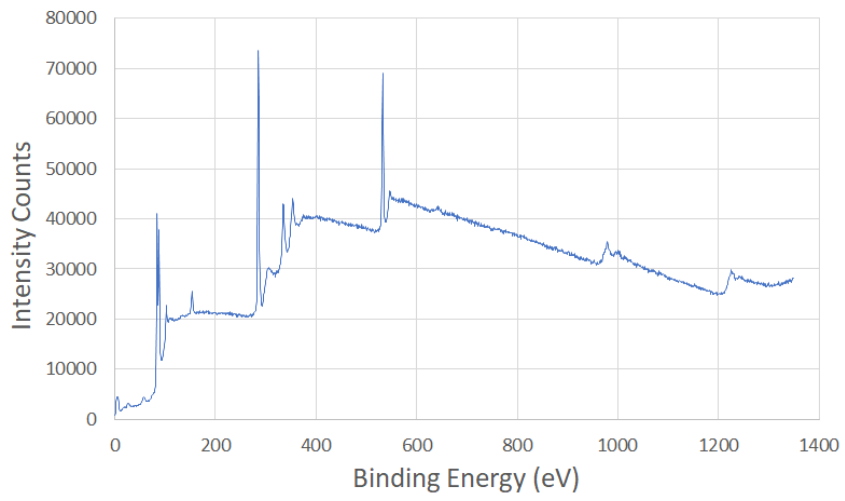


Figure B.11: General XPS spectrum results of sample SS20.

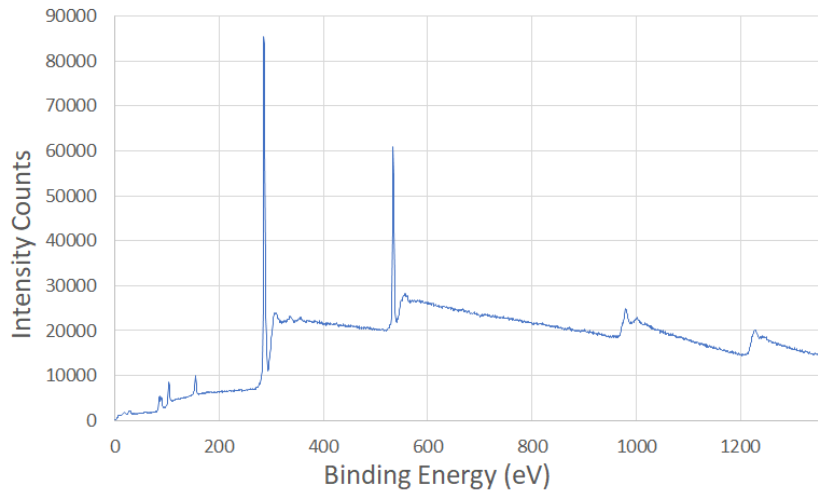


Figure B.12: General XPS spectrum results of sample SS21.

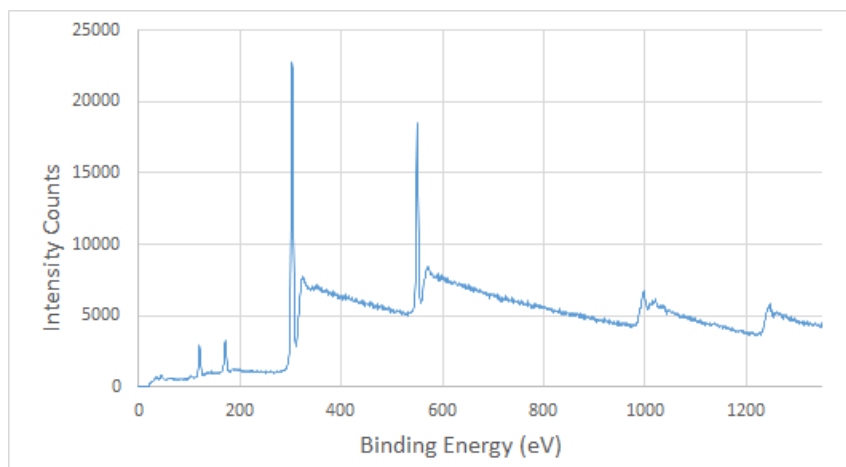


Figure B.13: Repeated measurements of the general XPS spectrum results of sample SS21.

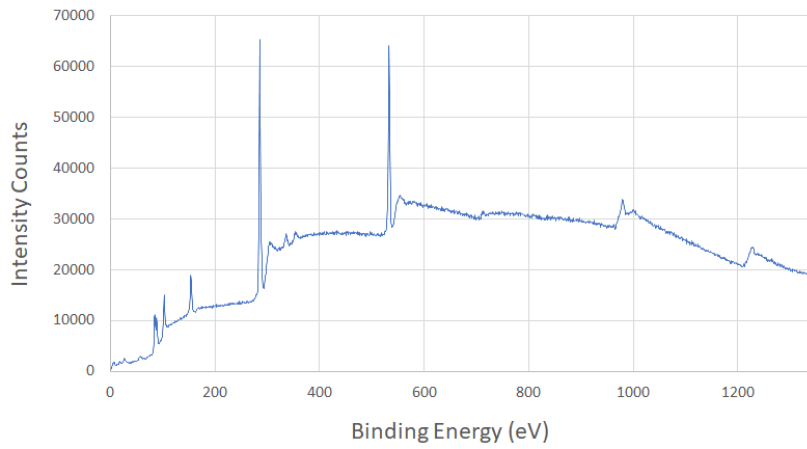


Figure B.14: General XPS spectrum results of sample SS30.

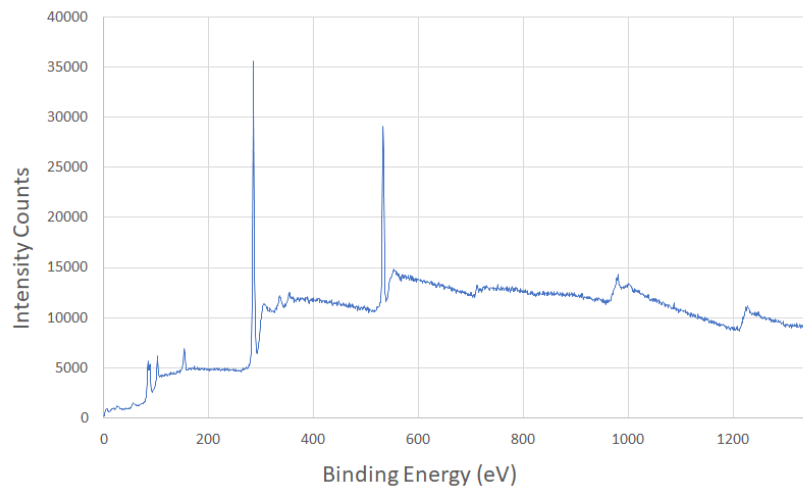


Figure B.15: General XPS spectrum results of sample SS33.

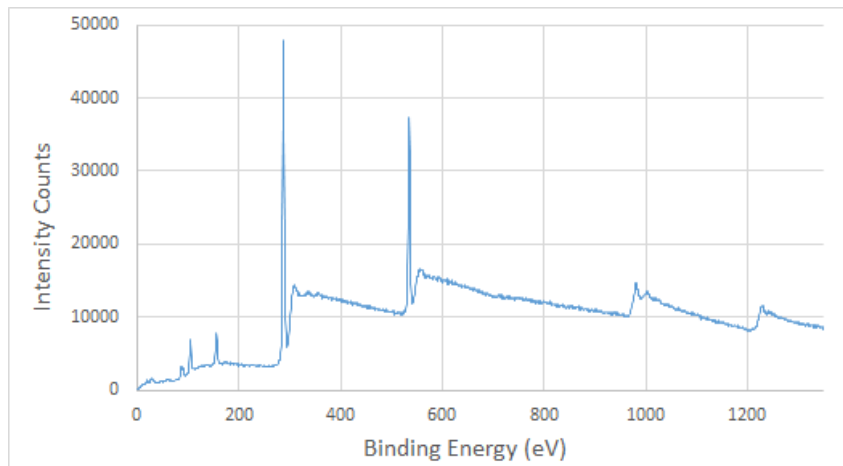


Figure B.16: General XPS spectrum results of the supernatant from sample SS33.

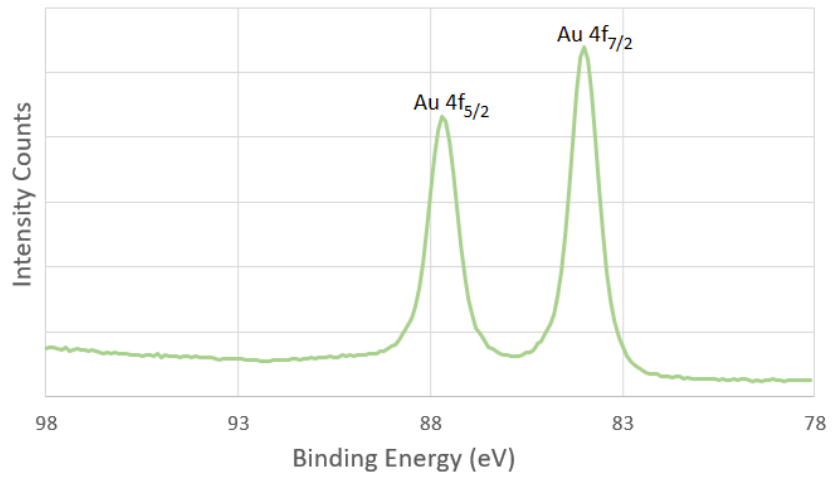


Figure B.17: High resolution XPS results for Au of sample SS20.

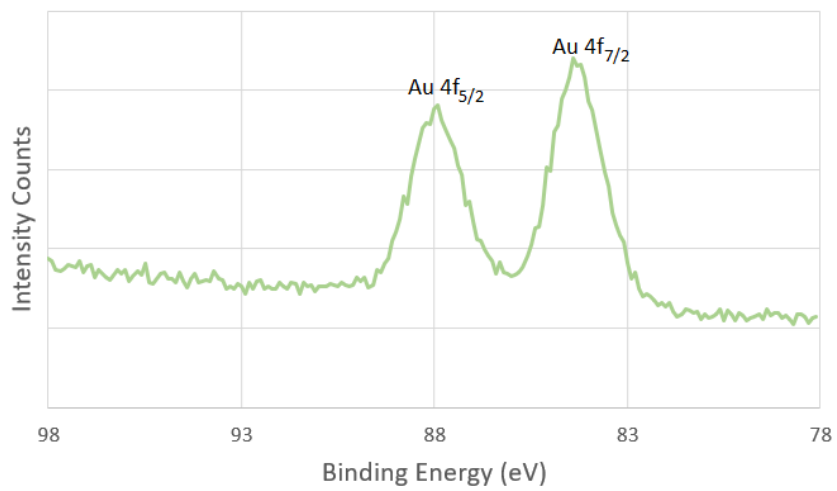


Figure B.18: High resolution XPS results for Au of sample SS21.

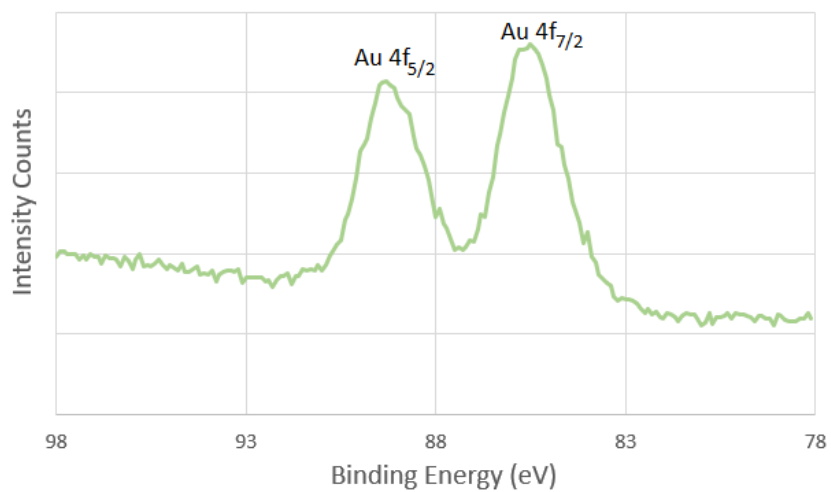


Figure B.19: High resolution XPS results for Au of sample SS30.

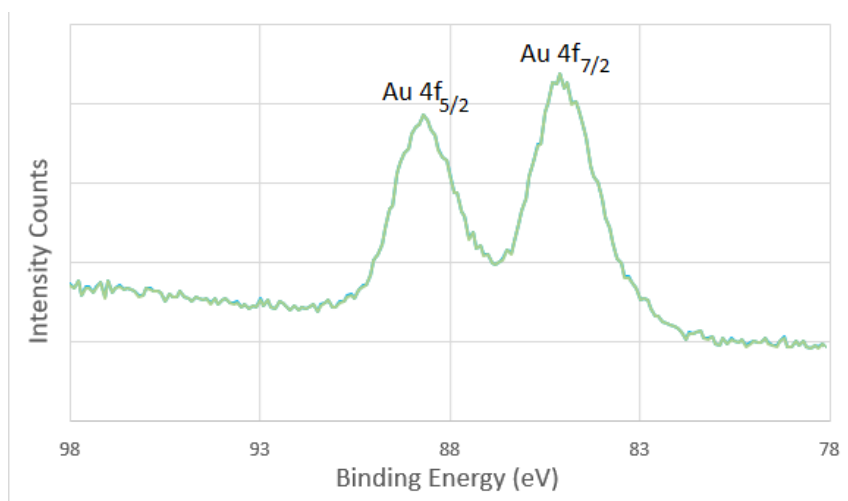


Figure B.20: High resolution XPS results for Au of sample SS33.